

**3D MULTI-FREQUENCY ANTENNA ARRAYS FOR CLINICAL VALIDATION  
OF MICROWAVE BREAST IMAGING**

by  
Suzette Marie Aguilar

A dissertation submitted in partial fulfillment of  
the requirements for the degree of

Doctor of Philosophy  
(Electrical and Computer Engineering)

at the  
UNIVERSITY OF WISCONSIN–MADISON  
2012

Date of final oral examination: 10/15/12

The dissertation is approved by the following members of the Final Oral Committee:

Susan C. Hagness, Professor, Electrical and Computer Engineering  
Nader Behdad, Assistant Professor, Electrical and Computer Engineering  
Barry D. Van Veen, Professor, Electrical and Computer Engineering  
David T. Anderson, Professor, Electrical and Computer Engineering  
Christopher L. Brace, Assistant Professor, Biomedical Engineering

© Copyright by Suzette Marie Aguilar 2012

All Rights Reserved

*To my mother  
for the will to give, to share, and to sacrifice*

“We’ve come a long long way together  
Through the hard times and the good  
I have to celebrate you baby  
I have to praise you like I should”  
—*Norman Cook*

## ACKNOWLEDGMENTS

I am deeply grateful to my advisor, Prof. Susan C. Hagness, for giving me the chance to collaborate in such a meaningful field and for inspiring high standards through her kind and constant mentoring, and to my advisor, Prof. Nader Behdad, for his keen sense of how much is enough and for his contributions to my professional growth. I greatly appreciate their patience and support.

I thank my dissertation committee – Profs. Barry Van Veen, David Anderson, and Christopher Brace – for reading my dissertation and suggesting a few changes.

My thanks to many wonderful colleagues and friends at UW–Madison. Very special thanks to Drs. Earl Zastrow, Mudar Al-Joumayly, Yazid Yusuf, and Jacob Shea for their kindness, wisdom, and strength during the many trying times of this journey, and to Dr. Keely Willis, Dr. Al Mashal, Dr. Steve Kennedy, Matt Burfeindt, TJ Colgan, Fuqiang Gao, and Owen Mays for the countless interactions that reminded me of how fortunate I was to work with such talented individuals.

For the early and continuous enthusiastic encouragement, many thanks to Henry La Rosa, Andrew Quecan, José M. Cerrato, and Mario Castañeda. My gratitude goes to Julia Haviland for her thoughtfulness and for caring so deeply.

I am grateful to my mother, Sonya, for making sure her daughters got the best education possible, for participating in this endeavor through calls and letters, and for leaving a legacy of love, dignity, and respect; to my brilliant and noble sister, Tatiana, who has my unconditional love, for believing in the beauty of truth; and to my father, Pompeyo, for nurturing my natural curiosity and for teaching me, through his example, the importance of a strong work ethic and perseverance.

My deep gratitude goes to my companions in life, in chronological order of appearance, Gail Izaguirre, Alex Fraño, and Bojana Zivanovic, for putting up with my unbalanced perfectionism, for standing by me throughout the years and while I completed this project, and for working together to make the world a better place to be. Finally, thanks to my furry bundle of joy, Toto, whose sensitive and loving soul brightened all of the days of this undertaking.

“Are you such a dreamer?  
To put the world to rights?  
I’ll stay home forever  
Where two and two always  
makes up five”

*-Radiohead*

## ABSTRACT

Microwave breast imaging has been identified as a promising low-cost, non-ionizing, and quantitative 3D imaging modality for improving breast cancer screening and diagnosis. An array of antennas transmits low-power microwave signals into the breast. The measured scattered signals are used to reconstruct the spatial distribution of the dielectric properties throughout the breast volume via a solution of the inverse scattering problem. Interpreting results from initial clinical studies of microwave tomographic imaging has been hindered by the lack of precise co-registration between microwave and benchmark images. At this stage, rigorous validation of microwave breast imaging against a 3D clinical benchmark such as magnetic resonance imaging (MRI) is needed and requires image co-registration, which is most reliably achieved with the breast in the same position during both the MRI and microwave scans.

We address two key factors that would enable straightforward co-registration and an objective and unambiguous comparison with MRI. First, we investigate the use of a polycaprolactone (PCL)-based thermoplastic mesh to serve as a tissue immobilization interface in a microwave imaging system designed for MRI-based validation. We characterize the wide-band dielectric properties of thermoplastic meshes in the frequency range of 0.5-3.5 GHz. We also characterize the dielectric properties of a vegetable oil – a candidate biocompatible immersion medium for the microwave imaging system. We show that the PCL-based thermoplastic material and the vegetable oil are well matched, essentially rendering the mesh invisible during the microwave scan.

Second, we investigate the performance characteristics of a class of slot-loaded patch antennas that compose a 3D microwave breast imaging array configured to occupy the space

vacated by removable breast coils in the patient support platform of a breast MRI system. This configuration imposes a constraint on the overall size and layout of the antenna array system and necessitates the use of miniaturized antennas. Additionally, the antennas are designed to operate in the biocompatible immersion medium at multiple frequencies within the frequency range of 0.5-3.5 GHz. Investigations on the radiation characteristics of the slot-loaded patch antenna elements and the multi-static channel characteristics of the antenna array indicate that these sensors are suitable candidates for microwave breast imaging.

**DISCARD THIS PAGE**



# TABLE OF CONTENTS

	Page
<b>ABSTRACT</b> . . . . .	iv
<b>LIST OF FIGURES</b> . . . . .	viii
<b>LIST OF TABLES</b> . . . . .	xvi
<b>1 Introduction</b> . . . . .	1
<b>2 Background</b> . . . . .	5
2.1 Review of microwave breast imaging research . . . . .	5
2.2 Strategy for precise co-registration of microwave and MR breast images . . . . .	7
2.3 Thermoplastic materials for immobilizing breast tissue . . . . .	8
2.4 Antenna array elements for microwave breast imaging . . . . .	9
2.4.1 Desired features of a 3D microwave sensor array . . . . .	9
2.4.2 Prior antenna array element designs for microwave breast imaging systems . . . . .	9
2.4.3 Multi-band miniaturized patch antennas for microwave breast imaging . . . . .	10
2.4.4 Mutual coupling . . . . .	12
<b>3 Dielectric characterization of a tissue-stabilizing thermoplastic material and biocompatible immersion medium for microwave breast imaging</b> . . . . .	13
3.1 Dielectric properties of PCL-based thermoplastic materials . . . . .	14
3.1.1 Method of dielectric characterization . . . . .	15
3.1.2 Validation and results . . . . .	19
3.1.3 Summary . . . . .	20
3.2 Dielectric properties of a biocompatible immersion medium . . . . .	20
3.2.1 Method of dielectric characterization . . . . .	22
3.2.2 Measurement results and data fitting . . . . .	22
3.2.3 Impedance match between PCL-based thermoplastic material and immersion medium . . . . .	24
3.2.4 Impact of the thermoplastic mesh on microwave breast imaging . . . . .	31

	Page
3.2.5 Summary . . . . .	32
<b>4 Multi-band miniaturized patch antennas for microwave breast imaging</b>	<b>34</b>
4.1 Introduction . . . . .	34
4.2 Measurement and experimental verification of a dual-band miniaturized patch antenna . . . . .	36
4.3 Multi-band miniaturized patch antennas . . . . .	41
4.3.1 Antenna design . . . . .	41
4.3.2 Results . . . . .	46
4.4 Effect of antenna pair separation distance on calculated gain . . . . .	58
4.5 Summary . . . . .	60
<b>5 Microwave breast imaging arrays comprised of multi-band miniaturized patch antennas</b>	<b>62</b>
5.1 Introduction . . . . .	62
5.2 Array design . . . . .	63
5.3 Reduction of mutual coupling . . . . .	64
5.4 Results . . . . .	76
5.4.1 Antenna element in array panel . . . . .	76
5.4.2 Antenna elements in 3D sensor array . . . . .	79
5.5 Summary . . . . .	85
<b>APPENDIX Bandwidth-enhanced miniaturized patch antenna</b>	<b>88</b>
A.0.1 Measurement and experimental verification results . . . . .	88
<b>LIST OF REFERENCES</b>	<b>92</b>

**DISCARD THIS PAGE**

## LIST OF FIGURES

Figure	Page	
2.1	Photograph of the patient support platform of a commercial breast MRI system. . . . .	8
2.2	Radiating elements most widely used in microwave breast imaging systems. (a) 32 monopole antenna array [1]. (b) Simple monopole antenna consisting of a coaxial cable from which the outer conductor has been stripped [2]. (c) Dipole antenna with a balun to reduce the radiation from the outer conductor of the semirigid coaxial cable [3]. . . . .	10
3.1	Photographs of PCL-based thermoplastic meshes characterized in this study. (a) A U-Plast <sup>TM</sup> 8338BL.SO2+/R thermoplastic mesh molded to a physical breast phantom. (b) An Efficast <sup>®</sup> 8333Y.3/R 2.0-mm-thick mesh with 2.8-mm-diameter holes created on a hexagonal lattice with $a = 5.8$ mm. (c) A U-Plast <sup>TM</sup> 8338BL.SO2+/R 2.4-mm-thick mesh with 1.4-mm-diameter holes created on a rectangular lattice with $w_1 = 5.6$ mm and $w_2 = 2.8$ mm. . . . .	15
3.2	Equivalent circuit model of the transmission line configuration. The parasitic elements associated with the coaxial-to-microstrip transition are contained inside the dash-dot-dash boxes ( $L = 0.28$ nH, $R = 0.05$ $\Omega$ , $C = 0.07$ pF). . . . .	16
3.3	Measured $S_{21}$ for a microstrip transmission line (width of 10 mm, length of 265 mm) fabricated on a substrate comprised of a perforated PCL-based thermoplastic (Efficast <sup>®</sup> 8333Y.3/R), compared with the ADS-computed $S_{21}$ for a model of the microstrip with optimized substrate dielectric properties. . . . .	20
3.4	Dielectric properties of two PCL-based thermoplastic materials, as a function of frequency, obtained from microstrip transmission-line measurements. The properties correspond to those of the bulk thermoplastic, after accounting for the air holes (i.e., perforations) in the commercial samples of (a) Efficast <sup>®</sup> 8333Y.3/R and (b) U-Plast <sup>TM</sup> 8338BL.SO2+/R. . . . .	21

Figure	Page
3.5 Comparison of the dielectric properties of safflower oil with varying time exposure to air. (a) Relative permittivity and (b) effective conductivity of safflower oil as a function of frequency. Each curve represents the average properties of three different measurements of the same sample. . . . .	25
3.6 Comparison of first order Debye model fit with measured dielectric properties of safflower oil samples. The Debye model was fit to measured oil dielectric properties in the frequency range of 5-10 GHz. (a) Relative permittivity and (b) effective conductivity as a function of frequency. Dash-dot line represents the average properties of three different measurements of the same sample. . . . .	26
3.7 Comparison of first order Debye model fit with measured dielectric properties of safflower oil samples. The Debye model was fit to measured oil dielectric properties in the frequency range of 0.5-5 GHz. (a) Relative permittivity and (b) effective conductivity as a function of frequency. Dash-dot line represents the average properties of three different measurements of the same sample. . . . .	27
3.8 Comparison of second order general dispersion model fit with measured dielectric properties of safflower oil samples. The second order model was fit to measured oil dielectric properties in the frequency range of 0.5-5 GHz. (a) Relative permittivity and (b) effective conductivity as a function of frequency. Dash-dot line represents the average properties of three different measurements of the same sample. . . . .	28
3.9 Measured transmission coefficients of a two-antenna system demonstrating the invisibility of the thermoplastic mesh in oil. The two dual-band miniaturized patch antennas are immersed in safflower oil and separated by 10 cm. . . . .	29
3.10 Difference between the measured transmission coefficients $S_{21}$ of a two-antenna system with and without a thermoplastic mesh in oil. The two dual-band miniaturized patch antennas are immersed in safflower oil and separated by 8 cm. Difference of the $S_{21}$ for (a) an Efficast® 8333Y.3/R mesh in oil and for an (b) U-Plast™ 8338BL.SO2+/R mesh in oil. The dash-dot line corresponds to the case when no thermoplastic sheet is present. . . . .	30
3.11 Coronal cross-sections of reconstructed three-dimensional dielectric profiles of a Class 2 (scattered fibroglandular) breast phantom. (a)-(b) Images of the phantom with no thermoplastic sheet. (c)-(d) Images of the phantom with the thermoplastic sheet at the skin surface. Dielectric constant, left, and effective conductivity (S/m), right, at 2.0 GHz. . . . .	33

Figure	Page
4.1 Photograph of the fabricated dual-band miniaturized patch antenna. . . . .	36
4.2 Simulated and measured reflection coefficients of the miniaturized patch antenna of Figure 4.1 immersed in safflower oil. . . . .	37
4.3 Simulated and measured transmission coefficients of a two-antenna system composed of the dual-band miniaturized patch antenna of Figure 4.1 immersed in safflower oil and separated by 10 cm. . . . .	38
4.4 Measured and simulated radiation patterns of the dual-band miniaturized patch antenna in oil. The patterns are obtained at a distance of 15 cm from the patch. (a) E-plane at 1.34 and (b) 2.87 GHz. (c) H-plane at 1.34 and (d) 2.87 GHz. Red: simulated data. Blue: measured data. Circle: co-pol. x: cross-pol. . . . .	39
4.5 Photograph of the fabricated small dipole antenna. . . . .	39
4.6 Measured reflection coefficients of the dual-band miniaturized patch antenna of Figure 4.1 and a small dipole of Figure 4.5 immersed in safflower oil. . . . .	40
4.7 Measured transmission coefficients of a two-antenna system composed either of dual-band miniaturized patch antennas or small dipoles. The two antennas are immersed in safflower oil and separated by 10 cm. . . . .	40
4.8 Top view of (a) standard patch, (b) slot-loaded patch, (c) slot-loaded patch with center slot, and (d) dual-band miniaturized patch antenna. (e) Schematic of current distributions for the first three longitudinal modes showing where the current is affected by the various slots in (b)-(d). . . . .	42
4.9 Top view of the (a) tri-band, and (b) quad-band miniaturized patch antennas. . . . .	44
4.10 Simulated and measured reflection coefficients of the dual-band miniaturized patch antenna of Figure 4.9(a) immersed in safflower oil. . . . .	45
4.11 Simulated and measured reflection coefficients of the tri-band miniaturized patch antenna of Figure 4.9(b) immersed in safflower oil. . . . .	45
4.12 Simulated and measured reflection coefficients of the quad-band miniaturized patch antenna of Figure 4.9(b) immersed in safflower oil. . . . .	46
4.13 Calculated gain versus frequency for different dielectric constants ( $\epsilon_r$ ) and thickness $h$ of the substrate. (a) $\epsilon_r = 3.55$ , (b) $\epsilon_r = 6.15$ , (c) $\epsilon_r = 10.2$ . . . . .	50

Figure	Page
4.14 Simulated and measured transmission coefficients of a two-antenna system composed of the tri-band miniaturized patch antenna of Figure 4.9(b) immersed in safflower oil and separated by 10 cm. . . . .	52
4.15 Simulated and measured radiation patterns of the tri-band miniaturized patch antenna in oil. The patterns are obtained at a distance of 15 cm from the patch. (a) E-plane at 1.36 GHz (b) 1.74 GHz and (c) 3.02 GHz. (d) H-plane at 1.36 GHz (e) 1.74 GHz and (f) 3.02 GHz. Solid red: simulated data. Dotted blue: measured data. Circle: co-pol. x: cross-pol. . . . .	54
4.16 Simulated and measured radiation patterns of the quad-band miniaturized patch antenna in oil. The patterns are obtained at a distance of 15 cm from the patch. (a) E-plane at 1.36 GHz (b) 1.74 GHz (c) 2.38 GHz, and (d)3.02 GHz. (e) H-plane at 1.36 GHz (f) 1.74 GHz (g) 2.38 GHz, and (h) 3.02 GHz. Solid red: simulated data. Dotted blue: measured data. Circle: co-pol. x: cross-pol. . . .	56
4.17 Comparison of imaging a Class II (scattered fibroglandular) breast phantom using two types of antenna arrays. Coronal (top row) and sagittal (bottom row) cross-sections of relative permittivity at 2.0 GHz. (a)-(b) True profile. (c)-(d) Images reconstructed using a multi-band miniaturized patch antenna array. (e)-(f) Images reconstructed using a dipole array. . . . .	57
4.18 Calculated antenna gain versus the separation distance (as a function of $\lambda$ ) between a pair of half-wavelength linear dipoles. Antenna gain obtained at the resonant frequency of the dipoles. . . . .	59
4.19 Calculated antenna gain versus the separation distance (as a function of $\lambda$ ) between a pair of slot-loaded, multi-band miniaturized patch antenna types immersed in safflower oil. Antenna gain obtained at $f_{100}$ and $f_{300}$ for (a) basic patch (b) CS patch (c) RS patch (d) RS+CS patch (e) NRS patch (f) CS+NRS patch (g) RS+NRS patch (h) RS+CS+NRS patch. For all figures the separation distance at which the strictest criterion (s.c.) is satisfied occurs at $3\lambda$ , except for (a) and (b), where the s.c. is noted. Solid circle and solid triangle: gain obtained using an antenna pair separated by 15 cm for $f_{100}$ and $f_{300}$ , respectively. . . . .	61

Figure	Page	
5.1	Microwave sensor array geometry. (a) Frontal view of one panel of the proposed array showing eight slot-loaded, miniaturized patch antennas. (b) Cross-sectional view of one slot-loaded, miniaturized patch antenna. (c) 3D view of the proposed sensor array, with side walls populated with patch antennas and top and bottom panels that contain metal planes. The top metal plane includes an opening that allows the breast to be suspended in the imaging volume. . . . .	64
5.2	Simulated responses of RS patch antennas patterned on Rogers RO4003 substrate panels ( $\epsilon_r = 3.55$ ) of different thicknesses. (a) reflection coefficients ( $S_{11}$ ) (b)-(d) mutual coupling ( $S_{21}$ ) between pairs of (b) horizontally adjacent, (c) diagonally adjacent, and (d) vertically adjacent (boxed dashed lines). The left and right sub-plots show the 1st and 2nd frequency bands, respectively. . . . .	66
5.3	Simulated responses of RS patch antennas patterned on Rogers RO4360 substrate panels ( $\epsilon_r = 6.15$ ) of different thicknesses. (a) reflection coefficients ( $S_{11}$ ) (b)-(d) mutual coupling ( $S_{21}$ ) between pairs of (b) horizontally adjacent, (c) diagonally adjacent, and (d) vertically adjacent (boxed dashed lines). The left and right sub-plots show the 1st and 2nd frequency bands, respectively. . . . .	67
5.4	Simulated responses of RS patch antennas patterned on Rogers RO3010 substrate panels ( $\epsilon_r = 10.2$ ) of different thicknesses. (a) reflection coefficients ( $S_{11}$ ) (b)-(d) mutual coupling ( $S_{21}$ ) between pairs of (b) horizontally adjacent, (c) diagonally adjacent, and (d) vertically adjacent (boxed dashed lines). The left and right sub-plots show the 1st and 2nd frequency bands, respectively. . . . .	68
5.5	Simulated responses of RS patch antennas for different element arrangements in an array panel: 3 by 3 (arrangement 1), staggered-frequency (arrangement 2), and staggered-element (arrangement 3). (a) reflection coefficients ( $S_{11}$ ) of a central element (b)-(d) mutual coupling ( $S_{21}$ ) between pairs of (b) horizontally adjacent, (c) diagonally bottom adjacent, and (d) vertically bottom adjacent (boxed dashed lines). The left and right sub-plots show the 1st and 2nd frequency bands, respectively. . . . .	70
5.6	Change in mutual coupling for pairs of adjacent antennas in the staggered-frequency (arrangement 2) and the staggered-element (arrangement 3) element arrangement relative to a 3 by 3 (arrangement 1) (shown in Figure 5.5). Change in mutual coupling ( $S_{21}$ ) between pairs of antennas adjacent to the center element of the panel are shown. The results are shown for the resonant frequency of (a) $TM_{100}$ and (b) $TM_{300}$ of the RS patch antenna. . . . .	71



Figure	Page
5.7 Simulated responses of RS patch antennas on different geometrical variations of the array panel substrate: basic substrate panel (case A), metal walls (case B), trenches on substrate (case C), and soft-surface substrate (case D). (a) reflection coefficients ( $S_{11}$ ) (b)-(d) mutual coupling ( $S_{21}$ ) between pairs of (b) horizontally adjacent, (c) diagonally adjacent (d) vertically adjacent. The left and right sub-plots show the 1st and 2nd frequency bands, respectively. . . . .	72
5.8 Change in mutual coupling for pairs of adjacent antennas in the metal walls (case B), trenches on substrate (case C), and soft-surface substrate (case D) geometrical variations on the panel substrate relative the basic substrate panel (case A) (shown in Figure 5.7). Change in mutual coupling ( $S_{21}$ ) between pairs of antennas adjacent to the center element of the panel are shown. The results are shown for the resonant frequency of (a) $TM_{100}$ and (b) $TM_{300}$ of the RS patch antenna. . . . .	73
5.9 Simulated responses of RS patch antennas on different array panel arrangements, 3 by 3 on a basic substrate panel (arrangement 1), staggered-element on a basic panel substrate (arrangement 2), 3 by 3 on a soft-surface structure substrate (arrangement 3), and staggered-element on a soft-surface structure substrate (arrangement 3 + case D). (a) reflection coefficients ( $S_{11}$ ) (b)-(d) mutual coupling ( $S_{21}$ ) between pairs of (b) horizontally adjacent, (c) diagonally adjacent, and (d) vertically adjacent (boxed dashed lines). The left and right sub-plots show the 1st and 2nd frequency bands, respectively. . . . .	75
5.10 Comparison of the simulated mutual coupling $S_{21}$ between a pair of dual-band miniaturized antennas that are vertically adjacent (3 by 3, top left) and diagonally adjacent (staggered-element, top right) (boxed dashed lines). The antennas are patterned on a 32-mil-thick Rogers RO4003 substrate panel ( $\epsilon_r = 3.55$ ). . .	76
5.11 Photograph of the fabricated dual-band miniaturized patch antenna in an array.	78
5.12 Simulated and measured reflection coefficients of an isolated dual-band miniaturized patch antenna immersed in safflower oil. Measured data for an antenna in an array is also shown. . . . .	78
5.13 Simulated and measured transmission coefficients of an antenna system composed of two dual-band miniaturized antennas. The two patch antennas are immersed in safflower oil and separated by 10 cm. Measured data for antenna array elements is also shown. . . . .	79

Figure	Page
5.14 Photograph of a prototype of one 13 cm × 13 cm panel of the proposed array showing eight dual-band miniaturized (28 mm × 29 mm) antennas. . . . .	80
5.15 Illustration of the 3D sensor array comprised of dual-band miniaturized antennas with (a) no phantom present, (b) simple fatty phantom, (c) simple glandular tissue phantom, and (d) simple fatty and glandular inclusion phantom present. . . . .	82
5.16 Simulated reflection coefficients ( $S_{ii}$ ) for dual-band miniaturized patch antennas in an oil-filled 3D sensor array. The left and right sub-plots show the 1st and 2nd frequency bands, respectively. [(a)-(b)] $S_{ii}$ of antennas in sensor array with no phantom present and [(c)-(d)] $S_{ii}$ of antennas in sensor array with the simple fatty phantom of Figure 5.15(b) present. The bold black line corresponds to a single isolated antenna $S_{ii}$ . . . . .	83
5.17 Simulated reflection coefficients ( $S_{ii}$ ) for dual-band miniaturized patch antennas in an oil-filled 3D sensor array with and without the phantoms of Figures 5.15 (b)-(c) present. The left and right sub-plots show the 1st and 2nd frequency bands, respectively. The bold black line corresponds to a single isolated antenna $S_{ii}$ with no phantom present. . . . .	84
5.18 Illustration of the 3D sensor array comprised of RS patch antennas on substrates using soft-surface structures. (a) single array panel and (b) 3D sensor array with simple phantom present. . . . .	85
5.19 Comparison of the responses of antenna elements in an individual array panel and a 3D sensor array with and without the simple phantom of Figure 5.18 (b), immersed in oil. (a) reflection coefficients ( $S_{11}$ ) of a central antenna element. (b)-(c) Mutual coupling ( $S_{21}$ ) between (b) diagonally and (c) horizontally adjacent antennas. The left and right sub-plots show the 1st and 2nd frequency bands, respectively. . . . .	86
5.20 Comparison of the transmission coefficients between two central antennas directly facing each other on opposite panels within an oil-filled 3D sensor array with and without the simple phantom of Figure 5.18(b) present. The left and right sub-plots show the 1st and 2nd frequency bands, respectively. . . . .	87
A.1 Top view of proposed bandwidth-enhanced patch antenna. . . . .	88
A.2 Simulated and measured reflection coefficients of the bandwidth-enhanced patch antenna of Figure A.1 immersed in safflower oil. . . . .	90

Figure	Page
A.3 Measured and simulated radiation patterns of the bandwidth-enhanced patch antenna in oil. The patterns are obtained at a distance of 15 cm from the patch. (a) E-plane at 1.73 GHz (b) 1.76 GHz and (c) 1.80 GHz. (d) H-plane at 1.73 GHz (e) 1.76 GHz and (f) 1.80 GHz. Red: simulated data. Blue: measured data. Circle: co-pol. x: cross-pol. . . . .	91

**DISCARD THIS PAGE**

## LIST OF TABLES

Table	Page
2.1 Review of antenna elements designed for experimental tomographic microwave breast imaging systems. . . . .	11
4.1 Calculated frequencies of operation and gain of several slot-loaded patch antenna types. White: $TM_{100}$ . Green: $TM_{300}$ . Blue: $TM_{500}$ . Red: $TM_{010}$ . . . . .	47
4.2 Calculated and measured values of multi-band miniaturized patch antennas discussed in Section 4.3.2.1. White: $TM_{100}$ . Green: $TM_{300}$ . Blue: $TM_{500}$ . Red: $TM_{010}$ . . . . .	53

# Chapter 1

## Introduction

According to the American Cancer Society, in 2009 an estimated 192,000 new cases of invasive breast cancer were diagnosed among women and approximately more than 40,000 women were expected to die from the disease [4]. Only lung cancer accounts for more cancer deaths in women. High breast tissue density (amount of glandular tissue relative to fatty tissue in the breast) has been shown to be a strong independent risk factor for the development of breast cancer. Women with the highest levels of breast density were found to have a four- to six-fold increased risk of breast cancer compared with women with the least dense breasts [5–7]. Recent research indicates that increasing breast density over time may be a strong predictor of breast cancer [8].

Five-year relative survival is lower among women with a more advanced stage at diagnosis. Larger tumor size at diagnosis is also associated with decreased survival [4]. Thus, it is crucial for clinicians to have access to medical imaging tools that will aid them in early-stage breast cancer diagnosis when the tumor may be small and more easily treated.

The most widespread method of breast cancer detection is X-ray mammography, but it presents some limitations [9]. The potential for false positive and false negative results remains high. Mammography on average will detect about 80%-90% of the breast cancers in women without symptoms. Studies suggest that mammography screenings may miss as many as one in six tumors. The risk of false positive results is about one in ten and about 75% of suspicious biopsies due to a mammogram are benign [10]. High breast density decreases the

sensitivity of mammography compared to women with less dense breasts [11]. Additionally, mammography requires breast compression and exposure to ionizing radiation.

An alternative imaging technique, magnetic resonance imaging (MRI) produces very detailed, cross-sectional images of the body. For women at high risk for breast cancer and with dense breasts, a screening MRI may be recommended. However, MRI is problematic for claustrophobic and obese patients, expensive, and not widely available, especially in underdeveloped parts of the world. There are persisting concerns about its low specificity compared to mammography [12]. Ultrasound is another alternate imaging technique that may help distinguish between benign and malignant masses. However, it lacks sensitivity and may result in higher false positive rates than mammography [13]. Due to their limitations, neither MRI or ultrasound is recommended as a general screening technique.

Effective imaging modalities for the early detection and diagnosis of breast cancer would improve the care of women who are at high risk by reducing the number of false alarms and the number of cases that go undetected [10]. The Institute of Medicine and National Research Council identified three potential ways to improve detection of breast cancer: more widespread use of mammography, better quality mammography, and development of new technologies [10]. Recent investigations strongly suggest that low-cost non-ionizing microwave tomography (see, for example, [1–3, 14–18]) is well-suited for screening women at higher risk for breast cancer as well as monitoring changes in breast tissue in response to prevention and treatment protocols. This type of imaging application will also provide a 3D, affordable, non-ionizing, tomographic, and quantitative breast imaging solution for breast density evaluation in the general population.

In active microwave breast imaging, low-power microwave signals are transmitted into the breast using an array of antennas. The measured scattered signals are used to reconstruct the spatial distribution of the dielectric properties, or some related characteristic such as scattering strength, throughout the breast volume. A biocompatible immersion medium is used to fill the void between the array of antennas and the breast.

Microwave breast tomography has been the subject of extensive numerical and laboratory investigations (e.g., [17, 19–23]). Preliminary clinical studies have also been reported [1, 24, 25]. At this stage, this technology has not been rigorously validated. Unambiguous comparison with a 3D clinical benchmark is needed to demonstrate the feasibility of using microwave imaging as an alternate breast imaging tool. Rigorous validation of microwave imaging using a clinical benchmark such as magnetic resonance imaging (MRI) technology requires precise co-registration. This dissertation addresses two key factors that would enable straightforward co-registration and an objective and unambiguous comparison:

1. A patient interface that immobilizes the breast so that the same position is maintained during both the MRI and microwave scans.
2. A microwave antenna array that fits within the interstitial space of an MRI patient support platform.

Thermoplastic meshes are commonly used as immobilization devices in radiation oncology, as well as in interventional breast MRI applications such as MR-guided preoperative localization or MR-guided needle biopsy [26, 27]. Such meshes are promising candidates for the patient interface in a microwave imaging design for MRI-based validation. This dissertation has addressed the need to characterize the wideband dielectric properties of tissue-stabilizing thermoplastic meshes. This data is important because it enables an investigation of the potential impact of the immobilization mesh on microwave imaging performance as well as a determination of system features, such as the immersion medium, that minimize that impact.

The microwave sensor array that is used in a 3D microwave tomography system has a direct impact on the accuracy of microwave breast imaging. The degree of ill-posedness of the inverse problem varies with the number and location of observations, the number of frequencies used, and the spatial resolution provided by the illuminating wavelengths [28]. The 3D antenna array that surrounds the breast of a prone patient is ideally composed of a large number of miniaturized elements, antennas that operate efficiently at multiple frequencies within the frequency range of 0.5-3.5 GHz, and antennas that are not so complex as to



render them impractical to model in the reconstruction algorithm. The work performed for this dissertation has also focused on the investigation of multi-frequency miniaturized patch antennas for a 3D microwave sensor array. An investigation of the radiation characteristics of the patch antenna elements that compose the array as well as the multi-static channel characteristics of the microwave sensor array indicates that these radiators are suitable candidates for microwave breast imaging. The microwave sensor system developed will be used in future research to demonstrate the feasibility of using microwave breast imaging in studies of breast density estimation and lesion detection and localization. The outcome of this investigation also contributes to the general knowledge base in the field of compact patch antennas and array design.

Chapter 2 gives an overview of microwave breast imaging research, thermoplastic materials, and previous work done on antenna array element designs for microwave breast imaging systems. The dielectric characterization of a tissue-stabilizing thermoplastic mesh and a biocompatible oil immersion medium is described in Chapter 3. In Chapter 4, several multi-band miniaturized patch antennas designed for use in a 3D sensor array for microwave breast imaging are presented and characterized. The multi-static characteristics of the multi-frequency 3D sensor array in the vicinity of a simple breast phantom immersed in the biocompatible medium are described in Chapter 5.

## Chapter 2

### Background

Microwave breast imaging using inverse scattering methods has been identified as a potential breast imaging tool for early detection of breast cancer, for monitoring changes in breast tissue in response to prevention and treatment protocols, and for evaluating breast density for individualized risk assessment. In microwave tomography, low-power microwave signals are transmitted into the breast tissue by an array of antennas, the scattered signals are measured, and the spatial distribution of the dielectric properties throughout the breast volume are estimated by solving an electromagnetic nonlinear inverse scattering problem. In this chapter, a brief overview of microwave breast imaging research is given, previously proposed antenna array elements for microwave breast imaging are described, and several topics related to the design of slot-loaded, miniaturized patch antennas elements for a microwave breast imaging array are briefly presented.

#### 2.1 Review of microwave breast imaging research

There is a growing interest in the development of microwave diagnostic techniques in medicine. Microwave breast imaging, an exploratory technique for improving breast cancer screening and diagnosis [10], has been the subject of numerous recent research studies (see, for example, [1, 2, 16–18, 29, 30]). Active methods of microwave imaging of the breast include microwave-induced thermoacoustic (MI-TA) tomography, ultrawideband radar-based methods, and microwave tomography. In MI-TA the absorbed electromagnetic energy induces acoustic waves by means of thermoelastic expansion, which can then be detected

by ultrasound transducers and processed for image reconstruction [31–34]. In radar-based methods [19, 30, 35], the scattered signals are processed to locate strongly scattering tissue formations. Radar-based methods were extensively investigated under an earlier assumption that the contrast between malignant and normal breast tissues was high (2:1 or higher).

A large-scale spectroscopy study showed that the contrast between malignant and normal fibroglandular tissues in the breast is  $\sim 10\%$  [36]. This dielectric constant ratio can be dramatically enhanced by exogenous tumor-targeting molecules [34]. The study also found that normal fibroglandular tissue exhibits more than a 5:1 dielectric contrast with adipose tissue [36], which points to the utility of microwave imaging techniques for breast density evaluation.

In microwave tomography, the measured scattered signals are used to estimate the spatial distribution of the dielectric properties throughout the breast volume by solving an electromagnetic nonlinear inverse scattering problem. Extensive inverse scattering contributions for breast imaging have recently been made [1–3, 14, 17, 28, 37, 38]. Differential images obtained using a numerical test bed demonstrate a successful approach where contrast agents are used in conjunction to microwave imaging to detect and localize tumors [18]. Additionally, results of a recent theoretical study support the utility of 3D microwave tomography for imaging the distribution of dense fibroglandular tissue [29].

Numerical and laboratory investigations of microwave breast tomography have been reported. In a numerical test bed, high-fidelity breast phantoms offer a well-controlled idealized test environment [17, 19–22]. The properties of these numerical phantoms are known exactly, e.g. MRI-derived models, and thus, they serve as rigorous benchmarks for imaging results. However, numerical test beds lack the realism in data acquisition artifacts that inevitably arise in experiments. Laboratory test beds use experimental phantoms constructed from synthetic materials that accurately mimic tissue properties [23] and have known structures. The phantoms have simple heterogeneities and offer the flexibility to study contrast-enhanced microwave imaging performance. However, highly complex structural distributions of the breast are difficult to mimic using experimental phantoms.

Some initial clinical studies of microwave breast imaging have been reported [1, 24, 25]. In [1, 24], 2D coronal-plane microwave images of the uncompressed breast were compared with 2D mammographic (craniocaudal) projection images of the breast under compression. Interpretation of microwave results is hindered by the limitations of 2D imaging and by the lack of precise co-registration between microwave and benchmark images. At this stage, a precise clinical validation of this technology is needed to demonstrate the feasibility of using microwave breast imaging in breast density estimation and lesion detection and localization.

## 2.2 Strategy for precise co-registration of microwave and MR breast images

Validation of 3D microwave imaging requires unambiguous co-registration with an existing 3D clinical benchmark, such as MRI. In this type of study, the true breast structure is known due to the registered benchmark attained.

Figure 2.1 shows a patient support platform of a commercial breast MRI system that is used to perform breast lesion localization using MR guidance. The RF coil in this system can be removed from the interstitial space of the patient support platform. An inexpensive biocompatible thermoplastic mesh that conforms to the patient's breast surface can be used to immobilize the breast tissue during the MRI exam. A study conducted on thermoplastic meshes used in MR-guided biopsy reported no imaging artifacts [26]. The study showed that any MR signal from the thermoplastic material appeared outside of the skin surface.

An MRI system such as the one described above would enable MR and microwave data to be collected with the breast in the exact same position, thereby solving the co-registration problem. A system that integrates a 3D microwave sensor array into the interstitial space of the MRI patient support platform is needed. The size of the microwave sensor array is constrained by the vertical limited extent of that interstitial space. If the sensor is to facilitate a dense spatial sampling of scattered fields, the antenna array elements are required to occupy a small footprint in relation to the overall surface of the breast. It is also highly desirable to fill the void between the array and the breast with a suitable biocompatible immersion



Figure 2.1 Photograph of the patient support platform of a commercial breast MRI system.

medium that is sufficiently well impedance matched to the thermoplastic material at the frequencies of interest. This impedance match would simplify the reconstruction because the thermoplastic layer may be neglected by the imaging solution without sacrificing imaging quality.

### 2.3 Thermoplastic materials for immobilizing breast tissue

Meshes constructed from perforated thermoplastic materials have been used as immobilization devices in interventional breast MRI applications such as MR-guided preoperative localization or MR-guided needle biopsy [26, 27]. One example of a thermoplastic polymer is polycaprolactone (PCL). This thermoplastic material is rigid at room temperature but softens and becomes malleable upon being immersed in a warm water bath of 57 °C. In its malleable state, a thermoplastic mesh easily conforms to the pendulous breast. Once the material cools back down to room temperature, its rigidity is restored. PCL-based polymers are also low cost and biodegradable [39]. Such material characteristics are important for the intended application wherein the patient-conformed thermoplastic mesh would be discarded after a single use.

The dielectric properties of PCL-based materials and films have been characterized at frequencies up to 10 MHz [40–42]. These materials exhibit stable dielectric properties in terms of their pre-heated and cooled-down states [40].

## **2.4 Antenna array elements for microwave breast imaging**

### **2.4.1 Desired features of a 3D microwave sensor array**

The 3D microwave sensor array that encloses the breast of a prone patient is ideally composed of a large number of elements to permit dense 3D spatial sampling of scattered fields. Thus each antenna element should occupy a very small footprint relative to the total surface area of the breast. Second, it is advantageous for the antennas to operate efficiently at multiple frequencies. Solving the inverse scattering problem at a single frequency poses inherent challenges because the stability and resolution of the imaging algorithm represent competing demands in choosing the frequency [43]. In contrast, the advantages of both lower and higher frequencies are retained with a multi-frequency approach [44]. The use of a parametric model to reconstruct the frequency-dependent dielectric properties reduces the ill-posed nature of the inverse problem [45] and computational burden of the multi-frequency algorithm [17]. In particular, antenna elements that operate within the frequency range of 0.5-3.5 GHz are desired. Frequencies below and above this range are non-optimal in terms of spatial resolution and penetration depth, respectively. In addition, a multi-band antenna operating in a biocompatible immersion medium that provides high gain at the design frequencies will in turn yield higher signal-to-noise ratio and imaging sensitivity. Finally, the antenna design should be simple enough to model efficiently in the reconstruction algorithms.

### **2.4.2 Prior antenna array element designs for microwave breast imaging systems**

The most widely used radiating elements in microwave tomography systems are monopole and dipole antennas due to their ease of fabrication and their simplicity of modeling in the

forward solution of the inverse problem [2, 3, 46, 47]. Examples of these types of radiators are shown in Figure 2.2. When immersed in a coupling medium they provide a broadband impedance match at the expense of reduced radiation efficiency that increases system loss [48]. Additionally, they are omni-directional radiators, which makes them very sensitive to environmental interference and their performance is highly dependent on the feeding cables.

Table 2.1 compares some of the antennas that have been fabricated and tested for microwave breast tomography systems. All of the antennas presented in Table 2.1, excluding the tapered patch, are difficult to arrange densely in a 3D array designed for the constrained space of an MRI patient support platform.

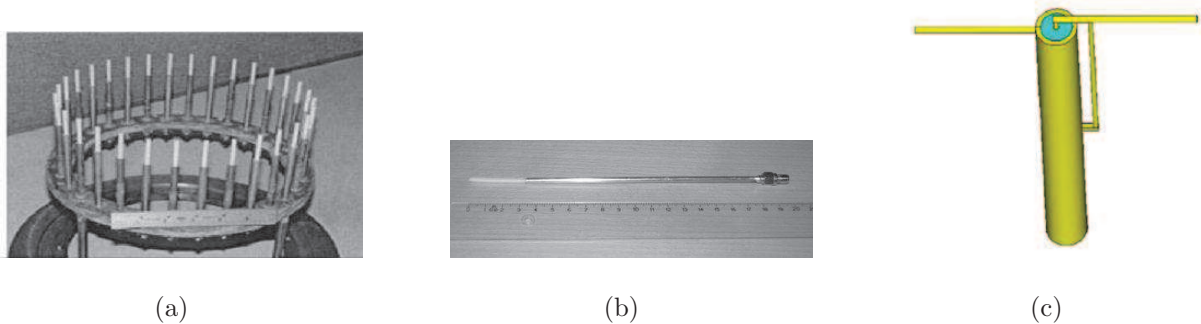


Figure 2.2 Radiating elements most widely used in microwave breast imaging systems. (a) 32 monopole antenna array [1]. (b) Simple monopole antenna consisting of a coaxial cable from which the outer conductor has been stripped [2]. (c) Dipole antenna with a balun to reduce the radiation from the outer conductor of the semirigid coaxial cable [3].

### 2.4.3 Multi-band miniaturized patch antennas for microwave breast imaging

Compact planar antennas have been studied for the last several decades mainly because of the proliferation of smaller mobile communication devices. Microstrip antennas, a class of planar antennas, are characteristically light weight, low-profile, and low-cost. A microstrip antenna may simply consist of a radiating patch of metallization on a grounded dielectric substrate. Comprehensive reviews of compact microstrip antennas have been presented in [50–52].

Table 2.1 Review of antenna elements designed for experimental tomographic microwave breast imaging systems.

Reference	Antenna type	Frequency	Number of antennas
[3] Yu, et al.	dipole	1.74 GHz, 2.7 GHz	2
[2] Rubaek, et al.	monopole	0.3-3.0 GHz	32
[1] Meaney, et al.	monopole	0.3-1.0 GHz	16
[37] Semenov, et al.	waveguides	0.8-1.2, 2.05-2.5 GHz	2
[38] Gilmore, et al.	Vivaldi	3-10 GHz	24
[49] Stang, et al.	tapered patch	2.7 GHz	32

The ground plane backing of microstrip antennas ensures uni-directional radiation. This prevents environmental interference that can occur with omnidirectional radiators, such as dipole antennas. The characteristics of a patch antenna are independent of the coaxial feed cables. This isolation can be exploited to increase the accuracy of modeling these types of antennas in forward simulations. The planar design of a patch antenna also contributes to ease of modeling in simulations that use Cartesian grids.

Miniaturizing techniques used to reduce the size of different types of antennas consist primarily of loading the antenna with lumped elements, using high-dielectric materials or conductors, and using the antenna casing to increase radiation. However, lumped-element loading or modifying the antenna casing can increase the complexity of the design, degrade the efficiency, or limit the bandwidth of the antenna. Rectangular patches that contain embedded slots have been implemented to produce compact antennas. Slot geometries can range from cross slots, rectangular slots, and circular slots. These slots cause meandering of the patch surface currents, which is an effect that generates compact antenna designs with simple topologies. Compact microstrip antennas that achieve dual-band operation by embedding a pair of slots parallel and close to the radiating edges of a meandered rectangular antenna or a bow-tie patch have been realized [53].



Techniques based on rectangular slot-loading can be used to reduce the size of a patch and produce multi-band operation within a specified frequency range [54–64]. Studies have shown that the frequency ratio of a slot-loaded, multi-band patch antenna can be tuned by varying the dimensions of the selected slot used for loading [54–58, 60, 61]. Several examples of single-layer patch antennas loaded with slots of different types and at different locations along the patch have been proposed. Results often include the gain of the slot-loaded patch antenna at its operating frequencies [58–64]. However, no extensive treatment of the trade-off between miniaturization via slot-loading type and location versus gain has been previously presented.

#### 2.4.4 Mutual coupling

One important consideration in the design of a densely populated array is the mutual coupling that may exist between antenna elements. Several researchers have attempted to minimize mutual coupling between array elements of microwave imaging systems [3, 38, 65]. Results presented in [38] showed successful reconstructions of dielectric phantoms by selecting frequencies of antenna operation where the antenna coupling was minimal. In the prototype reported by [3], researchers designed a system that was composed solely of two dipole antennas that were designed to transmit and receive electromagnetic waves to avoid the mutual coupling of antennas in an array. Another group has reported taking advantage of the lossy immersion medium to minimize magnitude and phase errors due to mutual coupling of neighboring monopoles in their microwave tomography system [65].

Despite these efforts, the connection between mutual coupling and successful image reconstruction is not well understood. Strong antenna coupling does tend to change the radiation characteristics of the antenna elements. The ability of the array elements to measure the amount of scattering information available from the breast tissue may also be degraded due to strong mutual coupling.

## Chapter 3

### **Dielectric characterization of a tissue-stabilizing thermoplastic material and biocompatible immersion medium for microwave breast imaging**

We propose the use of a polycaprolactone (PCL)-based thermoplastic mesh as a tissue-immobilization interface for microwave imaging. An investigation of the dielectric properties of two PCL-based thermoplastic materials in the frequency range of 0.5-3.5 GHz is presented. The frequency-dependent dielectric constant and effective conductivity of the PCL-based thermoplastics are characterized using measurements of microstrip transmission lines fabricated on substrates comprised of the thermoplastic meshes. We also characterize the dielectric properties of a vegetable oil – a candidate biocompatible immersion medium for the microwave imaging system. We demonstrate that the PCL-based thermoplastic material and the assumed biocompatible medium of vegetable oil are sufficiently well matched such that the PCL layer may be neglected by the imaging solution without sacrificing imaging quality. These results suggest that PCL-based thermoplastics are promising materials as tissue immobilization structures for microwave imaging applications.

### 3.1 Dielectric properties of PCL-based thermoplastic materials\*

The material used to immobilize the breast during a microwave and MRI scan should be sufficiently malleable to conform to the tissue and yet rigid enough to prevent movement during the imaging procedure. In addition, the material should be relatively low-loss to allow for adequate penetration of the microwave signals into the tissue to achieve the desired results and be well-matched to either the immersion medium or skin to prevent mismatch reflection loss. Several low-loss materials, including liquid crystal polymers [66], polymer-ceramic composites [67], and Parylene-N [68], have been proposed as flexible microwave substrates for conformal applications in microwave engineering. However, while these materials are flexible, they do not retain their shape unless bound or held in place. Thus they are not suitable for our proposed application.

Meshes constructed from perforated thermoplastic materials, such as the one shown in Figure 3.1(a), have been used as immobilization devices in interventional breast MRI applications such as MR-guided preoperative localization or MR-guided needle biopsy [26, 27]. One example of a thermoplastic polymer is polycaprolactone (PCL).

Here, we present an experimental microwave-frequency characterization of the dielectric properties of two commercially available PCL-based thermoplastic materials (shown in Figure 3.1)(b),(c)) in the frequency range of 0.5-3.5 GHz. The frequency range of our study corresponds to the range of interest in current microwave inverse scattering algorithms for breast imaging (e.g., [1, 2, 16–18, 29]). To the best of our knowledge, this represents the first study of the frequency-dependent microwave dielectric properties of a PCL-based thermoplastic. This data is important because it enables an investigation of the potential impact of the immobilization mesh on microwave imaging performance as well as a determination of system features, such as the immersion medium, that minimize that impact.

---

\*This section comprises content from the following published paper: S. M. Aguilar, J. D. Shea, M. A. Al-Joumayly, B. D. Van Veen, N. Behdad, and S. C. Hagness, "Dielectric characterization of PCL-based thermoplastic materials for microwave diagnostic and therapeutic applications," *IEEE Transactions in Biomedical Engineering*, vol. 59, no. 3, pp. 627-633, March 2012.

### 3.1.1 Method of dielectric characterization

We acquired samples of the following two PCL-based thermoplastic materials from Orfit Industries of America: Efficast® 8333Y.3/R and U-Plast™ 8338BL.SO2+/R. These perforated thermoplastic sheets, such as the one shown in Figure 3.1(a) are designed for patient fixation in radiation oncology. The Efficast® sample, shown in Figure 3.1(b), is a 2.0-mm-thick dielectric sheet perforated with 2.8-mm-diameter air holes. The U-Plast™ sample, shown in Figure 3.1(c), is a 2.4-mm-thick dielectric sheet perforated with 1.4-mm-diameter air holes.

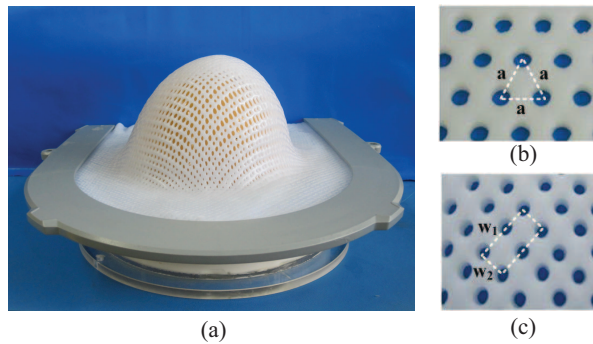


Figure 3.1 Photographs of PCL-based thermoplastic meshes characterized in this study. (a) A U-Plast™ 8338BL.SO2+/R thermoplastic mesh molded to a physical breast phantom. (b) An Efficast® 8333Y.3/R 2.0-mm-thick mesh with 2.8-mm-diameter holes created on a hexagonal lattice with  $a = 5.8$  mm. (c) A U-Plast™ 8338BL.SO2+/R 2.4-mm-thick mesh with 1.4-mm-diameter holes created on a rectangular lattice with  $w_1 = 5.6$  mm and  $w_2 = 2.8$  mm.

Transmission-line methods [69–76] are well suited for characterizing the wideband dielectric properties of thin, rigid material sheets. In such methods, the material under test is used as the substrate in a microstrip transmission line and its dielectric properties are extracted from electrical measurements performed on the line. We adopted this approach to characterize the dielectric properties of the PCL-based thermoplastic materials from 0.5 to 3.5 GHz. We fabricated a total of ten microstrip transmission lines of two different widths (three of each width) on each thermoplastic substrate. We chose transmission line lengths that spanned the entire length of the acquired sample boards. This was done to minimize the

influence of the connector and parasitic parameters on the overall measurement accuracy. The transmission line widths were chosen to cover 2-3 air holes in the transverse direction, thereby ensuring that the measured properties represented volume averages of the bulk material and the air holes. For the Efficast® samples, the widths of the transmission lines were 10 mm and 15 mm; the length of each line was 265 mm. For the U-Plast™ samples, the widths were 5 mm and 10 mm while the common length was 205 mm. Printed-circuit-board (PCB) edge-mount connectors were soldered at the end of each line. Two-port scattering (S-) parameter measurements were carried out over the 0.5-3.5 GHz frequency range using an Agilent E8364 vector network analyzer (VNA).

We developed equivalent circuit models of the transmission lines that take into account the presence of the connectors as well as the parasitic effects of the transitions between the connectors and the transmission lines (see Figure 3.2). Agilent’s Advanced Design System (ADS) [77] was used to simulate these equivalent circuit models. The internal optimization engine in ADS was used to extract parameter values by matching simulated performance to measurement values [78]. The dielectric constant and loss tangent of the substrate in the model were optimized within ADS to achieve a good agreement between the measured S-parameters and those predicted by the equivalent circuits over the frequency range of interest.

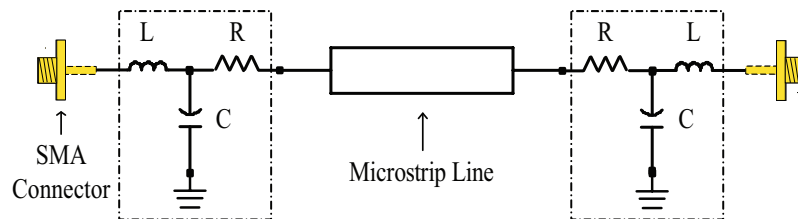


Figure 3.2 Equivalent circuit model of the transmission line configuration. The parasitic elements associated with the coaxial-to-microstrip transition are contained inside the dash-dot-dash boxes ( $L = 0.28$  nH,  $R = 0.05$   $\Omega$ ,  $C = 0.07$  pF).

The parameters of the two PCB edge-mount connectors were optimized to within 10% of the values provided by the manufacturer. We modeled the parasitic effects of the coaxial-connector-to-microstrip transition and connector assembly imperfections using a shunt capacitance,  $C$ , a series inductance,  $L$ , and a series resistance,  $R$ , on each side of the line, as shown in Figure 3.2. Assembly imperfections give rise to a small air gap that exists between the edge of the connector and the edge of the substrate. This gap contains a portion of the center conductor of the edge-mount connector with average dimensions of 1 mm both in diameter and length. Typical values for parasitic impedances of such short wires at microwave frequencies have been reported in [79, 80]. Estimates for the fringing capacitance of a microstrip line located at the edge of a dielectric substrate are also reported in [81]. From these studies, we obtained initial approximate values for the parasitic  $R$ ,  $L$ , and  $C$  elements used in the circuit model. These parameters were optimized in ADS and the resulting parasitic element values were found to be  $R = 0.05 \Omega$ ,  $C = 0.07 \text{ pF}$ , and  $L = 0.28 \text{ nH}$ .

The substrate dielectric properties extracted from the ADS simulation of the transmission line models include the effects of the air-hole perforations; hence, we refer to the ADS-optimized dielectric constant and loss tangent as  $\epsilon_{avg}$  and  $\tan \delta_{avg}$ , respectively. The ADS optimization was performed using both the magnitude and the phase of the  $S_{21}$  and  $S_{11}$  measurements. The  $S_{21}$  fit was given a 10:1 priority weighting relative to the  $S_{11}$  fit because the imperfect symmetry in the assembly of the connectors on each side of the line gives rise to unequal reflection coefficients (e.g.  $S_{22}$  and  $S_{11}$ ) from the two ports. The values of the substrate dielectric properties in each transmission line model were swept using the internal optimization engine of ADS until the best achievable optimization goal was obtained. Values for the dielectric properties were extracted for frequency bands of 0.5 GHz across the desired frequency range of 0.5-3.5 GHz.

The dielectric properties of the bulk thermoplastic are of greater fundamental importance than the volume-averaged properties of the mesh for two reasons. First, it is unlikely that the holes in the thermoplastic mesh will remain air-filled in the intended application involving an immersion liquid. Second, several different hole patterns are available from manufacturers of

PCL-based thermoplastic meshes, and the volume-averaged dielectric properties depend on the hole pattern. Knowledge of the dielectric properties of the bulk thermoplastic enables one to predict the average dielectric properties of any mesh configuration. We extracted the dielectric properties of the bulk thermoplastic material from the average dielectric properties using a volumetric averaging principle [82]. The hole patterns in the thermoplastic meshes repeat themselves in unit cells as shown in Figure 3.1(b) and (c). The unit cells are triangular (equilateral) for the Efficast® sample and rectangular for the U-Plast™ sample. Thus, the relationship between the measured volume-averaged properties of the perforated Efficast® sample and the underlying properties of the bulk thermoplastic material,  $\epsilon_r$  and  $\tan \delta$ , is as follows:

$$\epsilon_{avg} = \frac{\pi}{2\sqrt{3}}\left(\frac{D}{a}\right)^2 + \epsilon_r\left(1 - \frac{\pi}{2\sqrt{3}}\left(\frac{D}{a}\right)^2\right) \quad (3.1)$$

$$\tan \delta_{avg} = \tan \delta\left(1 - \frac{\pi}{2\sqrt{3}}\left(\frac{D}{a}\right)^2\right) \quad (3.2)$$

where  $D = 2.88$  mm is the hole diameter and  $a = 5.8$  mm is the length of the side of the unit cell triangle. The first and the second terms in equation (3.1) correspond to the contribution of air and the bulk thermoplastic material, respectively. Taking into account that air is lossless, equation (3.2) represents the loss of the bulk thermoplastic material. Similarly, the average properties of the U-Plast™ sample are related to the properties of the thermoplastic material as follows:

$$\epsilon_{avg} = \frac{\pi}{2}\left(\frac{D^2}{w_1 \times w_2}\right) + \epsilon_r\left(1 - \frac{\pi}{2}\left(\frac{D^2}{w_1 \times w_2}\right)\right) \quad (3.3)$$

$$\tan \delta_{avg} = \tan \delta_{avg}\left(1 - \frac{\pi}{2}\left(\frac{D^2}{w_1 \times w_2}\right)\right) \quad (3.4)$$

where  $D = 1.4$  mm is the hole diameter and  $w_1 = 2.88$  mm and  $w_2 = 5.6$  mm are the sides of the rectangle. The loss tangent of the thermoplastic material was converted to an effective conductivity,  $\sigma$ .

### 3.1.2 Validation and results

Our equivalent circuit model was tested and validated using S-parameter measurements taken from transmission lines patterned on a known Rogers 5880 board. The resulting extracted dielectric properties for the Rogers 5880 board were  $\epsilon_r = 2.203$  and  $\tan \delta = 0.00099$  for the frequency range of 0.5-3.5 GHz. The manufacturer specifies values of  $\epsilon_r = 2.20 \pm 0.02$  and  $\tan \delta = 0.0009$  for frequencies up to 10 GHz. This high level of agreement in the dielectric properties confirms the validity of the equivalent circuit model, namely, the connector parameters as well as the values of the parasitic elements-used in the ADS-based dielectric-properties optimization scheme.

The measured and simulated  $S_{21}$  curves for one of the 205-mm-long, 10-mm-wide transmission lines on the Efficast® sample are shown in Figure 3.3. This representative example illustrates the excellent agreement obtained between measurement and simulation for all of the transmission line samples. The resulting dielectric properties,  $\epsilon_r$  and  $\sigma$ , of both PCL-based thermoplastic materials are presented in Figure 3.4. Each data point represents the mean value of the results (dielectric constant or effective conductivity) from the ten transmission lines fabricated on each of the two material samples. The vertical bars span the maximum and minimum values at specific frequencies.

The mean value of the dielectric constant of the Efficast® PCL-based material ranges between 3.23 and 3.24 over the 0.5-3.5 GHz frequency range. For the U-Plast™ material, the mean dielectric constant ranges between 3.20 and 3.22. The mean conductivity ranges from 0.014 (S/m) at 0.5 GHz to 0.048 (S/m) at 3.5 GHz for Efficast® and from 0.013 (S/m) (0.5 GHz) to 0.049 (S/m) (3.5 GHz) for U-Plast™. The variation about the mean dielectric constant was less than 1.4% for Efficast® and 3.5% for U-Plast™ over the entire



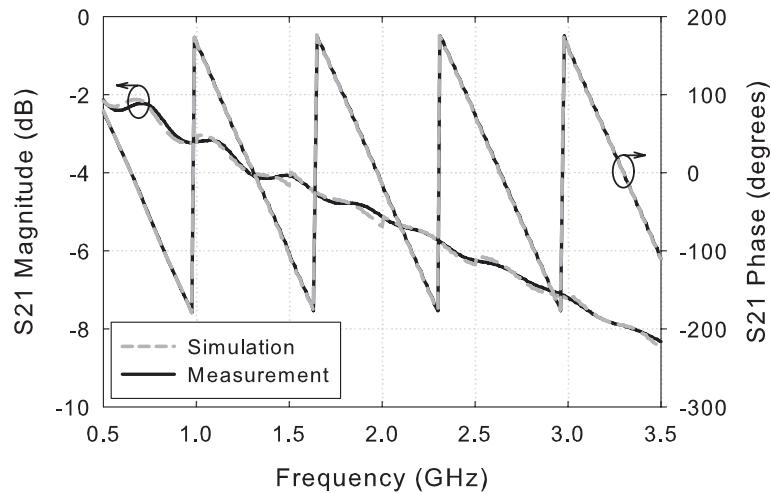


Figure 3.3 Measured  $S_{21}$  for a microstrip transmission line (width of 10 mm, length of 265 mm) fabricated on a substrate comprised of a perforated PCL-based thermoplastic (Efficast® 8333Y.3/R), compared with the ADS-computed  $S_{21}$  for a model of the microstrip with optimized substrate dielectric properties.

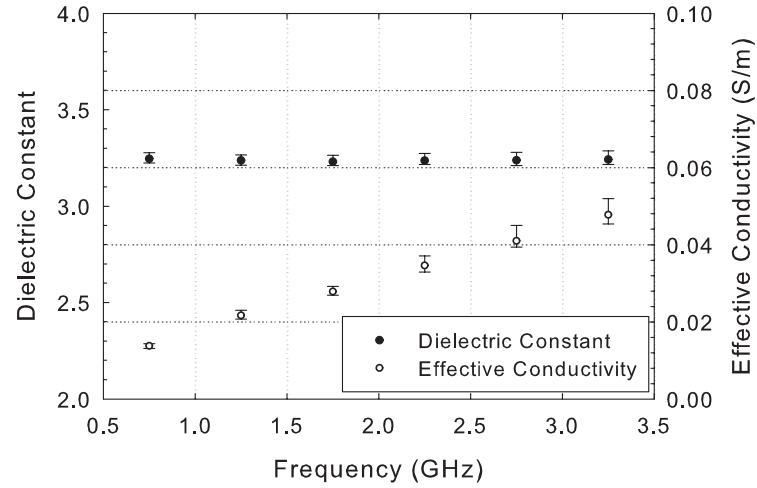
frequency range of interest. This measurement variability is attributed to small differences in the assembly processes for each of the transmission lines used to extract these properties.

### 3.1.3 Summary

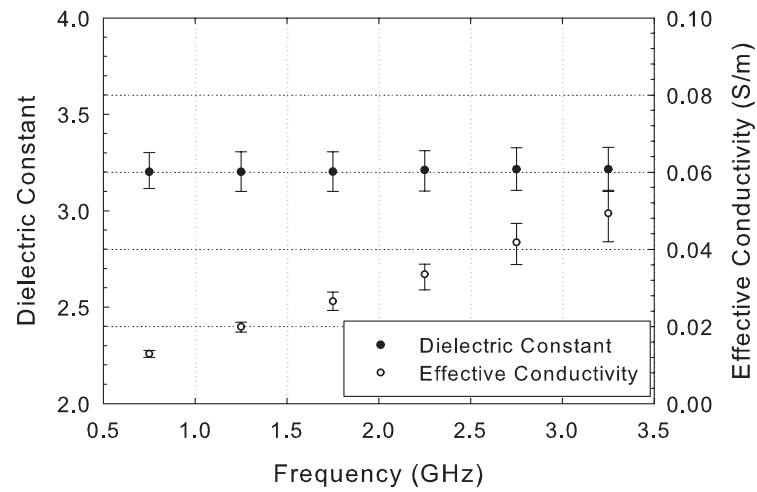
The dielectric properties of commercially available PCL-based thermoplastic materials have been experimentally characterized in the microwave range of 0.5-3.5 GHz using transmission line measurements. We determined that the dielectric constant of the PCL-based thermoplastics is  $3.22 \pm 0.02$  over the entire frequency range and the conductivity ranges from  $0.0133 \pm 0.0004$  (S/m) at 0.5 GHz to  $0.0485 \pm 0.0008$  (S/m) at 3.5 GHz.

## 3.2 Dielectric properties of a biocompatible immersion medium

We propose the use of safflower oil as a biocompatible immersion medium for microwave breast imaging. This immersion medium fills the void between the microwave sensor array and the breast and potentially minimizes the impact of the immobilization mesh on microwave imaging performance. Here, we present an experimental microwave-frequency



(a)



(b)

Figure 3.4 Dielectric properties of two PCL-based thermoplastic materials, as a function of frequency, obtained from microstrip transmission-line measurements. The properties correspond to those of the bulk thermoplastic, after accounting for the air holes (i.e., perforations) in the commercial samples of (a) Efficast® 8333Y.3/R and (b) U-Plast™ 8338BL.SO2+/R.

characterization of the dielectric properties of safflower oil in the frequency range of 0.5-3.5 GHz.

We hypothesize that this immersion medium is well matched in impedance to the PCL-based tissue-stabilizing thermoplastic material characterized in Section 3.1. The extent of the impedance match between the medium and the thermoplastic material is investigated using an experimental test bed. The experimental findings suggest that the thermoplastic mesh will have no discernible impact on the reconstructed images. This is confirmed by a complementary numerical investigation (conducted by J.D. Shea) involving a realistic numerical breast phantom with and without the presence of a thin thermoplastic material layer enveloping the breast.

### 3.2.1 Method of dielectric characterization

We characterized the dielectric properties of the biocompatible immersion medium using an Agilent 85070D dielectric probe kit [83] and E8364 vector network analyzer (VNA). We conducted complex permittivity measurements on oil samples in small glass beakers. Three dielectric measurements were made by completely immersing the probe in the oil. Data was taken in the frequency range of 0.5-10 GHz and the results at each frequency were averaged. We also studied the properties of oil as a function of the time it had been exposed to air by making measurements on samples with different time exposures.

### 3.2.2 Measurement results and data fitting

Figure 3.5 shows measured relative permittivity and effective conductivity of three oil samples over a frequency range of 0.5-3.5 GHz. The results indicate that both the relative permittivity and effective conductivity of the medium remain stable even when exposed to air for up to two years.

Dispersion models are commonly used as compact representations of frequency-dependent dielectric properties. Here, we develop several such models that are valid for safflower oil over the frequency range of interest (0.5-3.5 GHz). Since the accuracy of the probe increases

at higher frequencies for materials with low relative permittivity values (e.g.,  $\epsilon_r$  in the range of 2-5) [83], our general strategy was to incorporate higher frequency data content into the curve-fitting procedure.

Our first approach to curve-fitting the measured data was to use a first order Debye model over a high frequency range of 5-10 GHz. Over this frequency range the accuracy of the probe for  $\epsilon_r$  varies from 8%-5%. Using a first order Debye model, the complex permittivity as a function of frequency can be expressed as:

$$\epsilon_r(\omega) = \epsilon_\infty + \frac{\epsilon_s - \epsilon_\infty}{1 + j\omega\tau} + \frac{\sigma_s}{j\omega\epsilon_o}. \quad (3.5)$$

Here  $\tau$  is the relaxation time constant,  $\epsilon_s$  and  $\epsilon_\infty$  are the relative permittivity at DC and very large frequencies, respectively,  $\epsilon_o$  is the permittivity of free space, and  $\sigma_s$  is the static conductivity [84].

We use a least-squares fit of the first order Debye model to the average experimental data over the frequency range of interest. The fitting parameters are  $\epsilon_s$ ,  $\epsilon_\infty$ ,  $\tau$  and  $\sigma_s$ . These parameters were modified slightly within the range of experimental uncertainty of the probe to obtain the best fit between simulation and measurement data of a dual-band miniaturized antenna designed to operate in the oil immersion medium [85]. The resulting Debye parameters are as follows:  $\epsilon_\infty = 2.24$ ,  $\epsilon_s = 2.97$ ,  $\sigma_s = 0$  (S/m), and  $\tau = 5$  ps. Figure 3.6 shows the dielectric properties of this first order Debye model fit to the average measurement data.

Our second approach was to curve-fit the measured data over a frequency range of 0.5-5 GHz. This approach still satisfies our general strategy of curve-fitting given that we include data content in our frequency range of interest (0.5-3.5 GHz) as well as at higher frequencies. Again, we chose to fit a first order Debye model to the measured data. Figure 3.7 shows the dielectric properties of the first order Debye model fit to measured data of the safflower oil over this frequency range. The resulting Debye parameters are as follows:  $\epsilon_\infty = 2.54$ ,  $\epsilon_s = 2.97$ ,  $\sigma_s = 0.01$  (S/m), and  $\tau = 30.53$  ps.

Finally, to improve the closeness of the fit, a second order dispersion model based on a general polynomial formulation [86] was employed. This second order dispersion model can be expressed as:

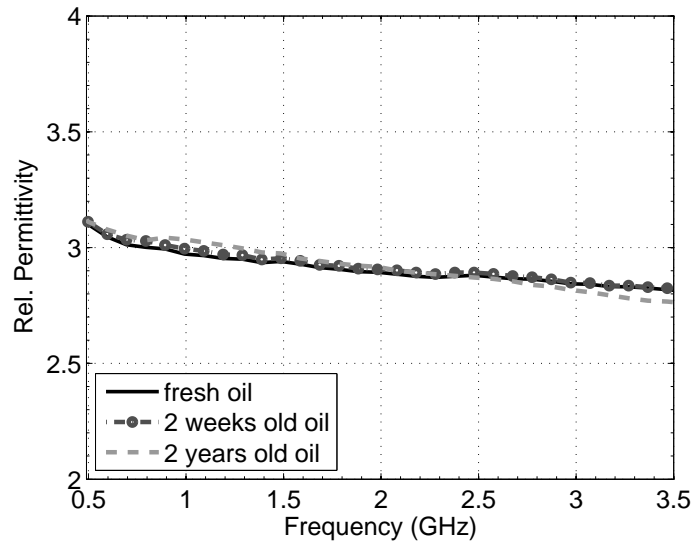
$$\epsilon_r(\omega) = \epsilon_\infty + \frac{\beta_0 + j\omega\beta_1}{\alpha_0 + j\omega\alpha_1 - \omega^2}. \quad (3.6)$$

The fit was performed to data over the frequency range of 0.5-5 GHz. The resulting second order dispersion model parameters are as follows:  $\epsilon_\infty = 2.15$ ,  $\alpha_0 = 195.47 \times 10^{18} \text{ s}^{-2}$ ,  $\alpha_1 = 88.20 \times 10^9 \text{ s}^{-1}$ ,  $\beta_0 = 292.62 \times 10^{18} \text{ s}^{-2}$ ,  $\beta_1 = 63.83 \times 10^9 \text{ s}^{-1}$ . Figure 3.8 shows the relative permittivity and effective conductivity of the second order general dispersion model fit to measured data of the safflower oil over the frequency range of 0.5-5 GHz. This model provides a closer fit to the measured dielectric properties of the safflower oil in our frequency range of interest. Furthermore, the model makes it possible to incorporate highly accurate dielectric properties values into numerical simulations that involve the vegetable-oil-based immersion medium.

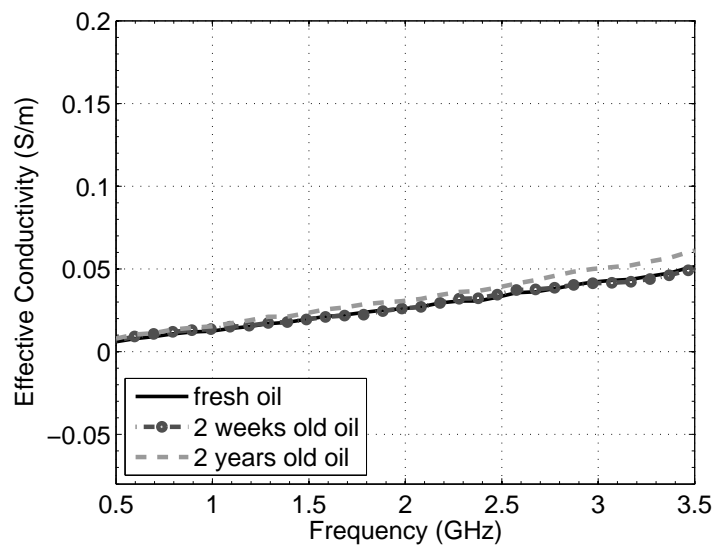
### 3.2.3 Impedance match between PCL-based thermoplastic material and immersion medium

We experimentally studied the impedance match of the proposed tissue-immobilizing thermoplastic materials and the vegetable-oil-based immersion medium. We used a pair of dual-band miniaturized antennas that operate at 1.34 GHz and 2.87 GHz (see Chapter 4) immersed in the oil medium and separated by 10 cm. Figure 3.9 shows the measured transmission coefficients  $S_{21}$  with a thin layer ( $\sim 0.2$  cm) sheet of the thermoplastic mesh placed between the opposing antennas, at a distance of 5 cm from each. We observe that the solid curve is indistinguishable from the dash-dotted and dashed curves at the two resonant frequencies.

We also calculated the difference between the transmission coefficient with the thermoplastic mesh (denoted as  $S_{21\_a}$ ) and that without the mesh (denoted as  $S_{21\_b}$ ). For this experiment the thermoplastic layer was placed  $\sim 4$  cm from each antenna. The difference was

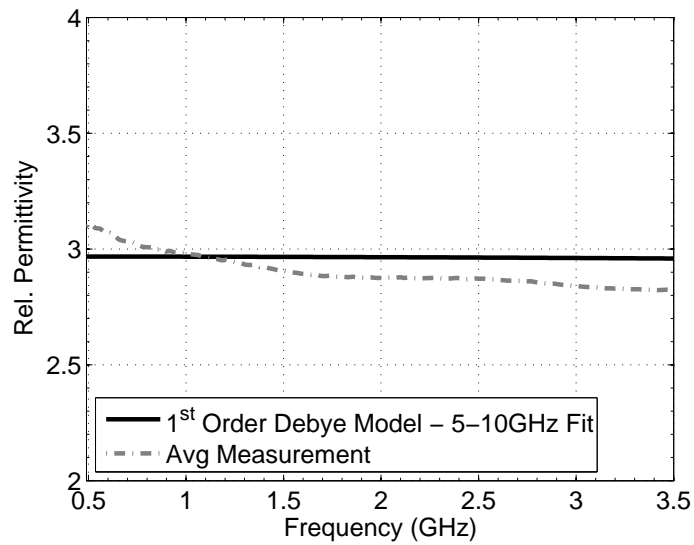


(a)

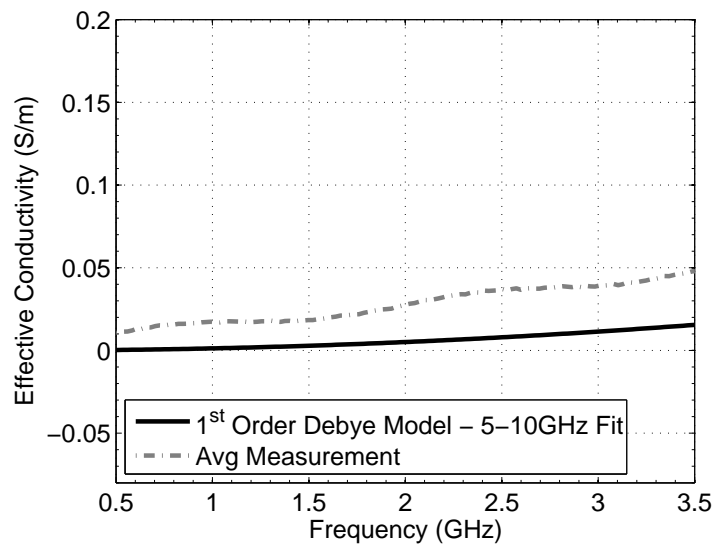


(b)

Figure 3.5 Comparison of the dielectric properties of safflower oil with varying time exposure to air. (a) Relative permittivity and (b) effective conductivity of safflower oil as a function of frequency. Each curve represents the average properties of three different measurements of the same sample.

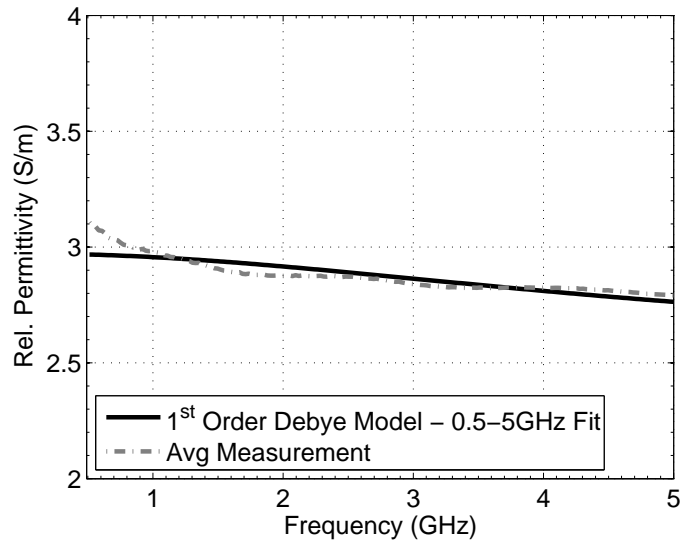


(a)

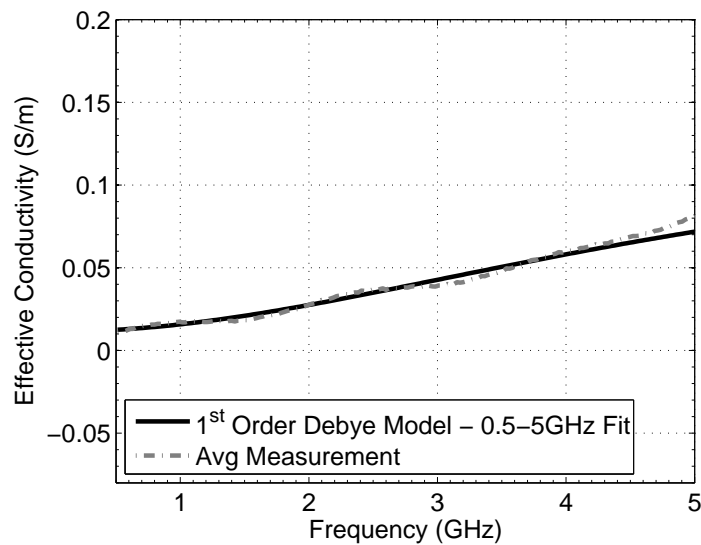


(b)

Figure 3.6 Comparison of first order Debye model fit with measured dielectric properties of safflower oil samples. The Debye model was fit to measured oil dielectric properties in the frequency range of 5-10 GHz. (a) Relative permittivity and (b) effective conductivity as a function of frequency. Dash-dot line represents the average properties of three different measurements of the same sample.



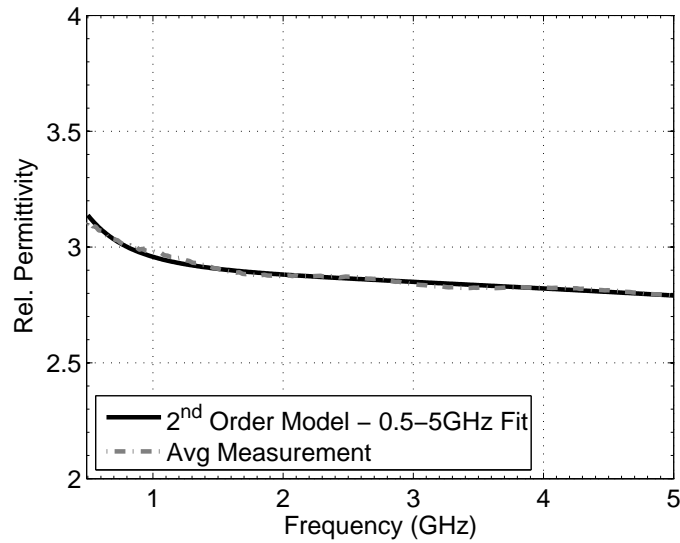
(a)



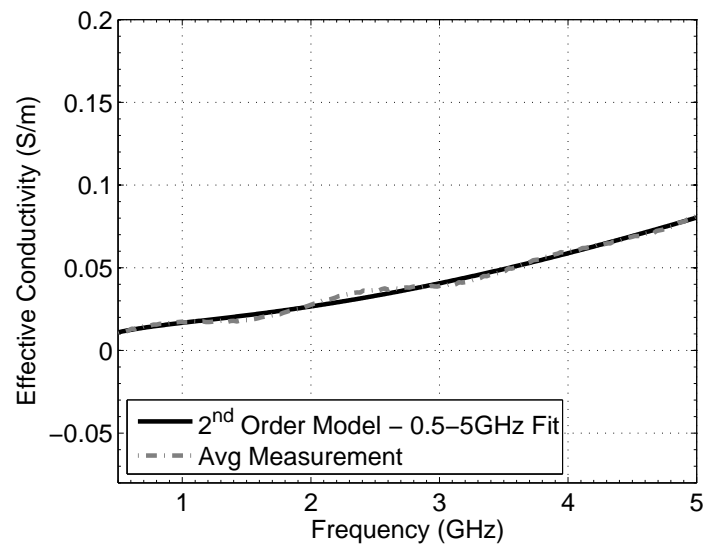
(b)

Figure 3.7 Comparison of first order Debye model fit with measured dielectric properties of safflower oil samples. The Debye model was fit to measured oil dielectric properties in the frequency range of 0.5-5 GHz. (a) Relative permittivity and (b) effective conductivity as a function of frequency. Dash-dot line represents the average properties of three different measurements of the same sample.





(a)



(b)

Figure 3.8 Comparison of second order general dispersion model fit with measured dielectric properties of safflower oil samples. The second order model was fit to measured oil dielectric properties in the frequency range of 0.5-5 GHz. (a) Relative permittivity and (b) effective conductivity as a function of frequency. Dash-dot line represents the average properties of three different measurements of the same sample.

calculated on a dB scale as  $20\log(|S_{21\_a}| - |S_{21\_b}|)$ . The results are presented in Figure 3.10 for two thermoplastic materials, namely an Efficast® 8333Y.3/R mesh and a U-Plast™ 8338BL.SO2+/R mesh. We also measured the difference between two  $S_{21}$  sweeps without thermoplastic layer present (dash-dot curve). This measurement enables us to assess the noise floor of the measurement system. The noise floor is slightly below -80 dB.

For the Efficast® mesh, the difference between both  $S_{21}$  values at 1.34 GHz and 2.87 GHz is -72.01 dB and -76.35 dB, respectively. For the U-Plast™ mesh, the difference between both  $S_{21}$  values at 1.34 GHz and 2.87 GHz is -66.65 dB and -78.29 dB, respectively. These values demonstrate that the difference between two transmission sweeps, one in which the thermoplastic layer is present and one in which it is not, is negligible. The immersion medium and thermoplastic mesh are closely impedance matched, making the thermoplastic mesh invisible to the microwaves.

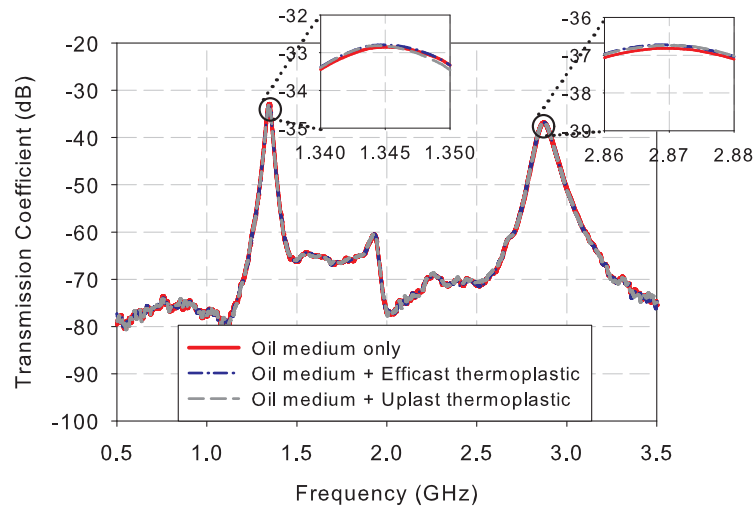
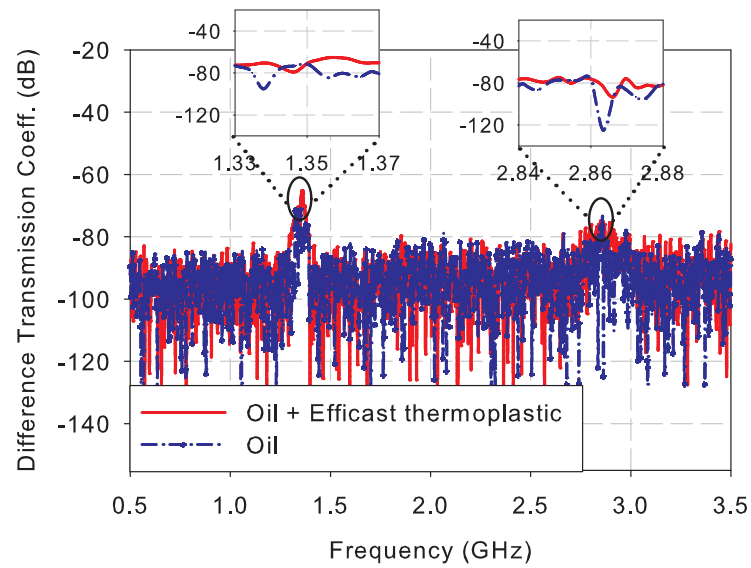
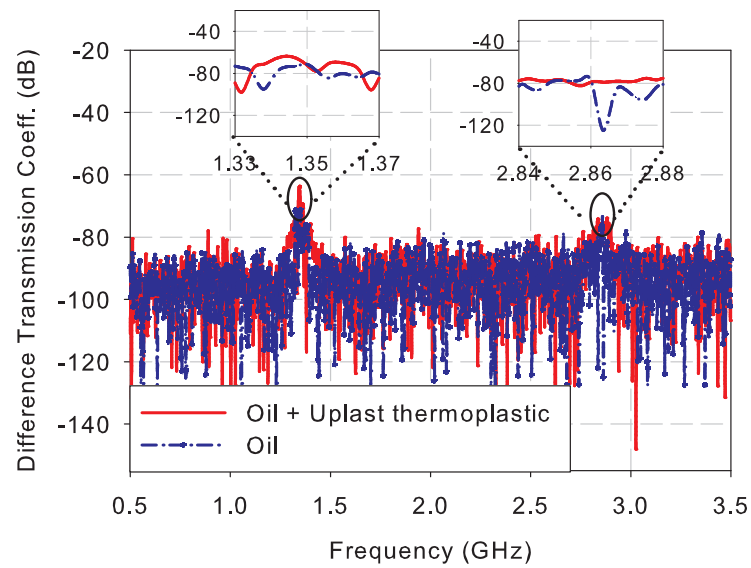


Figure 3.9 Measured transmission coefficients of a two-antenna system demonstrating the invisibility of the thermoplastic mesh in oil. The two dual-band miniaturized patch antennas are immersed in safflower oil and separated by 10 cm.



(a)



(b)

Figure 3.10 Difference between the measured transmission coefficients  $S_{21}$  of a two-antenna system with and without a thermoplastic mesh in oil. The two dual-band miniaturized patch antennas are immersed in safflower oil and separated by 8 cm. Difference of the  $S_{21}$  for (a) an Efficast® 8333Y.3/R mesh in oil and for an (b) U-Plast™ 8338BL.SO2+/R mesh in oil. The dash-dot line corresponds to the case when no thermoplastic sheet is present.

### 3.2.4 Impact of the thermoplastic mesh on microwave breast imaging

During the measurement of a breast by a microwave imaging system, any surrounding objects illuminated by the array may scatter the waves strongly enough to introduce artifacts in the resulting images if those objects are not properly accounted for. In general, any materials used for tissue immobilization must be imaged along with the breast, redacted from the data via some calibration scheme, or included in the propagation model of the imaging solution. All of these options add significant complexity to the imaging algorithm. However, if the dielectric properties of the immobilizer are closely matched to the immersion medium into which the array and breast are placed, the scattering from the immobilizer may fall below the sensitivity of the measurements making any resulting imaging artifacts negligible.

The dielectric characteristics results reported here were used by another researcher in our group (J.D. Shea) to investigate the impact on microwave breast imaging of a PCL-based thermoplastic material used to immobilize the breast in an immersion medium comprised of vegetable oil. A numerical test bed was used in order to isolate the effect of the thermoplastic immobilizer; such an investigation cannot be conducted in the less-controlled environment of an experimental test bed. The numerical test bed was based on the down-sampled Class 2 (scattered fibroglandular) breast phantom and dipole array described in a previous imaging study [6]. In addition, a conformal layer of 2-mm-thick thermoplastic material was placed over the surface of the skin region of this phantom. The dielectric properties of the thermoplastic material were assumed to be  $\epsilon_r = 3.24$  and  $\sigma = 0.031$  S/m. The dielectric properties of the oil immersion were assumed to be dispersive with first order Debye parameters  $\epsilon_s = 2.97$ ,  $\epsilon_\infty = 2.72$ , and  $\tau_p = 15$  ps [85]. We modeled the thermoplastic immobilizer as a solid layer without any perforations. We consider this to be a worst-case test bed because it creates the largest expected impedance mismatch between the immersion medium and the immobilizer. In practice, the average dielectric properties of a perforated thermoplastic layer

(with either air- or oil-filled holes) will provide a better match to the properties of the oil immersion than that assumed here.

The inverse scattering algorithm described in [29] was applied to the data acquired from the numerical phantom with and without the conformal thermoplastic layer. In both cases the thermoplastic was excluded in the forward model of the imaging solution and instead assumed that the immersion medium extended to the skin surface. Under these forward-model assumptions, any scattering from the thermoplastic layer that is on the order of the level of scattering from the interior breast tissue structures will manifest as artifacts in the image of the interior volume. Such artifacts would occur because the imaging algorithm seeks to minimize any residual scattering between measurements of the reconstruction and the actual object.

Coronal cross-sections of the resulting three-dimensional images of the phantom with and without the thermoplastic layer are shown in Figure 3.11. Any differences between the reconstructed dielectric-properties profiles for the two cases are imperceptible. This result suggests that the PCL-based thermoplastic material and vegetable oil are sufficiently well matched such that the thermoplastic layer presents a negligible amount of scattering and may therefore be neglected by the imaging solution.

### 3.2.5 Summary

In these experiments we characterized the dielectric properties of an immersion medium comprised of safflower oil from 0.5-3.5 GHz. We found that a second order general dispersion fit to the measured dielectric properties of oil provides a highly accurate model of the properties in our frequency range of interest. This second order model makes it possible to incorporate accurate values of the dielectric properties of the oil into numerical simulations used in the development of a microwave breast imaging sensor array. In addition, we found that the properties of oil remain stable when exposed to air for an extended period of time

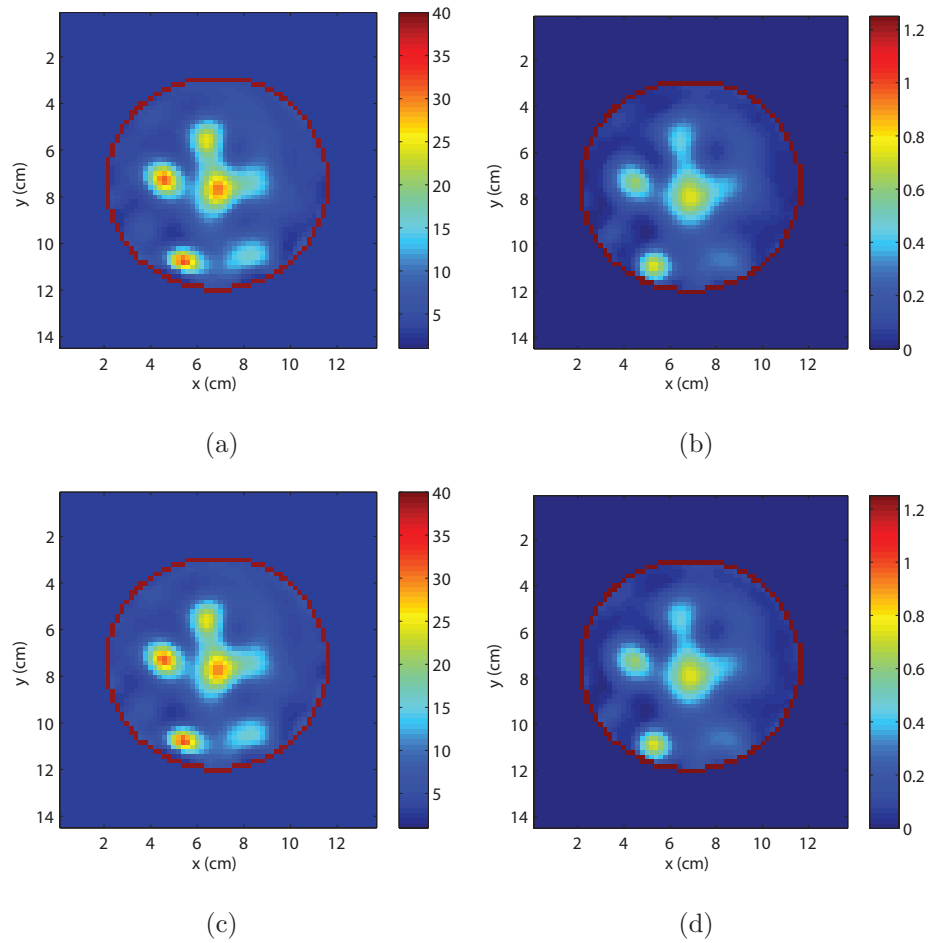


Figure 3.11 Coronal cross-sections of reconstructed three-dimensional dielectric profiles of a Class 2 (scattered fibroglandular) breast phantom. (a)-(b) Images of the phantom with no thermoplastic sheet. (c)-(d) Images of the phantom with the thermoplastic sheet at the skin surface. Dielectric constant, left, and effective conductivity (S/m), right, at 2.0 GHz.

(i.e., up to 2 years). We verified experimentally that the low-loss, biocompatible oil immersion medium provides an excellent impedance match with the tissue-stabilizing thermoplastic material, effectively making the thermoplastic invisible to the microwaves.

## Chapter 4

# Multi-band miniaturized patch antennas for microwave breast imaging

### 4.1 Introduction

We present multi-band miniaturized patch antennas designed for use in a 3D sensor array for microwave breast imaging. Microstrip patch antennas offer a number of desirable features for microwave breast imaging. They are lightweight, low-profile, and low-cost. The ground plane backing ensures unidirectional radiation, thereby minimizing environmental interference. This isolation can be exploited to increase the accuracy of modeling these types of antennas in forward simulations, which are part of the reconstruction algorithm. The planar layout of a rectangular patch antenna is easy to model in simulations that use Cartesian grids.

Techniques based on rectangular slot-loading can be used to reduce the size of a patch and produce multi-band operation within a specified frequency range [54–64]. The frequency ratio of a slot-loaded, multi-band patch antenna can be tuned by varying the dimensions of the selected slot used for loading [54–58, 60, 61]. Several examples of single-layer patch antennas loaded with slots of different types and at different locations along the patch have been proposed. Results often include the gain of the slot-loaded patch antenna at its operating frequencies [58–64]. However, no extensive treatment of the trade-off between miniaturization via slot-loading type and location versus gain has been previously presented.

Here, we investigate performance characteristics of several slot-loaded, multi-band miniaturized patch antenna designs. The antenna elements are designed for a 3D sensor array for

microwave tomography and operate in a biocompatible immersion medium comprised of safflower oil. We examine the effects of varying antenna design parameters, including thickness and permittivity of the dielectric substrates and location of the slots, on the operating characteristics of these antennas. These investigations are first conducted using numerical simulations. Several multi-band miniaturized patch antennas, including tri- and quad-band designs, are fabricated and measured to verify the simulation results. We demonstrate that slot-loading can be used to obtain similar and symmetric radiation patterns, as well as similar gain, at three or four frequencies of operation between 0.5 and 3.5 GHz. The ultimate goal of this work is to determine the usefulness of slot-loaded, multi-band miniaturized patch antenna designs for microwave tomography. We also demonstrate the feasibility of microwave breast imaging with a 3D enclosed antenna array populated with one type of slot-loaded antenna considered in this study.

In Section 4.2, we describe an experimental study to verify and test the performance of a dual-band, miniaturized patch antenna described in [85]. In Section 4.3.1, we discuss the principle of operation and design strategy for multi-band miniaturized patch antennas using slot-loading. In Section 4.3.2, we present the operating characteristics of several multi-band miniaturized patch antenna designs immersed in a biocompatible medium. We also show experimental characterization results of fabricated prototypes of multi-band miniaturized patch antenna elements. Finally in Section 4.3.2.4, we discuss a numerical study of microwave breast imaging using realistic numerical breast phantoms and a 3D antenna array.



## 4.2 Measurement and experimental verification of a dual-band miniaturized patch antenna\*

This section describes a study under which we experimentally verify the performance of a dual-band, miniaturized patch antenna previously proposed [85]. The miniaturized patch antenna was designed for use in a 3D microwave sensor array for breast imaging. This antenna was designed to exhibit dual-band response by exploiting the dominant mode,  $TM_{100}$ , and one of the higher-order modes of the patch antenna,  $TM_{300}$  (see Section 4.3.1 for a detailed description of the antenna design). The experimental results aim to validate the methods employed in the design, measurement, and testing of the antenna.

We fabricated prototypes of isolated antenna elements (Figure 4.1). The antenna elements were patterned on a 32-mil-thick RO4003 substrate (Rogers Corp.) and are probe fed using the center conductor of an SMA connector.

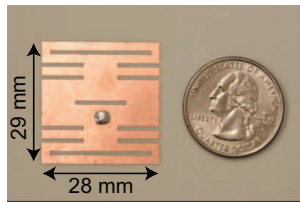


Figure 4.1 Photograph of the fabricated dual-band miniaturized patch antenna.

We measured the reflection and transmission coefficients of the dual-band miniaturized patch antenna. We immersed the fabricated antenna(s) in a 32 cm  $\times$  15 cm  $\times$  11 cm tank filled with safflower oil. The magnitude of the measured  $S_{11}$  frequency response of the antenna is shown in Figure 4.2. Excellent agreement is observed between the simulated and measured reflection coefficients. The fabricated antenna shows multiple bands at 1.34 GHz,

---

\*This section comprises some of the content from the following published paper: M. A. Al-Joumayly, S. M. Aguilar, N. Behdad, and S. C. Hagness, "Dual-band miniaturized patch antennas for microwave breast imaging," *IEEE Antennas and Wireless Propagation Letters*, vol. 9, pp. 268-271, 2010. M. A. Al-Joumayly and S. M. Aguilar contributed equally to the measurement and experimental verification reported in this section.

1.93 GHz, and 2.87 GHz. The slight discrepancy (2% at most) with respect to the simulation results is primarily attributed to the inherent uncertainty in the electrical properties of the single-pole Debye oil model used in the simulations (see Section 3.2.2).

Figure 4.3 shows the measured transmission coefficient of a system of two miniaturized patch antennas facing each other and separated by a distance of 10 cm in the oil. As expected, the system has transmission peaks at  $f_{100}$  and  $f_{300}$ . The transmission peak at  $f_{200}$  is very low ( $-60$  dB), confirming that the radiation pattern has a broadside null at this frequency. This second resonance is not expected to be useful for the intended application where a low-power microwave signal is transmitted. Here we also observe excellent agreement between simulation and experiment.

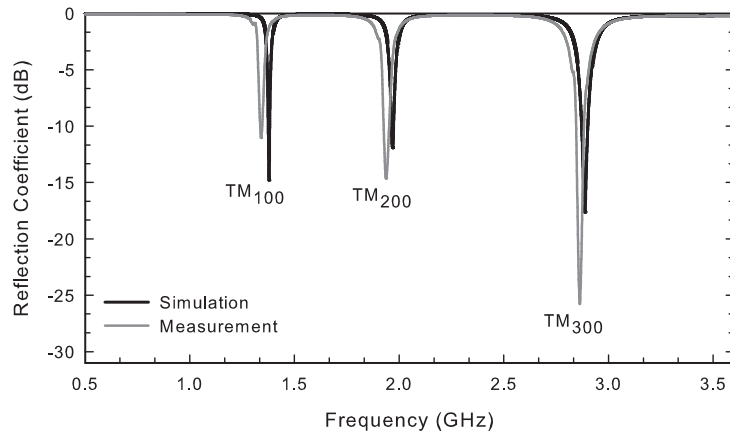


Figure 4.2 Simulated and measured reflection coefficients of the miniaturized patch antenna of Figure 4.1 immersed in safflower oil.

We also characterized the radiation patterns of the miniaturized patch antenna immersed in oil. These antennas are designed to be used in an enclosed cubical array with side lengths on the order of 15 cm. Thus, the measurements were taken at a distance of 15 cm from the patch using half-wavelength dipoles. The measurements were taken at a distance of 15 cm from the patch. Figure 4.4 shows the co-polarized and cross-polarized radiation patterns in the E- and H-planes at 1.34 GHz and 2.87 GHz. The measured cross-pol level is a minimum

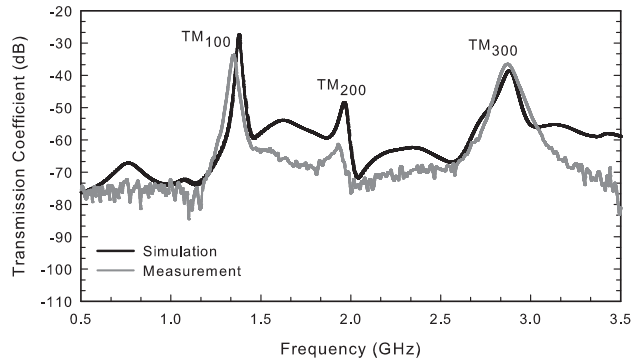


Figure 4.3 Simulated and measured transmission coefficients of a two-antenna system composed of the dual-band miniaturized patch antenna of Figure 4.1 immersed in safflower oil and separated by 10 cm.

of 20 dB lower than co-pol at broadside for both frequencies. We observe better agreement between measurement and simulation in the co-pol radiation patterns than cross-pol. We attribute the greater cross-pol discrepancy to the fact that the very low cross-pol levels are more susceptible to measurement imperfections. As shown in Figure 4.4, the antenna exhibits symmetric and similar radiation patterns at the two operating frequencies.

We compared the performance of our proposed dual-band miniaturized antenna with a dipole, the most widely-used radiators for microwave tomography systems. We fabricated a dipole with the same physical size as our patch. Because of its small size, the first resonance of this dipole occurs at 3.1 GHz. However, the resonant frequency of the first mode of the dual-band patch is 1.34 GHz. Thus, we compared the performance of this small dipole at this same frequency and designed its balun to operate at 1.34 GHz. Figure 4.5 shows the dipole and its balun. Figures 4.6 and 4.7 show the magnitude of the measured reflection and transmission coefficients, respectively, of the small dipole and of the dual-band miniaturized antenna. At 1.34 GHz, we observe that the transmission coefficient of the patch is 20 dB higher than that of the dipole since the patch is impedance matched at this frequency and the dipole is not. Interestingly, however, the balun acts as an impedance transformer for dipole at a frequency of approximately 1 GHz. At this frequency, because of the impedance matching, the transmission is comparable to that of the dual-band miniaturized antenna.

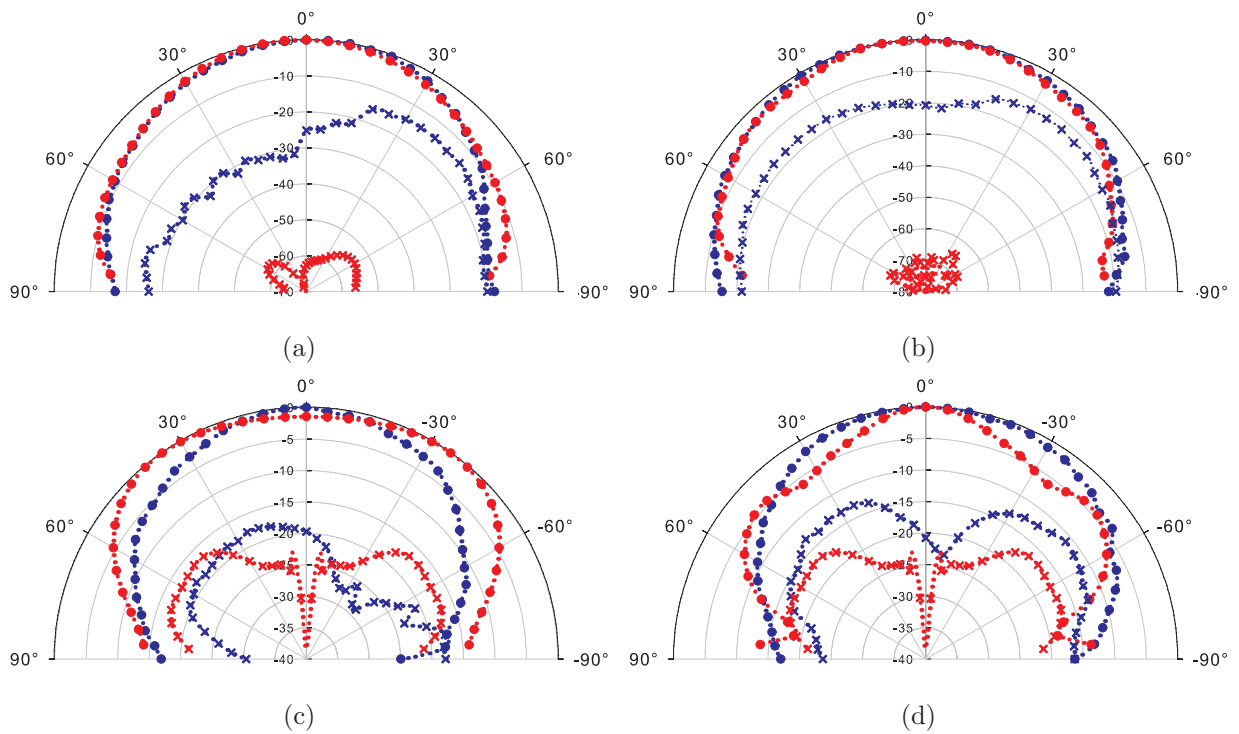


Figure 4.4 Measured and simulated radiation patterns of the dual-band miniaturized patch antenna in oil. The patterns are obtained at a distance of 15 cm from the patch. (a) E-plane at 1.34 and (b) 2.87 GHz. (c) H-plane at 1.34 and (d) 2.87 GHz. Red: simulated data. Blue: measured data. Circle: co-pol. x: cross-pol.

From this study, we can conclude that regardless of the type of antenna used, multi-frequency impedance matching is required to significantly increase the level of transmitted power.



Figure 4.5 Photograph of the fabricated small dipole antenna.

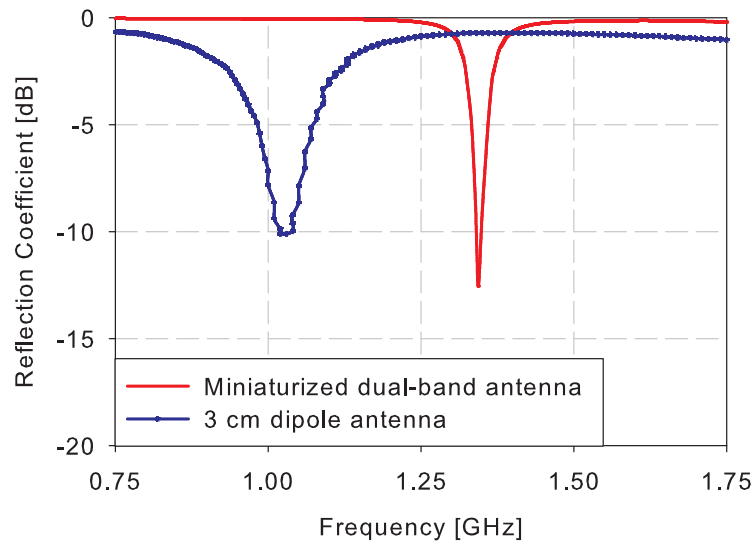


Figure 4.6 Measured reflection coefficients of the dual-band miniaturized patch antenna of Figure 4.1 and a small dipole of Figure 4.5 immersed in safflower oil.

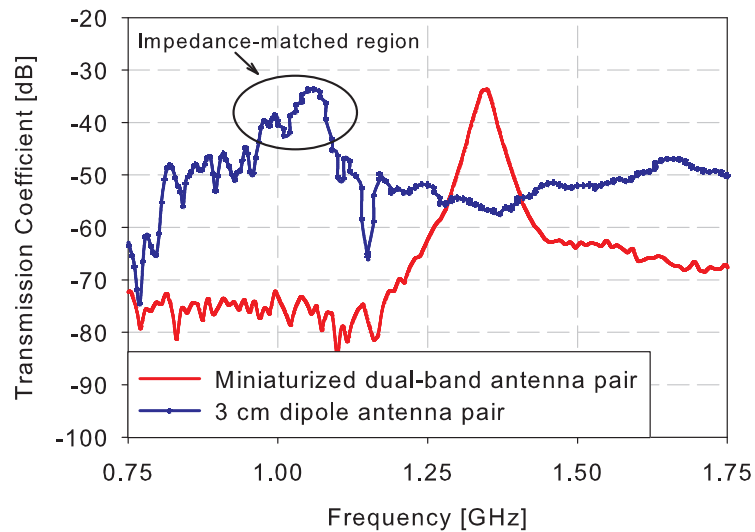


Figure 4.7 Measured transmission coefficients of a two-antenna system composed either of dual-band miniaturized patch antennas or small dipoles. The two antennas are immersed in safflower oil and separated by 10 cm.

## 4.3 Multi-band miniaturized patch antennas\*

### 4.3.1 Antenna design

Our antenna design strategy is to load the patch with judiciously placed slots to shift additional higher-order resonant modes into a desired frequency range while maintaining current distributions similar to that of the dominant mode. This technique enables antenna miniaturization and multi-band operation within the frequency range of interest. We illustrate this process in what follows by summarizing the effect of slot loading, reviewing the design guidelines of a dual-band miniaturized patch antenna previously presented [85], and presenting the proposed designs for multi-band operation.

Figure 4.8 illustrates the topology of a rectangular patch antenna (Figure 4.8(a)), loaded with a series of slots (Figure 4.8(b)-(d)). The slot-loaded patch, shown in Figure 4.8(b), comprising two slots (A and B) parallel to and near the radiating edges, was shown to have a dual-band response [58]. In this structure, the lower frequency of operation is determined by the resonant frequency,  $f_{100}$ , of the dominant mode,  $TM_{100}$ , of a rectangular patch antenna, while the higher operating frequency is determined by the resonant frequency,  $f_{300}$ , of a perturbed higher-order longitudinal mode,  $TM_{300}$ . The addition of these two slots has a slight effect on reducing  $f_{100}$ , since the slots are located close to the current minima of the dominant  $TM_{100}$ , as shown in Figure 4.8(e). The slots have a more significant effect in reducing  $f_{300}$ , since the current for the  $TM_{300}$  mode, shown in Figure 4.8(e), is more significant in the regions of these slots.

Figure 4.8(c) illustrates a slot-loaded patch antenna with an additional slot (C) located at the center of the patch. This center slot increases the electrical lengths of the current paths for the first and third modes, since it is located in a region where both these modes have current maxima, as shown in Figure 4.8(e). Thus, increasing the length of this slot

---

\*This section comprises content from the following manuscript: S. M. Aguilar, et al., "Multi-band miniaturized patch antennas for microwave breast imaging," *IEEE Transactions on Antennas and Propagation*, under preparation.

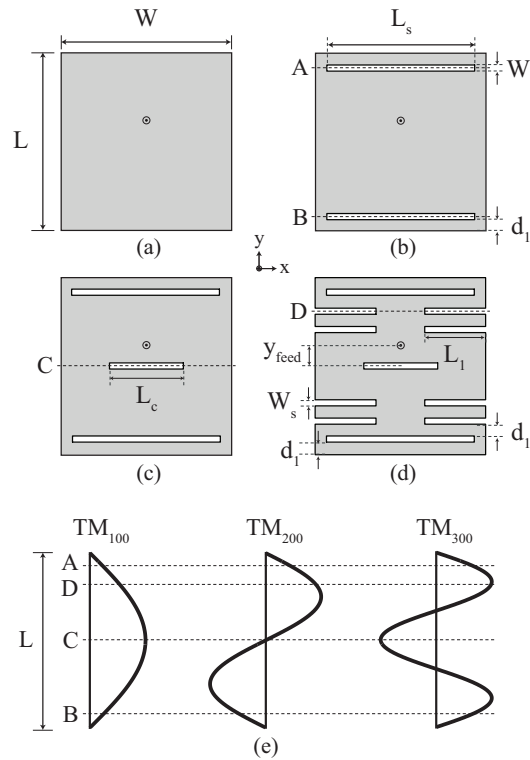


Figure 4.8 Top view of (a) standard patch, (b) slot-loaded patch, (c) slot-loaded patch with center slot, and (d) dual-band miniaturized patch antenna. (e) Schematic of current distributions for the first three longitudinal modes showing where the current is affected by the various slots in (b)-(d).

reduces the operating frequencies of these two bands. The effect is more significant for  $f_{300}$ , since the slot is electrically longer for the  $TM_{300}$  mode. The slot, however, does not have any effect on the second mode,  $TM_{200}$ , since it is located at the current minimum of this mode.\*

Figure 4.8(d) shows the location of nonradiating edge slots (D) that cause the current paths of all longitudinal modes to be further increased, thereby permitting a greater reduction in the length of the patch [85]. The location of these edge slots, as shown in Figure 4.8(e), has a slight effect on the current distribution of the  $TM_{100}$  mode and a more significant effect on the current distribution of the third mode,  $TM_{300}$ . Figure 4.8(d) represents the

---

\*In a rectangular patch, due to anti-symmetric current distributions, the radiation patterns of the second,  $TM_{200}$ , and fourth,  $TM_{400}$ , modes have nulls in the broadside direction. Thus, in this work, the longitudinal modes of interest are the first, third, and fifth.

dual-band miniaturized patch antenna previously reported [85]. The resonant frequencies of the  $TM_{100}$  and  $TM_{300}$  modes of the dual-band miniaturized patch antenna were reduced by 37% and 23% [85], respectively, compared to a conventional dual-band, slot-loaded patch antenna [58].

Figure 4.8(d) and Figure 4.9 show the topology and dimensions of our proposed multi-band miniaturized patch antenna designs. The dual-band miniaturized patch antenna reported in [85] is shown in Figure 4.8(d) for reference. The resonant frequencies of the first three longitudinal modes are affected by the length,  $L_s$ , of the slot added near and parallel to the radiating edge, the length,  $L_c$ , of the slot added at the center of the patch, and the length,  $L_1$ , of the slots added to the nonradiating edges. In Figure 4.8(d), the loading effect of the slots located near the radiating edges of the antenna is limited by the width of the patch [58]. To overcome this limitation, spiral-loaded slots replace the straight slots near the radiating edges, as shown in Figure 4.9(a). The addition of spiral slots has an effect on the dominant mode,  $TM_{100}$ , and two of the higher-order modes of the patch antenna, namely the  $TM_{300}$  and  $TM_{500}$  modes.

The resulting tri-band miniaturized patch antenna, shown in Figure 4.9(a), comprises two spiral slots (length  $L_s$  and width  $W_s$ ) near the radiating edges of the patch, a slot (length  $L_c$  and width  $W_s$ ) located at the center of the patch, and edge slots (lengths  $L_1$  and  $L_2$  and width  $W_s$ ) located at the nonradiating edges of the patch. This tri-band antenna topology offers a great degree of flexibility in choosing the three frequencies of operation over a broad band. For example, the frequency ratio,  $f_{300}/f_{100}$ , can be designed to be as small as 1.0 or as large as 3.0.

The topology of the quad-band miniaturized patch antenna is the same as that of the tri-band patch, except the feed is located off the axis of symmetry of the structure, as shown in Figure 4.9(b). The off-axis feed yields a quad-band response by exciting the dominant orthogonal mode,  $TM_{010}$ . The polarization of this mode is perpendicular to the polarization of the aforementioned longitudinal modes. This, however, is not expected to be a problem for the intended microwave imaging application.



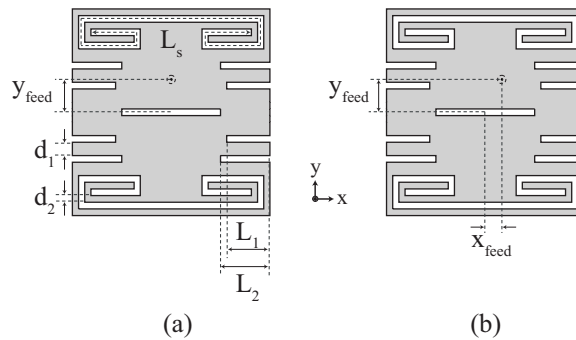


Figure 4.9 Top view of the (a) tri-band, and (b) quad-band miniaturized patch antennas.

The multi-band miniaturized patch antennas are designed to operate in a biocompatible immersion medium comprised of safflower oil. A second-order dispersion model in CST Microwave Studio [86] was fit to the measured frequency-dependent complex permittivity of the safflower oil (see Section 3.2.2).

The dimensions of the dual-, tri-, and quad-band miniaturized patch antennas immersed in oil were tuned in CST Microwave Studio to achieve operating frequencies within the 0.5-3.5 GHz frequency range. The resulting physical dimensions for the dual-band antenna are (in mm):  $W=28$ ,  $L=29$ ,  $W_s=1$ ,  $L_s=24$ ,  $L_c=12$ ,  $L_1=10$ , and  $d_1=2$ . The resulting physical dimensions for the tri-band antenna are (in mm):  $W=32$ ,  $L=33$ ,  $W_s=1$ ,  $L_s=82$ ,  $L_c=16$ ,  $L_1=7$ ,  $L_2=8$ ,  $d_1=2$ , and  $d_2=1$ . The coordinates of the feed location, relative to the center of the patch, are given by (in mm)  $(x_{\text{feed}}=0, y_{\text{feed}}=4.5)$  for the dual-band,  $(x_{\text{feed}}=0, y_{\text{feed}}=8.5)$  for the tri-band, and  $(x_{\text{feed}}=3, y_{\text{feed}}=8.5)$  for the quad-band patch.

The calculated reflection coefficients for the tri- and quad-band antennas, as well as that of the dual-band antenna are shown in Figures 4.10-4.12. The tri-band antenna exhibits  $\text{TM}_{100}$ ,  $\text{TM}_{300}$ , and  $\text{TM}_{500}$  resonances at 1.36 GHz, 1.74 GHz, and 3.03 GHz, respectively. The miniaturization technique used in this patch antenna reduces the operating frequencies of its  $\text{TM}_{100}$ ,  $\text{TM}_{300}$ , and  $\text{TM}_{500}$  modes by 48%, 78%, and 77%, respectively, compared to a rectangular patch antenna occupying the same area. The ratio between the frequencies of operation is  $f_{300}/f_{100} = 1.3$  and  $f_{500}/f_{100} = 2.2$ . A comparison of Figs. 4.10 and 4.11 shows that the combination of the spiral loading on the radiating-edge slots and the wider center

slot not only brings  $f_{500}$  down into the range of interest, but also further reduces  $f_{300}$  by 40% relative to the dual-band antenna. The additional resonance of interest of the quad-band antenna, the  $TM_{010}$ , occurs at 2.38 GHz.

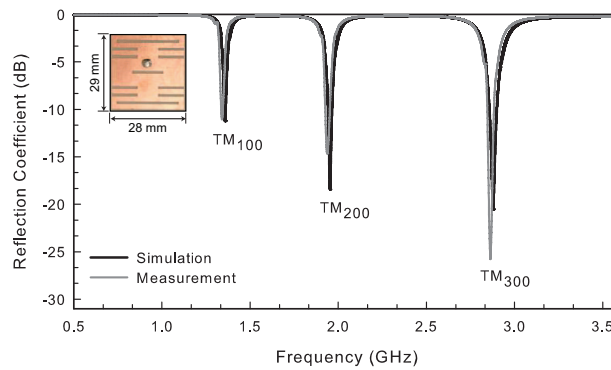


Figure 4.10 Simulated and measured reflection coefficients of the dual-band miniaturized patch antenna of Figure 4.9(a) immersed in safflower oil.

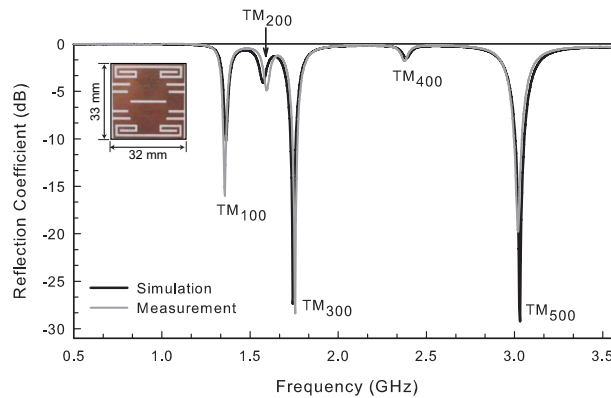


Figure 4.11 Simulated and measured reflection coefficients of the tri-band miniaturized patch antenna of Figure 4.9(b) immersed in safflower oil.

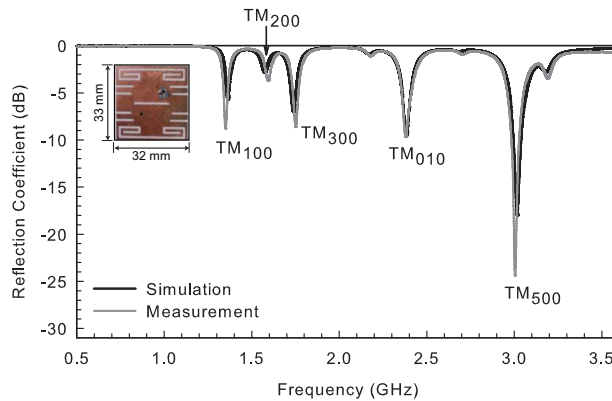


Figure 4.12 Simulated and measured reflection coefficients of the quad-band miniaturized patch antenna of Figure 4.9(b) immersed in safflower oil.

## 4.3.2 Results












### 4.3.2.1 Effect of types of slot-loading

To understand the design trade-offs of slot-loading a patch antenna, we performed numerical simulations of antennas loaded with slots at different locations along the patch. Table 4.1 shows the resonant frequencies and gain of different types of slot-loaded patch antennas.

We considered antenna designs that were patterned on a  $10\text{ cm} \times 10\text{ cm} \times 0.08\text{ cm}$  Rogers RO4003 substrate ( $\epsilon_r = 3.55$ ) and immersed in a biocompatible immersion medium. The designs are based on the antenna geometries given in Figure 4.8(d)-Figure 4.9 ( $L=29\text{ mm}$  and  $W=28\text{ mm}$ ). Slots used in designs based on the antenna geometry shown in Figure 4.8(d) have the same dimensions as the ones used in the dual-band miniaturized patch antenna described in Section 4.3.1. Slots used in designs based on the antenna geometry shown in Figure 4.9 have modified dimensions as follows (dimensions in mm):  $W=28$ ,  $L=29$ ,  $W_s=1$ ,  $L_s=61$ ,  $L_c=14$ ,  $L_1=5$ ,  $L_2=6$ ,  $d_1=1$ , and  $d_2=1$ . The coordinates of the feed location, relative to the center of the patch, are given by (in mm)  $(x_{\text{feed}}=0, y_{\text{feed}}=4.5)$  for the dual-band,  $(x_{\text{feed}}=0, y_{\text{feed}}=7.5)$  for the tri-band, and  $(x_{\text{feed}}=3, y_{\text{feed}}=5.5)$  for the quad-band patch.

The table details the location and number of slots used for loading the patch, the first few resonant frequencies of each type of antenna design, and gain at the resonant frequencies

Table 4.1 Calculated frequencies of operation and gain of several slot-loaded patch antenna types. White:  $TM_{100}$ . Green:  $TM_{300}$ . Blue:  $TM_{500}$ . Red:  $TM_{010}$ .

type of slot-loaded patch antenna	topology	freq. (GHz)	gain (dBi)	reduction in freq. relative to basic patch (%)	change in gain relative to basic patch (dB)
basic patch (no slots)		2.58	6.5	-	-
		7.91	7.7	-	-
radiating-edge slot (RS)		2.16	2.6	16	-3.9
		3.77	4.9	52	-2.8
center slot (CS)		2.36	6.2	9	-0.3
		6.85	8.8	13	1.1
non-radiating-edge slot (NRS)		1.70	-0.2	34	-6.7
		3.56	-16.4	55	-24.1
radiating-edge slot spiraled (RSS)		2.16	-0.6	16	-7.1
		4.59	5.7	42	-2.0
RS + CS		2.09	2.6	19	-3.9
		3.48	1.6	56	-6.1
RS + NRS		1.42	-4.6	45	-11.1
		3.02	-3.0	62	-10.7
CS + NRS		1.57	-1.9	39	-8.4
		3.52	-13.0	56	-20.7
RS + CS + NRS		1.36	-5.2	47	-11.7
		2.88	-6.4	64	-14.1
RSS + CS + NRS		1.36	-6.0	47	-12.5
		1.74	-7.0	78	-14.7
		3.03	-8.6	77	-15.3
RSS + CS + NRS + offset feed		1.36	-5.9	47	-12.4
		1.74	-7.2	78	-13.7
		3.03	-8.0	77	-14.7
		2.38	-2.4	10	-8.7

of interest. The gain of the antenna is calculated from simulated data using the following modified Friis transmission formula for a lossy medium [87]:

$$\frac{P_R}{P_T} = G_T G_R \left( \frac{\lambda_{\text{eff}}}{4\pi R} e^{-\alpha R} \right)^2 (1 - |\Gamma_T|^2) (1 - |\Gamma_R|^2) \quad (4.1)$$

Here,  $P_T$ ,  $P_R$ ,  $G_T$ ,  $G_R$  are the transmitted and received powers and the gains of the respective antennas,  $R$  is the distance between antennas,  $\lambda_{\text{eff}} = \lambda = 2\pi/\text{Re}[k]$ , and  $\alpha = |\text{Im}[k]|$ , where  $k$  is the wave number of the lossy medium. The effect of impedance mismatch is taken into account by including the term  $(1 - |\Gamma_T|^2) (1 - |\Gamma_R|^2)$  in the above equation, where  $\Gamma$  is the reflection coefficient at the respective antenna. The gain of each antenna at the design frequency of interest was determined using a system of two identical miniaturized patch antennas immersed in the oil, separated by a distance of 15 cm. Because this spacing is rather small and the antennas radiate in a lossy environment, the calculated gain values reported in this work do not represent the traditional far-field gain of an antenna, which is reported when the antenna radiates in lossless environments and the observation point is well into the far-field.\* Nonetheless, the reported gain values can be used to compare the relative performance of different antenna types with each other (e.g. RS with RS + CS, etc.).

Table 4.1 shows miniaturization and gain reduction of the slot-loaded antennas compared to a basic patch. As expected, the table illustrates that slot-loading techniques miniaturize the patch antennas at the expense of gain. However, while different types of slots produce similar reductions in frequency, some affect the gain of the antenna more adversely than others. For example, loading the patch with either radiating-edge slots (RS) or non-radiating-edge slots (NRS) produces almost the same reduction in  $f_{300}$  (slightly over 50%). Using the latter ones, however, has a more significant effect in the reduction of gain at this frequency. RS designs (i.e. RS, RS + CS) produce a miniaturization of more than 50% at the resonant frequency of the  $\text{TM}_{300}$  mode with relatively good values of gain, 2-5 dBi. The center slot

---

\*The conventional definition of antenna gain is not valid for antennas that radiate in lossy environments [87].

(CS) only slightly reduces  $f_{100}$  and  $f_{300}$  with virtually no reduction in gain relative to the basic patch. Antennas loaded with a combination of slots (e.g. RS + CS, CS + NRS, RS + CS + NRS, and RSS + CS + NRS) produce the highest degree of miniaturization at both  $f_{100}$  and  $f_{300}$ . Again note, however, that gain at both  $f_{100}$  and  $f_{300}$  deteriorates significantly if the design incorporates NRS. The RSS + CS + NRS combination excites an additional mode, the  $TM_{500}$ , within the range of 0.5 - 3.5 GHz (as described in Section 4.3.1). Similar values of gain are obtained at the three desired frequencies of operation of this antenna. Moreover, off-setting the feed of this tri-band antenna excites an orthogonal resonant mode at 2.38 GHz with a gain of -2.4 dBi.

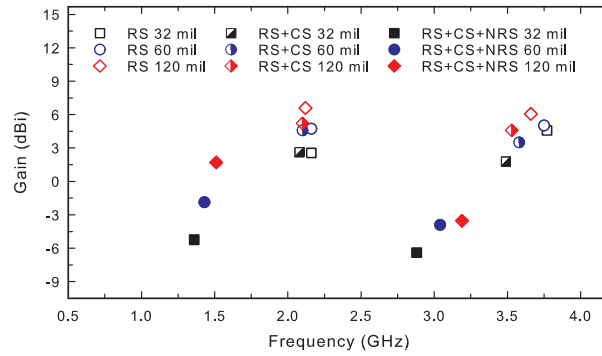
### 4.3.2.2 Effect of substrate parameters

We investigated the influence of substrate parameters, dielectric constant and thickness, on the resonant frequencies and gain of several slot-loaded patch antennas. The calculated gain of the RS, RS + CS, and RS + CS + NRS (i.e. dual-band miniaturized patch antenna) patch antennas versus frequency are shown in Figure 4.13. For this study we considered substrates with dielectric constants  $\epsilon_r = 3.55, 6.15,$  and  $10.2$  and thicknesses  $h = 32$  mil,  $60$  mil, and  $120$  mil. These are typical characteristics of substrate materials used in designing microstrip patch antennas.

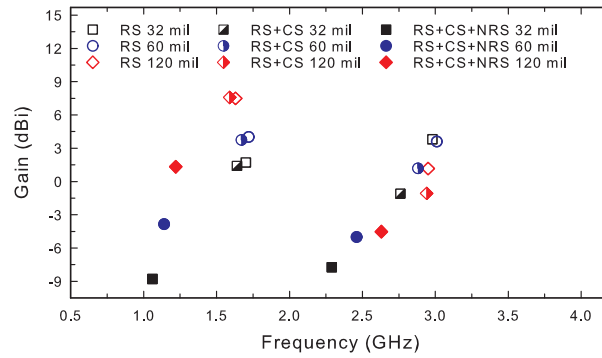
Figure 4.13 shows that the resonant frequencies of the  $TM_{100}$  and  $TM_{300}$  modes can be easily changed by changing these substrate characteristics. As expected, an increase in the dielectric constant of the antenna substrate corresponds to a decrease in the operating frequencies of the patch. In addition, an increase in the thickness of the substrate will improve the calculated gain at the frequencies of operation. The maximum calculated gain (similar values) is achieved for a substrate with  $\epsilon_r = 3.55$  and  $h = 120$  mil.

### 4.3.2.3 Measurement and experimental verification

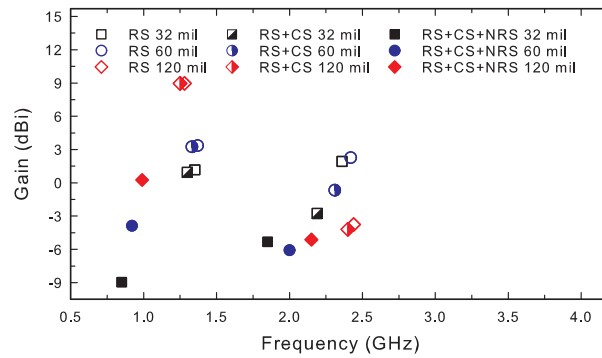
We experimentally validated miniaturized patch antenna designs presented in Table 4.1 that were loaded with a combination of slots, namely the RS + CS + NRS and the RSS +



(a)



(b)



(c)

Figure 4.13 Calculated gain versus frequency for different dielectric constants ( $\epsilon_r$ ) and thickness  $h$  of the substrate. (a)  $\epsilon_r = 3.55$ , (b)  $\epsilon_r = 6.15$ , (c)  $\epsilon_r = 10.2$ .

CS + NRS. These antenna designs correspond to the geometries shown in Figure 4.8(d) and Figure 4.9. The antenna elements were patterned on a  $10\text{ cm} \times 10\text{ cm} \times 0.08\text{ cm}$  RO4003 substrate and probe fed using the center conductor of an SMA connector. The fabricated antennas were immersed in a  $32\text{ cm} \times 15\text{ cm} \times 11\text{ cm}$  tank filled with safflower oil for all measurements described below.

The measured input reflection coefficients,  $S_{11}$ , of the multi-band miniaturized antennas are shown in Figs. 4.10-4.12. The fabricated tri-band antenna shows bands of operation at 1.36 GHz ( $TM_{100}$ ), 1.76 GHz ( $TM_{300}$ ), and 3.02 GHz, ( $TM_{500}$ ). The additional operating band of the quad-band miniaturized antenna is observed at 2.38 GHz ( $TM_{010}$ ). Excellent agreement is observed between the simulated and measured reflection coefficients for all of the multi-band antennas. This agreement provides an additional validation of the accuracy of the second-order dispersion fit of the dielectric properties of the safflower oil used in the numerical simulations of the antenna design. We note that the agreement between simulated and measured  $S_{11}$  curves for the dual-band antenna (Figure 4.10) is improved relative to that reported in [85]; that previous study used a less accurate dielectric property model for oil.

The depths of the  $S_{11}$  nulls for the  $TM_{100}$ ,  $TM_{300}$ , and  $TM_{500}$  modes of operation of the quad-band antenna (Figure 4.12) are not as deep as those of the tri-band antenna (Figure 4.11). This is attributed to the fact that the optimum feed location that results in the best impedance match is different for each mode. Thus, a compromise has to be made when using a single feed to impedance match a highly resonant structure at four different frequencies. Nonetheless, the measured  $S_{11}$  of this antenna is better than -8.6 dB for all frequencies of operation, which satisfies the requirements of our intended application.

Figure 4.14 shows the measured transmission coefficient of a system of two of the tri-band miniaturized patch antennas separated by a distance of 10 cm in the oil. The measurement of the transmission coefficient of a system of two dual-band miniaturized patch antennas was shown in Figure 4.3. As expected, the system has transmission peaks at the resonant frequencies of the first longitudinal modes. The measured transmission peak at  $f_{200}$  is very low (-60 dB), confirming that the radiation pattern has a broadside null at this frequency.



This second resonance is not useful for the intended application where a low-power microwave signal is transmitted. Here we also observe excellent agreement between simulation and experiment. We also measured the co- and cross-polarized radiation patterns of the multi-band miniaturized patch antennas immersed in oil. The measurements were taken at a distance of 15 cm from the patch. These antennas are designed to be used in an enclosed cubical array with side lengths on the order of 15 cm. Thus, the measurements were taken at a distance of 15 cm from the patch using half-wavelength dipoles.

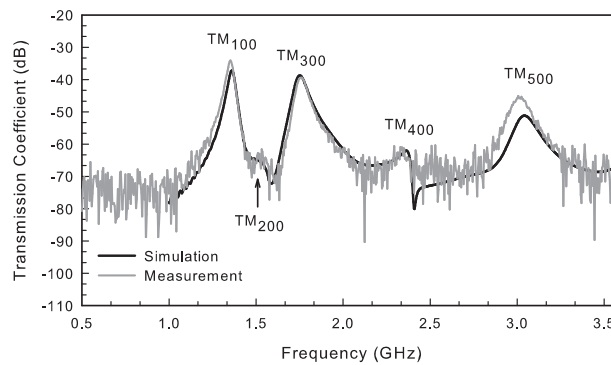


Figure 4.14 Simulated and measured transmission coefficients of a two-antenna system composed of the tri-band miniaturized patch antenna of Figure 4.9(b) immersed in safflower oil and separated by 10 cm.

Figures 4.15-4.16 show the co- and cross-polarized radiation patterns in the E- and H-planes at the frequencies of interest of the tri- and quad-band miniaturized antennas. The radiation patterns of the dual-band miniaturized antenna are shown in Figure 4.15. Each antenna shows consistent radiation patterns at its different bands of operation despite having different current distributions at each frequency. This is attributed to the manipulation of the current distribution of the higher-order resonant modes of the patch by strategically locating the loading slots. Moreover, most measured cross-pol levels are at least 15 dB lower than the co-pol ones at broadside for all frequencies of interest.

Figs. 4.15 and 4.16 show a good agreement between the co-pol components of the measured and the simulated radiation patterns of the two fabricated prototypes. The greater

discrepancy observed between the measured and the simulated cross-pol components is attributed to the fact that the very low cross-pol levels are more susceptible to measurement imperfections.

We also measured the gain of the multi-band miniaturized antennas immersed in oil. The gain of the antenna is calculated from measured or simulated data as described in Section 4.3.2.1. The simulated and measured gain values at the resonant frequencies of interest for the multi-band miniaturized antennas are listed in Table 4.2. We observe good agreement between the simulated and measured gain values.

Table 4.2 Calculated and measured values of multi-band miniaturized patch antennas discussed in Section 4.3.2.1. White:  $TM_{100}$ . Green:  $TM_{300}$ . Blue:  $TM_{500}$ . Red:  $TM_{010}$ .

type of antenna	freq. (GHz)	simulated gain (dBi)	measured gain (dBi)
dual-band	1.36	-5.3	-5.5
	2.88	-6.4	-5.9
tri-band	1.36	-6.0	-5.3
	1.74	-7.0	-7.6
	3.03	-8.6	-8.4
quad-band	1.36	-5.9	-5.3
	1.74	-7.2	-7.6
	3.03	-8.0	-7.7
	2.38	-2.4	-4.3

#### 4.3.2.4 Performance of the multi-band miniaturized patch antennas in microwave breast imaging

Another researcher in our group (M. J. Burfeindt) demonstrated the efficacy of using one of multi-band, miniaturized patch antennas reported here in an imaging array. The radiating-edge slot (RS) patch antenna was chosen to populate the array. The four array panels containing antennas have dimensions of  $L=124$  mm and  $W=164$  mm and are lined with a 60-mil-thick substrate with dielectric properties  $\epsilon_r=10.2$  and  $\tan \delta=0.0024$  S/m. The

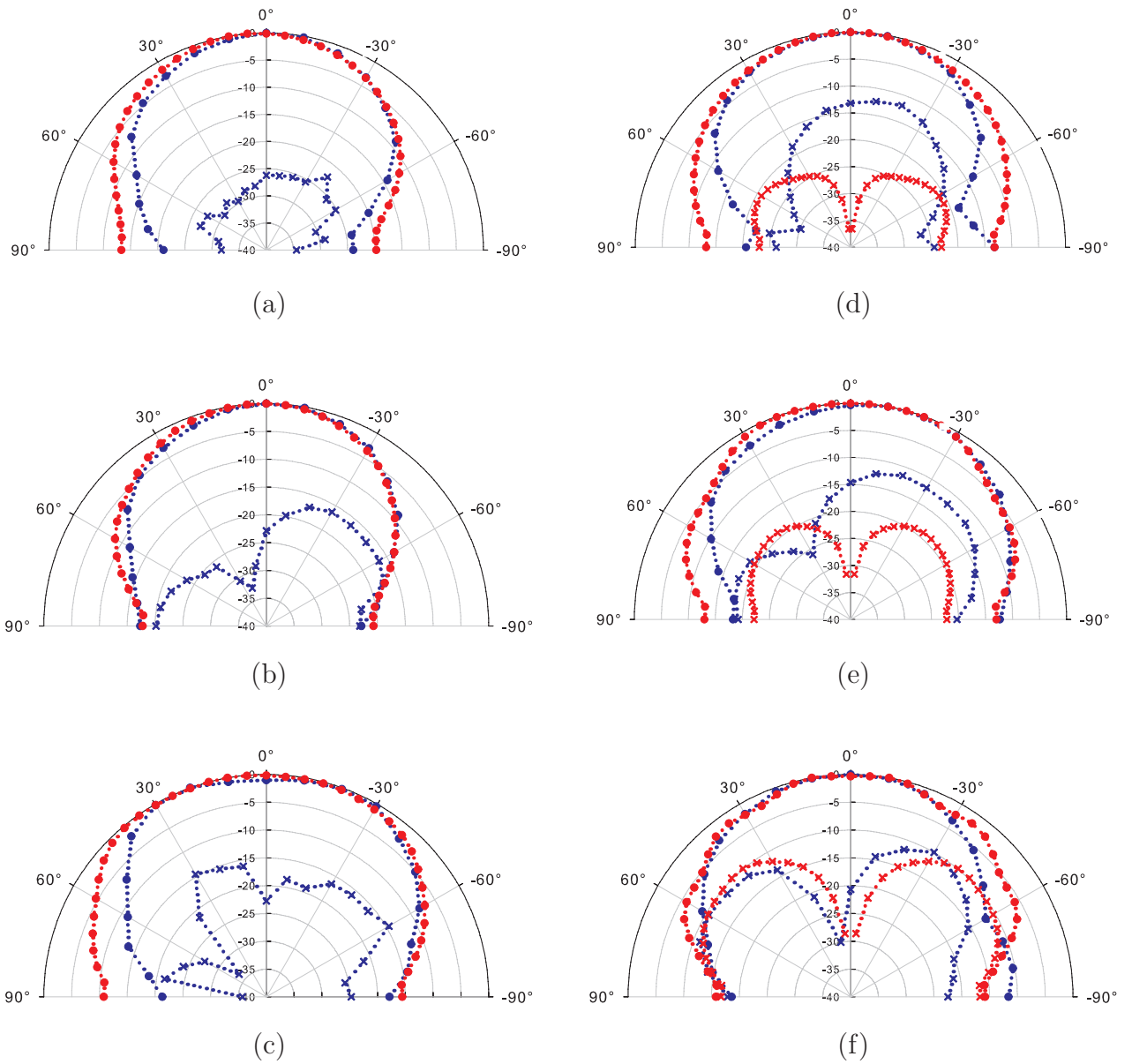


Figure 4.15 Simulated and measured radiation patterns of the tri-band miniaturized patch antenna in oil. The patterns are obtained at a distance of 15 cm from the patch. (a) E-plane at 1.36 GHz (b) 1.74 GHz and (c) 3.02 GHz. (d) H-plane at 1.36 GHz (e) 1.74 GHz and (f) 3.02 GHz. Solid red: simulated data. Dotted blue: measured data. Circle: co-pol. x: cross-pol.

hole in the top PEC array panel, through which the breast phantom descends, conforms to the ellipsoidal base of the phantom. The interior of the array is filled with an immersion material whose dielectric properties are described by a single pole Debye model with parameters  $\epsilon_\infty = 2.24$ ,  $\epsilon_s = 2.97$ , and  $\tau_p = 5$  ps.

The testbed consisted of the Class II (scattered fibroglandular) numerical breast phantom described in a previous imaging study [29]. Data acquisition was simulated using the finite-difference time-domain (FDTD) method. The dielectric profile of the breast is reconstructed using the technique described in [29]. FDTD was also used in the forward solver in the inverse scattering algorithm.

Visual agreement between the true phantom profile and the 3D reconstructed profiles is evident in the cross-sectional images of Figure 4.17. Cross-sections through the true profile are shown in Figure 4.17 (a)-(b). The reconstruction was performed using frequencies corresponding to the  $\text{TM}_{100}$  and  $\text{TM}_{300}$  modes of the RS patch antenna. Coronal and sagittal cross-sections through the 3D reconstruction are shown in Figure 4.17 (c)-(d). For comparison, cross-sections through a reconstruction created using the dipole array described in [29] are shown in Figure 4.17 (e)-(f). For the dipole reconstruction, the same frequencies were used in order to make a fair comparison. Both the patch and dipole reconstructions are successful in capturing the locations and basic shape of fibroglandular tissues in the phantom. The patch reconstruction is of similar fidelity to the true profile as compared to the dipole reconstruction. These results demonstrate the potential for using miniaturized, multi-band patch antennas for reconstructing the breast dielectric profile.

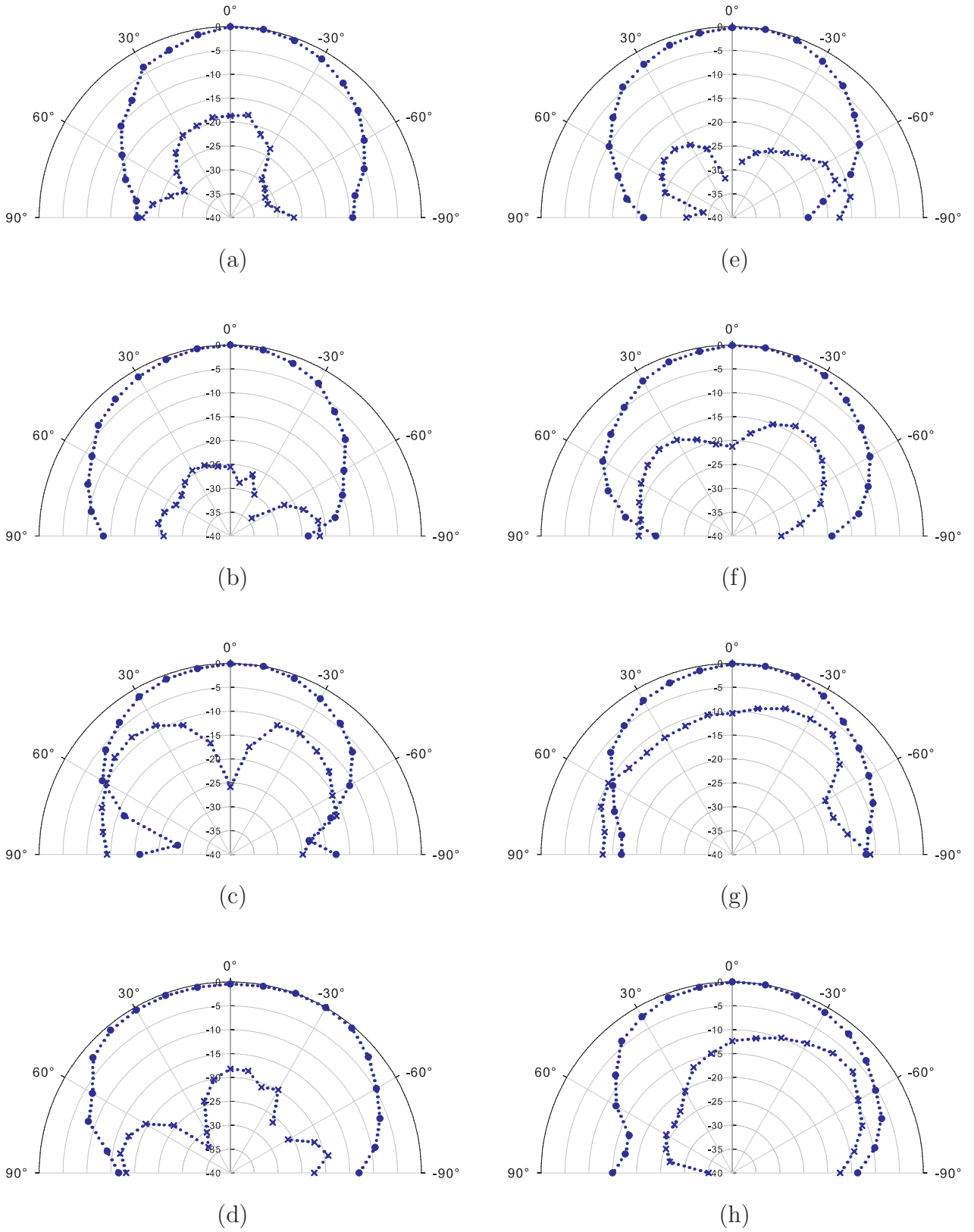


Figure 4.16 Simulated and measured radiation patterns of the quad-band miniaturized patch antenna in oil. The patterns are obtained at a distance of 15 cm from the patch. (a) E-plane at 1.36 GHz (b) 1.74 GHz (c) 2.38 GHz, and (d) 3.02 GHz. (e) H-plane at 1.36 GHz (f) 1.74 GHz (g) 2.38 GHz, and (h) 3.02 GHz. Solid red: simulated data. Dotted blue: measured data. Circle: co-pol. x: cross-pol.

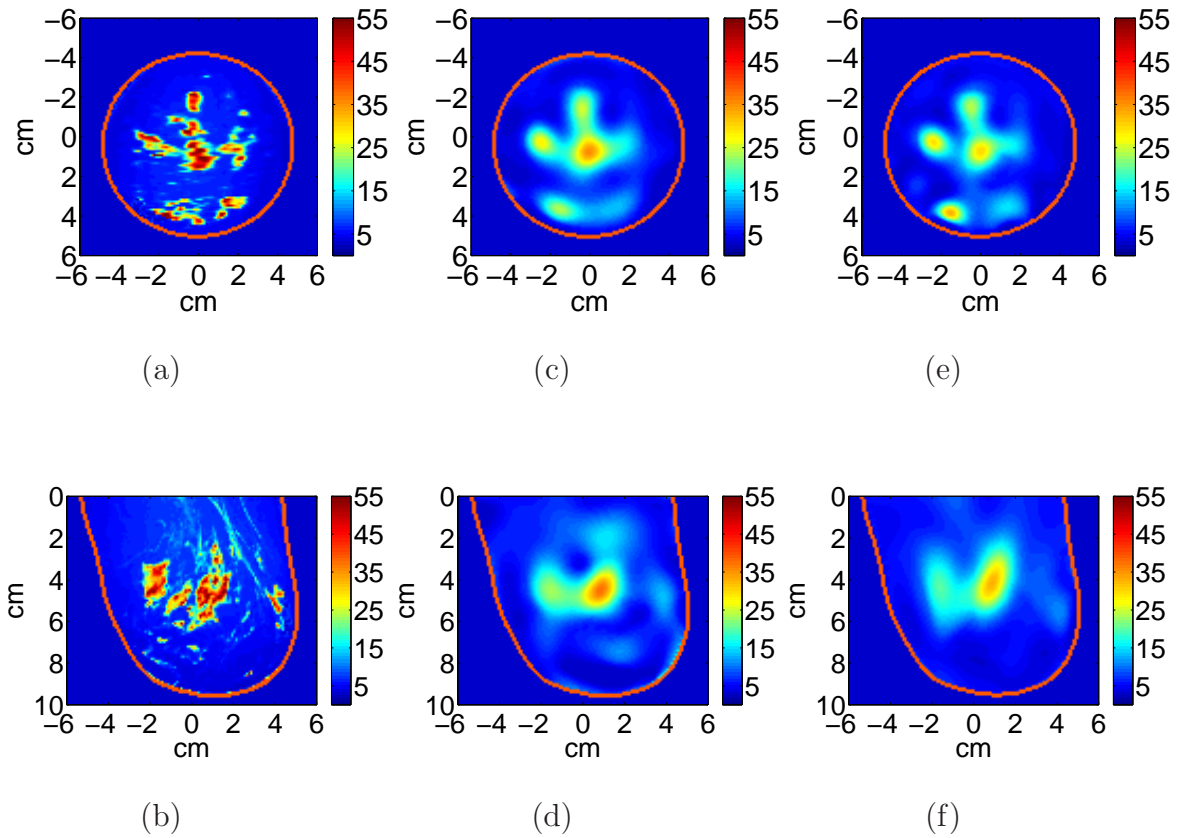


Figure 4.17 Comparison of imaging a Class II (scattered fibroglandular) breast phantom using two types of antenna arrays. Coronal (top row) and sagittal (bottom row) cross-sections of relative permittivity at 2.0 GHz. (a)-(b) True profile. (c)-(d) Images reconstructed using a multi-band miniaturized patch antenna array. (e)-(f) Images reconstructed using a dipole array.

#### 4.4 Effect of antenna pair separation distance on calculated gain

In Section 4.3.2.1, we mentioned that the calculated antenna gain values reported in this work do not represent the traditional far-field gain of the antenna for two reasons. First, the antennas are immersed in an oil medium, which is a lossy environment. Second, the calculated gain is obtained by using a system of two identical antennas separated by a distance of 15 cm, which is a rather small spacing. We adopted a modified form of the Friis transmission formula (equation (4.1)) to account for antenna radiation in oil. This transmission formula is well suited for antennas that radiate in a lossy medium [87]. In this section, we investigate the impact that having a distance of separation between antennas that is less than the traditional far-field one has on the calculated gain.

In its derivation, the Friis transmission equation (4.1) assumes far-field conditions between the transmitting and receiving antennas. The gain quantities in equation (4.1) are strictly far-field gains. If far-field conditions are not satisfied between the transmitting and the receiving antenna, near-field mutual coupling effects may play an important role. In such circumstances, the power transmission between the antennas is different from what would be predicted by (4.1) using far-field gains. One way to account for these effects is to use ‘near-field’ gains in the Friis transmission equation. Besides being different from the conventional far-field gain of an antenna, the ‘near-field’ gain, as will be observed later in this section, varies with the separation distance between the transmitting and the receiving antenna. The dependence of gain on antenna separation reduces as the distance is increased and far-field conditions are satisfied. The ‘near-field’ gain value then converges to the conventional far-field gain one.

The effects mentioned above can be observed by considering a half-wavelength dipole. An analytical model of a dipole has been used to accurately calculate the coupling between dipole antennas at any distance. This model is based on variational solutions of the self and mutual impedances of dipoles [88]. The self and mutual impedances are then converted into S-parameters using standard network theory techniques [89], which in turn are used

to calculate the modified gain of a half-wavelength dipole versus antenna separation using equation (4.1). Figure 4.18 shows that the computed gain of the half-wavelength dipole varies in an oscillatory fashion for antenna separation distances that are less than  $3\lambda$ . As the separation distance increases, the calculated gain then converges to the well-known dipole gain of 2.17 dBi.

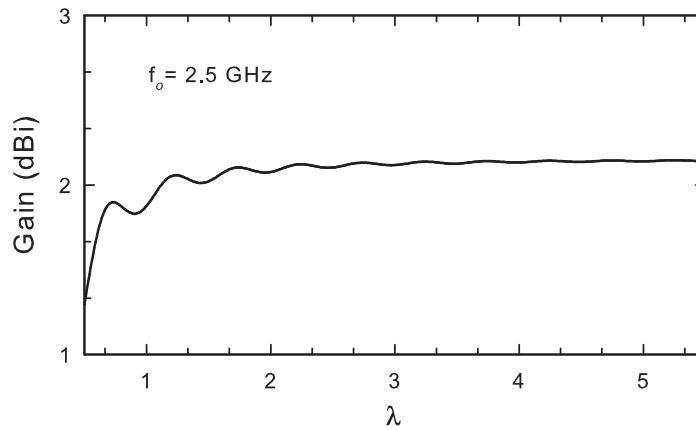


Figure 4.18 Calculated antenna gain versus the separation distance (as a function of  $\lambda$ ) between a pair of half-wavelength linear dipoles. Antenna gain obtained at the resonant frequency of the dipoles.

We studied the effects of antenna separation distances on the calculated gain at  $f_{100}$  and  $f_{300}$  of the different types of slot-loaded patch antennas shown in Table 4.1. In this study, we took into account guidelines set by [90] on the minimum distances, in  $\lambda$ , that facilitate measurements in the far-field of the antenna. These distances are based on the strictest of three conventional far-field criteria at each frequency of interest. These criteria suggest that the measurement distance be greater than the largest of  $2D^2/\lambda$  (the phase uncertainty limit),  $3D$  (the amplitude uncertainty limit), and  $3\lambda$  (the reactive near-field limit), where  $D$  is the largest dimension of the antenna and  $\lambda$  is the wavelength at the frequency of interest. The strictest criterion at  $f_{100}$  and  $f_{300}$  for most of the multi-band antennas considered in this study is the reactive near-field limit one ( $3\lambda$ ). The strictest criterion of the basic patch and CS patch at  $f_{300}$  is the phase uncertainty limit ( $2D^2/\lambda$ ).



Figure 4.19 shows the calculated antenna gain versus separation distance (as a function of  $\lambda$ ) between a pair of the slot-loaded, multi-band miniaturized patch antenna types immersed in safflower oil. Each data point represents the calculated gain value at separation distances of  $1\lambda$ ,  $2\lambda$ , and  $3\lambda$  for both frequencies of interest,  $f_{100}$  and  $f_{300}$ . The gain at the strictest criterion for  $f_{300}$  of the basic patch and CS patch are also shown. For comparison, the gain values calculated in Section 4.3.2.1 at a separation distance of 15 cm between the antennas are also presented. As in the case of the half-wavelength dipole (Figure 4.18), the results indicate that the calculated gain converges to a particular value as the distance of separation between the antennas increases. We can observe that the modified ‘near-field’ gain values obtained at 15 cm separation distance between the antennas using equation (4.1) are closely similar to those obtained at the conventional far-field strictest criterion of each antenna.

## 4.5 Summary

Slot-loaded, multi-band, miniaturized patch antennas for microwave breast imaging were designed, simulated, and tested. We investigated the gain at the operating frequencies of numerous slot-loaded miniaturized patch antennas patterned on different types of substrates. The study made it possible to understand the trade-off between miniaturization via slot-loading versus gain. The study also revealed that the gain of the miniaturized patch antennas can be modified by varying the antenna substrate dielectric constant and thickness.

Prototypes of several miniaturized patch antennas were fabricated and verified experimentally in a biocompatible immersion medium. The measured resonant frequencies of the modes of the patch antennas were in excellent agreement to the expected ones. Similar and symmetric radiation patterns at all bands of operation are obtained. The measured results of these fabricated prototypes indicate that these structure are suitable candidates as array element for multi-frequency microwave breast imaging systems.

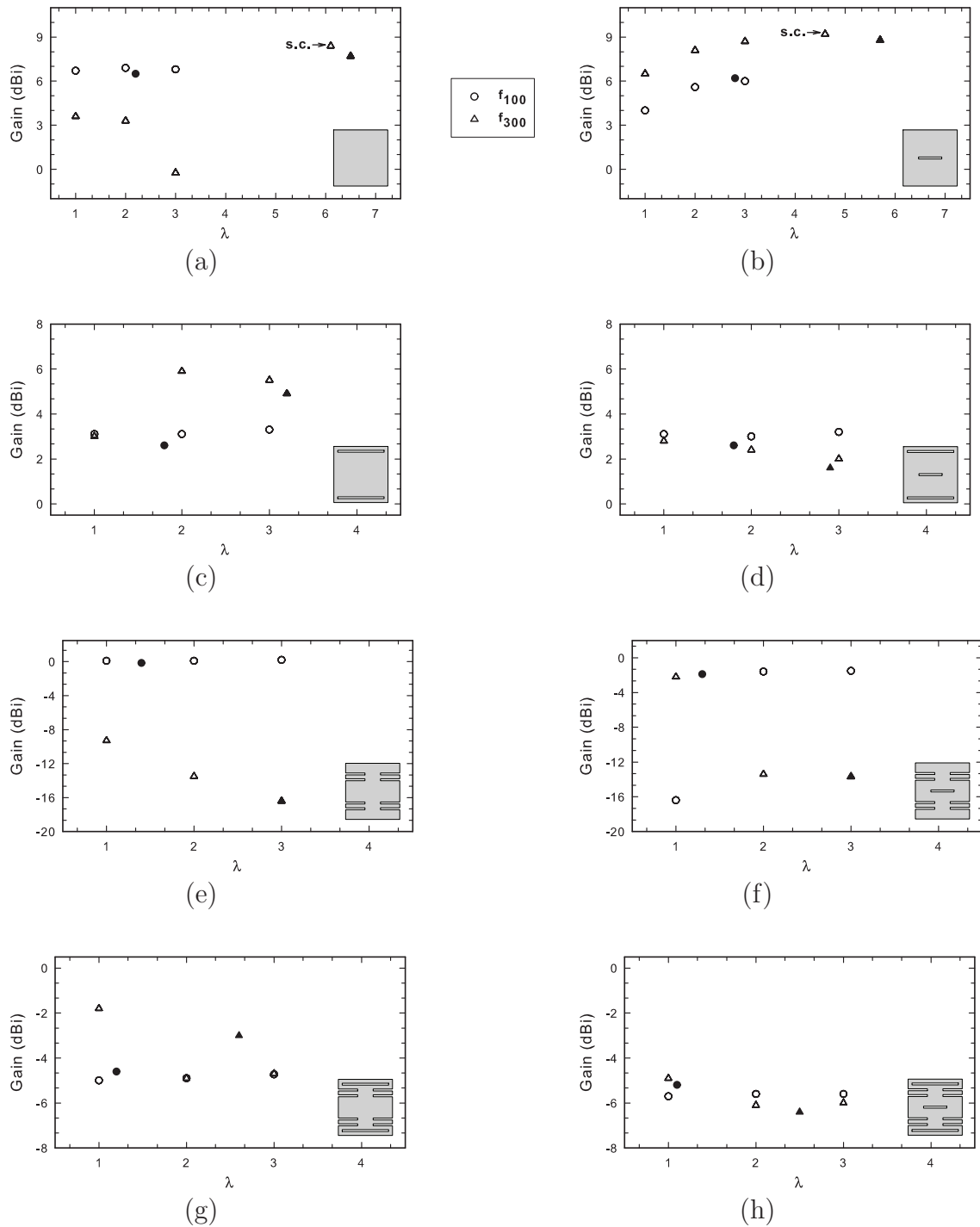


Figure 4.19 Calculated antenna gain versus the separation distance (as a function of  $\lambda$ ) between a pair of slot-loaded, multi-band miniaturized patch antenna types immersed in safflower oil. Antenna gain obtained at  $f_{100}$  and  $f_{300}$  for (a) basic patch (b) CS patch (c) RS patch (d) RS+CS patch (e) NRS patch (f) CS+NRS patch (g) RS+NRS patch (h) RS+CS+NRS patch. For all figures the separation distance at which the strictest criterion (s.c.) is satisfied occurs at  $3\lambda$ , except for (a) and (b), where the s.c. is noted. Solid circle and solid triangle: gain obtained using an antenna pair separated by 15 cm for  $f_{100}$  and  $f_{300}$ , respectively.

## Chapter 5

# Microwave breast imaging arrays comprised of multi-band miniaturized patch antennas

We present a compact multi-band patch antenna array designed for use in a 3D microwave tomography system for breast imaging. The array is designed for operation within the interstitial space of an MRI patient support platform. This configuration permits scattered-field data acquisition with the breast in the same position as a benchmark MRI scan, thereby enabling precise co-registration with breast MRI. We investigate operating characteristics, including mutual coupling, of the antenna array elements contained in the array using numerical simulations. We demonstrate that multi-band operation of the array is maintained in the presence of an ellipsoidal breast phantom.

### 5.1 Introduction

In this section, we present the design of a microwave antenna array that will enable an objective and precise comparison to be made between microwave and MR images of the breast. The coils of a breast MRI system will be removed from the patient support platform (see Figure 2.1) to create space for the microwave antenna array. This approach enables the microwave scan to take place with the patient on the MRI couch, but outside of the MRI bore. As previously mentioned, a thermoplastic mesh is used to maintain the position of the breast for both MRI and microwave scans [91].

We focus on maximizing the number of antenna elements contained in each panel to increase the spatial sampling of scattered signals. The maximum size of an array panel is constrained by the limited vertical extent available in the patient support platform.

Multi-band miniaturized patch antennas suitable for microwave breast imaging have been previously proposed [85,92]. These miniaturized patch antennas have a small footprint ( $\sim 30$  mm) and operate within the frequency range of 0.5 GHz to 3.5 GHz. Our proposed array is composed of these multi-band miniaturized patch antennas. One of the goals of this investigation is to assess the extent to which the operating characteristics of the individual antenna elements are altered in the presence of other antenna elements as well as the breast.

## 5.2 Array design\*

We populate the four side panels of the array with a maximum of 36 multi-band miniaturized patch antennas. Figure 5.1 shows the geometry of the proposed 3D sensor array. The antenna elements were patterned on a commercial substrate (Rogers Corp.) and are probe fed using the center conductor of an SMA connector. Each antenna panel measures  $13.7\text{ cm} \times 13.7\text{ cm}$  and is backed by a ground plane, which ensures unidirectional radiation into the imaging environment and provides isolation from external scatterers.

The top and bottom panels of the box contain metal planes that provide known boundary conditions at these locations of the imaging domain. The top metal plane includes an opening that allows the breast to be suspended in the imaging volume. The void between the array and the breast is filled with an oil immersion medium that provides an excellent impedance match with the tissue-stabilizing thermoplastic material, effectively making the thermoplastic invisible to the microwaves (see Chapter 3).

---

\*This section comprises content from the following conference proceeding: S. M. Aguilar, M. J. Burfeindt, M. A. Al-Joumayly, J. D. Shea, N. Behdad, and S. C. Hagness, "Design of a Microwave Breast Imaging Array Comprised of Dual-Band Miniaturized Antennas," presented at the URSI General Assembly and Scientific Symposium of International Union of Radio Science, Istanbul, Turkey, August 2011.

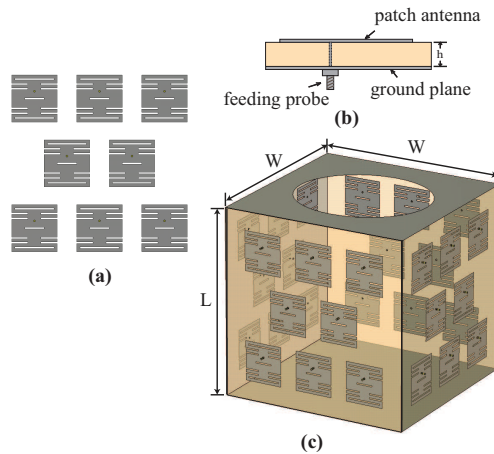


Figure 5.1 Microwave sensor array geometry. (a) Frontal view of one panel of the proposed array showing eight slot-loaded, miniaturized patch antennas. (b) Cross-sectional view of one slot-loaded, miniaturized patch antenna. (c) 3D view of the proposed sensor array, with side walls populated with patch antennas and top and bottom panels that contain metal planes. The top metal plane includes an opening that allows the breast to be suspended in the imaging volume.

### 5.3 Reduction of mutual coupling

Although the exact connection between mutual coupling and successful image reconstruction is not well understood, antenna coupling plays an important role in overall radiation and the input impedance of the antenna elements. Several researchers have proposed methods to minimize the mutual coupling between antenna elements of microwave imaging arrays [3, 38, 65]. Strong mutual coupling may reduce the measurement sensitivity of the system. Mainly, we want to maximize the number of antenna elements populating the array, while also minimizing the strong electromagnetic interaction between closely spaced elements.

The study described in Section 4.3.2.1 revealed that the radiating-edge slot (RS) patch antenna patterned on a 120-mil-thick Rogers RO4003 substrate ( $\epsilon_r = 3.55$ ) provided the best attainable gain at both  $f_{100}$  and  $f_{300}$ . The calculated gain values were 6.6 dB and 6.1 dB at 2.12 GHz ( $TM_{100}$ ) and 3.66 GHz ( $TM_{300}$ ), respectively (see Figure 4.13). We characterized

the mutual coupling between this type of RS patch antenna elements configured in an array panel.

The mutual coupling levels between adjacent RS patch antenna elements in the array were investigated using numerical simulations conducted with CST Microwave Studio. For our study, we considered the influence of substrate parameters (dielectric constant and thickness), variations of the geometrical structure of the substrate (e.g. metal walls or dielectric cuts), and different antenna element arrangements. To make a fair comparison, all patch antenna array elements patterned on a substrate panel are separated by a distance of 12 mm from each other. The substrate panels measure 13.7 cm  $\times$  13.7 cm and are immersed on the biocompatible immersion medium comprised of safflower oil.

Our first strategy was to vary substrate characteristics. We considered a panel arrangement that consisted of three rows of three antennas each (3 by 3) of RS patch antennas patterned on substrates of different dielectric constants  $\epsilon_r = 3.55$ , 6.15, and 10.2 and thicknesses  $h = 32$  mil, 60 mil, and 120 mil. Figures 5.2 - 5.4 show the coupling between different pairs of adjacent elements (horizontal, diagonal, vertical) in the array panel over the two frequency bands of interest,  $f_{100}$  and  $f_{300}$ . The results indicate that the level of mutual coupling between elements is a function of the substrate characteristics. A thicker substrate usually increases the gain of the antenna (as seen in Section 4.3.2.2). However, surface waves are easier to excite in an electrically thicker substrate and a substantial amount of power is coupled into the substrate. The results shown in Figures 5.2 - 5.4 reveal that using the thickest substrate (i.e. 120 mil) substantially increases the mutual coupling between antenna elements. The coupling increase can be as much as 13 dB at  $f_{100}$ . Figure 5.2 shows that adjacent elements on a substrate with the lowest dielectric constant considered in this study (i.e.  $\epsilon_r = 3.55$ ) exhibit the lowest levels of mutual coupling overall. However, the coupling between vertically adjacent elements is still significant. A 32-mil-thick,  $\epsilon_r = 3.55$  substrate provides the lowest mutual coupling ( $< -29$  dB) for all adjacent element pairs. For substrates with dielectric constants  $\epsilon_r = 6.15$  and 10.2, mutual coupling was more significant for horizontally adjacent antenna pairs, especially at  $f_{100}$ . The highest level of mutual coupling

observed was for a pair of horizontally adjacent antenna pairs patterned on a 120-mil-thick,  $\epsilon_r = 10.2$  substrate (-11 dB at  $f_{100}$ ).

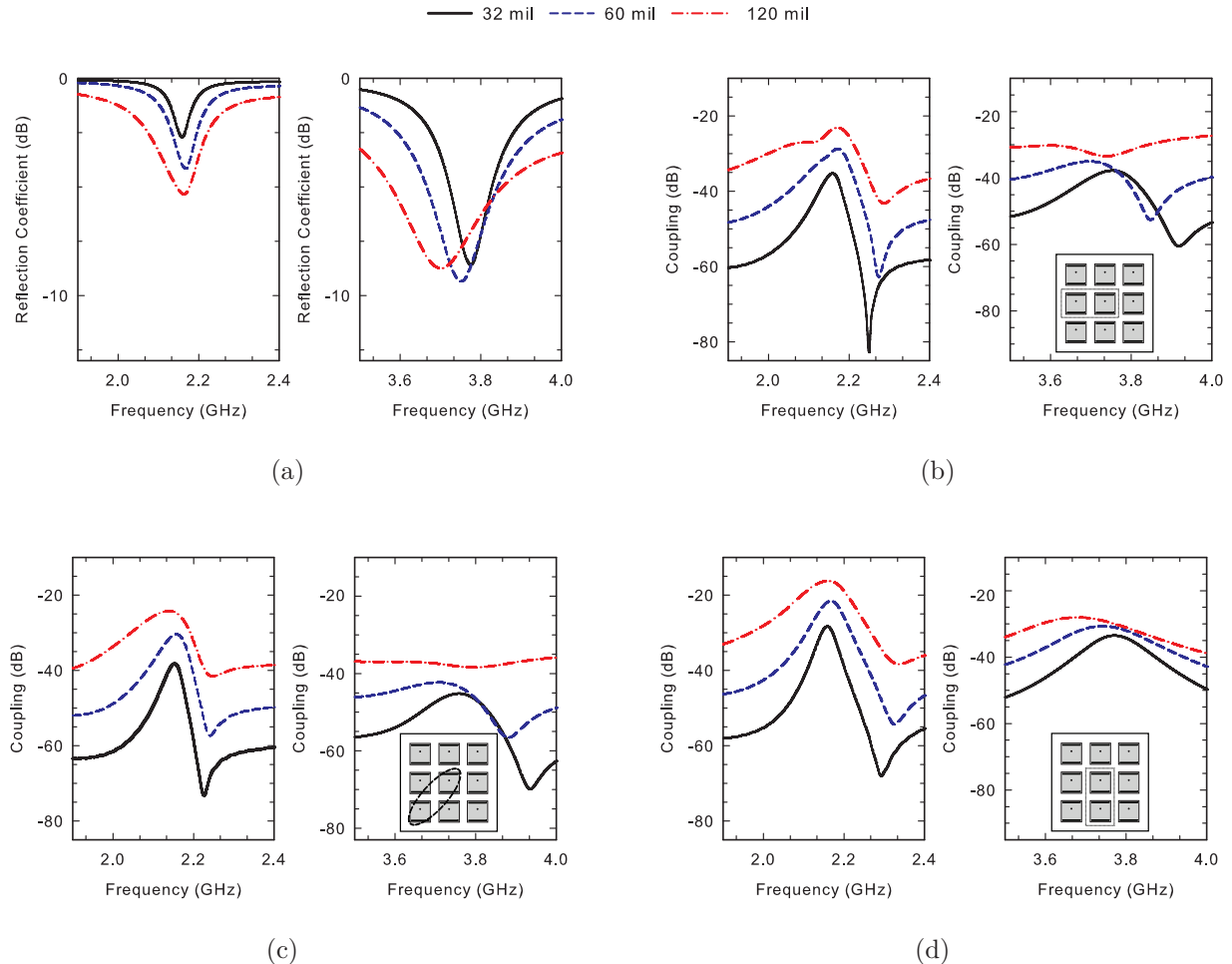


Figure 5.2 Simulated responses of RS patch antennas patterned on Rogers RO4003 substrate panels ( $\epsilon_r = 3.55$ ) of different thicknesses. (a) reflection coefficients ( $S_{11}$ ) (b)-(d) mutual coupling ( $S_{21}$ ) between pairs of (b) horizontally adjacent, (c) diagonally adjacent, and (d) vertically adjacent (boxed dashed lines). The left and right sub-plots show the 1st and 2nd frequency bands, respectively.

For the remaining two aspects of the study outlined in this section, we used a 32-mil-thick Rogers RO4003 ( $\epsilon_r = 3.55$ ) panel substrate populated by RS patch antennas.

First, we studied the effect of varying the antenna element arrangements on the array panel. We compared two alternate arrangements to the 3 by 3 arrangement (see top of Figure 5.5). The first one was an interleaved array configuration that contained antenna

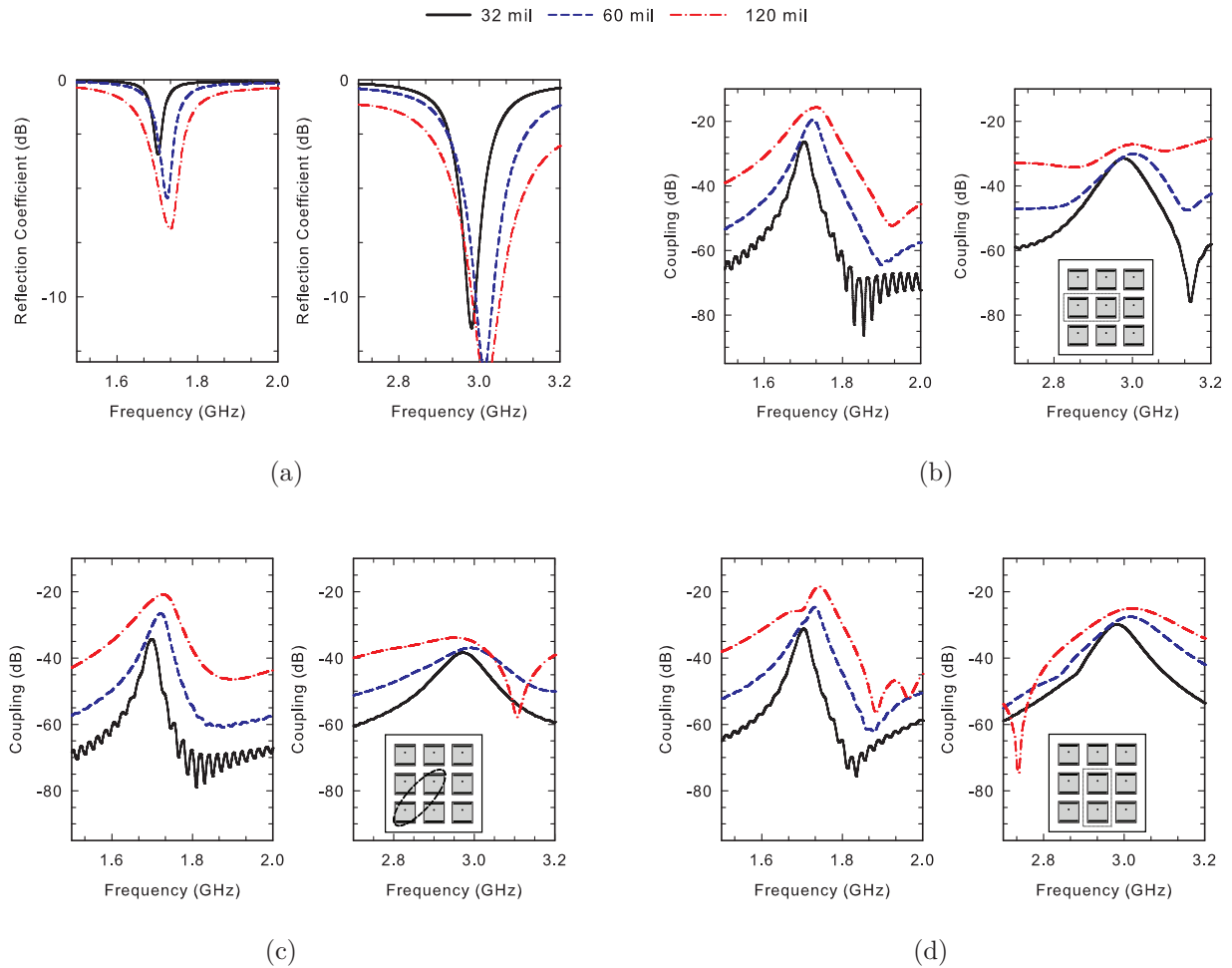


Figure 5.3 Simulated responses of RS patch antennas patterned on Rogers RO4360 substrate panels ( $\epsilon_r = 6.15$ ) of different thicknesses. (a) reflection coefficients ( $S_{11}$ ) (b)-(d) mutual coupling ( $S_{21}$ ) between pairs of (b) horizontally adjacent, (c) diagonally adjacent, and (d) vertically adjacent (boxed dashed lines). The left and right sub-plots show the 1st and 2nd frequency bands, respectively.

elements with two types of multi-band operation (i.e. the array consists of a group of antennas that operate at  $\{f_1, f_2\}$  and another group of antennas operating at  $\{f_3, f_4\}$ ). In this staggered-frequency arrangement,  $f_1=1.84$  GHz,  $f_2=3.07$  GHz,  $f_3=2.16$  GHz, and  $f_4=3.71$  GHz. Figure 5.5 shows the mutual coupling levels obtained between a center element and adjacent elements (horizontal, diagonal, vertical). We consider the coupling value between the adjacent elements at  $f_1$  and  $f_2$ . For the resonant frequency of  $TM_{100}$ , the total reduction for horizontally adjacent pairs is of around 5.4 dB. Coupling reduction for diagonally and



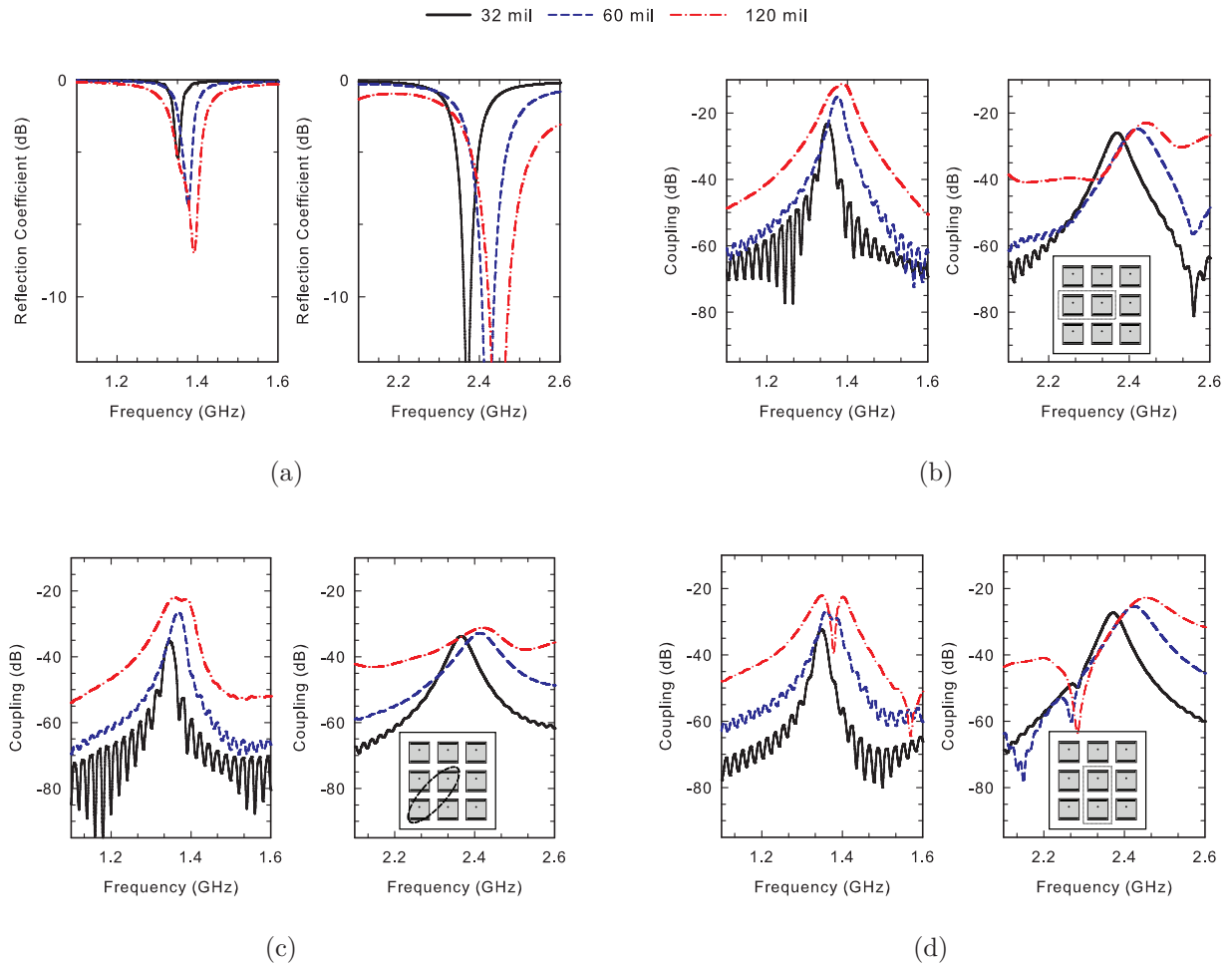


Figure 5.4 Simulated responses of RS patch antennas patterned on Rogers RO3010 substrate panels ( $\epsilon_r = 10.2$ ) of different thicknesses. (a) reflection coefficients ( $S_{11}$ ) (b)-(d) mutual coupling ( $S_{21}$ ) between pairs of (b) horizontally adjacent, (c) diagonally adjacent, and (d) vertically adjacent (boxed dashed lines). The left and right sub-plots show the 1st and 2nd frequency bands, respectively.

vertically adjacent antenna pairs is also observed. We also considered a staggered-element arrangement of RS patch antennas that operate at the same frequencies of interest. This element arrangement reduces the total number of antenna elements on the panel to eight. This staggered topology provides a coupling reduction for some diagonally adjacent pairs, mainly between the center element and the top or bottom element closer to the edge of the substrate. The change in mutual coupling for pairs of antennas adjacent to each other in the

staggered-frequency (arrangement 2) and the staggered-element (arrangement 3) element arrangement relative to a 3 by 3 (arrangement 1) is shown in Figure 5.6. The change in mutual coupling between pairs of antennas adjacent to the center element of the panel are shown. The results show that the staggered-element provides more mutual coupling reduction at the resonant frequency of  $TM_{100}$ . The staggered-frequency provides more mutual coupling reduction at the resonant frequency of  $TM_{300}$ .

Finally, we considered geometrical variations of the array panel substrate, including metal walls [93], trenches or cuts on the substrate [93], and a realization of artificially soft-surface structures that have been previously proposed in [94]. These methods are well-suited for the suppression of surface waves [93, 95]. The propagation of surface waves causes undesirable coupling between the antenna elements.

Figure 5.7 (top, from left to right) illustrates a basic substrate panel with no geometry variation, a substrate panel with 4-mm-thick metal walls in between antenna elements, a substrate panel with 4-mm-thick dielectric cuts around antenna elements, and the proposed soft-surface structures. The soft-surface structures consist of a number of metal strips that are close to a quarter-wavelength wide at  $TM_{100}$  and that are short-circuited to the ground plane [95]. It has been demonstrated that the operating frequency for this soft-surface is determined by the strip width [93]. A single square ring of the shorted quarter-wavelength metal strips is employed to form a soft-surface and to surround the patch antenna for the suppression of outward propagating surface waves [95].

The response of antennas patterned on the substrates with different geometrical variations is shown in Figure 5.7. The reflection coefficient of the center element reveals a slight shift in the center frequencies of operation of the antennas patterned on substrates that incorporate metal walls and the soft-surface. Coupling coefficients between different pairs of adjacent antenna are also shown. Overall, the cuts on the dielectric substrate did not provide any reduction in the mutual coupling between antenna elements. Additional simulations of substrates with different dielectric constants,  $\epsilon_r = 6.15$  and  $10.2$ , revealed the same trend. The mutual coupling reduction obtained with the substrates using the metal walls and the

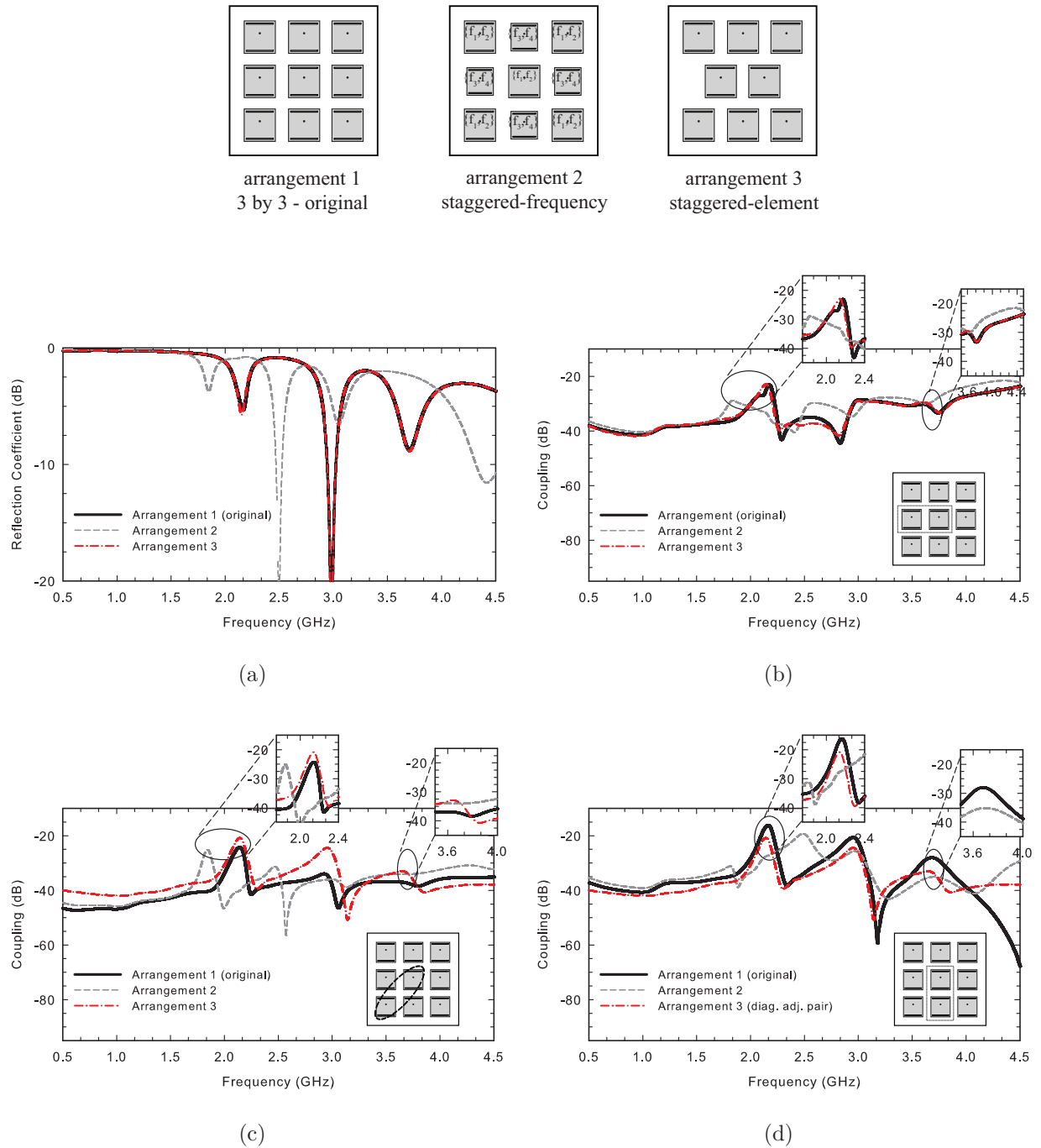
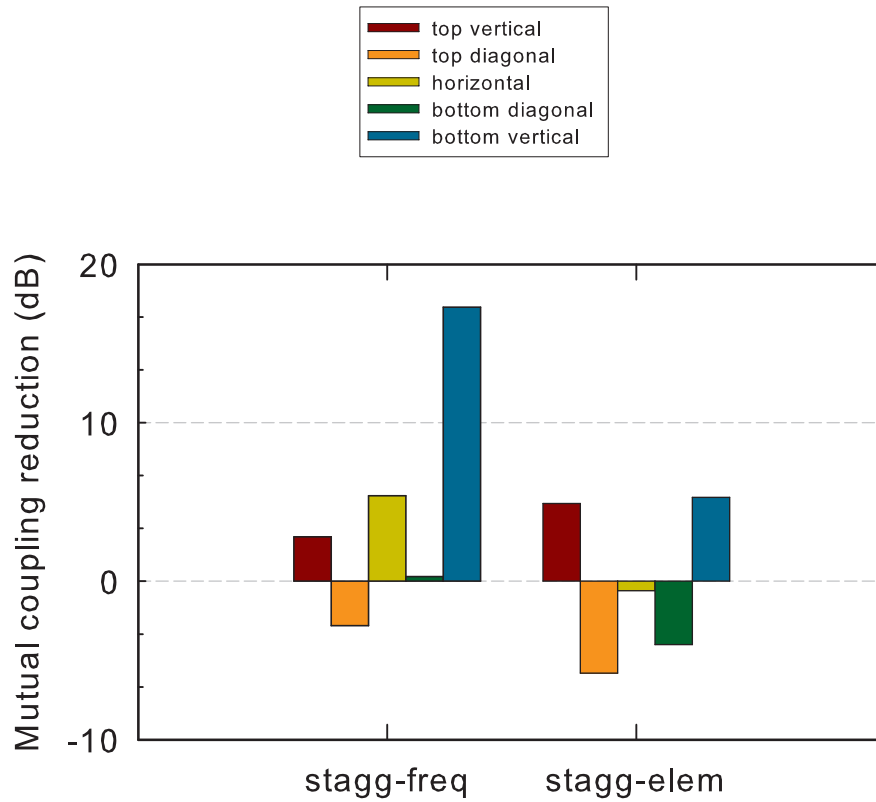
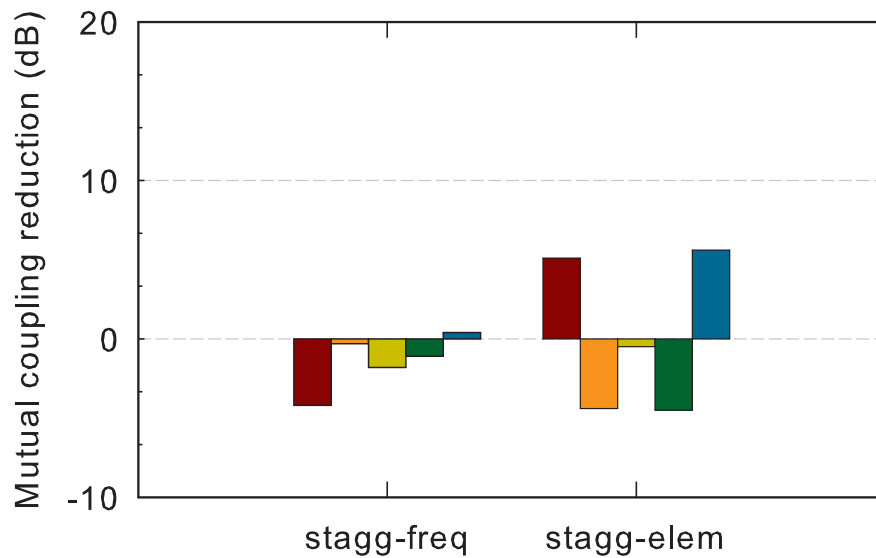


Figure 5.5 Simulated responses of RS patch antennas for different element arrangements in an array panel: 3 by 3 (arrangement 1), staggered-frequency (arrangement 2), and staggered-element (arrangement 3). (a) reflection coefficients ( $S_{11}$ ) of a central element (b)-(d) mutual coupling ( $S_{21}$ ) between pairs of (b) horizontally adjacent, (c) diagonally bottom adjacent, and (d) vertically bottom adjacent (boxed dashed lines). The left and right sub-plots show the 1st and 2nd frequency bands, respectively.



(a)



(b)

Figure 5.6 Change in mutual coupling for pairs of adjacent antennas in the staggered-frequency (arrangement 2) and the staggered-element (arrangement 3) element arrangement relative to a 3 by 3 (arrangement 1) (shown in Figure 5.5). Change in mutual coupling ( $S_{21}$ ) between pairs of antennas adjacent to the center element of the panel are shown. The results are shown for the resonant frequency of (a)  $TM_{100}$  and (b)  $TM_{300}$  of the RS patch antenna.

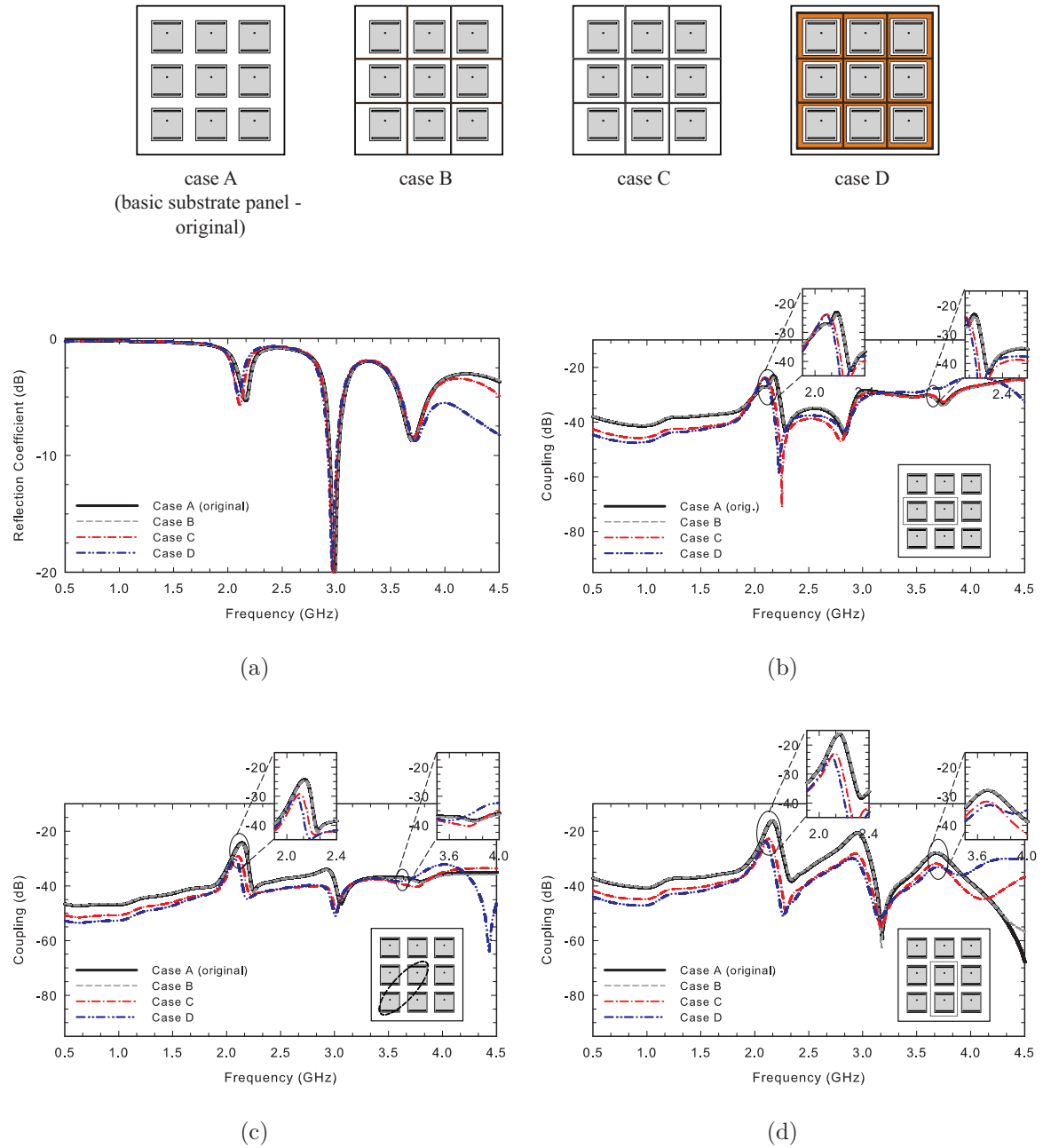
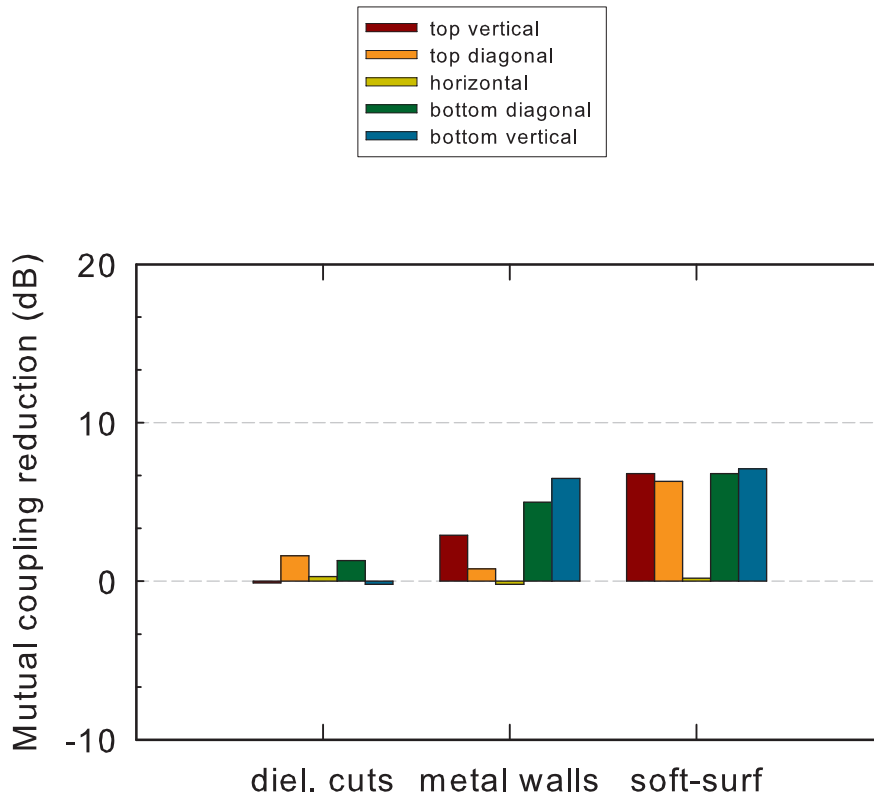
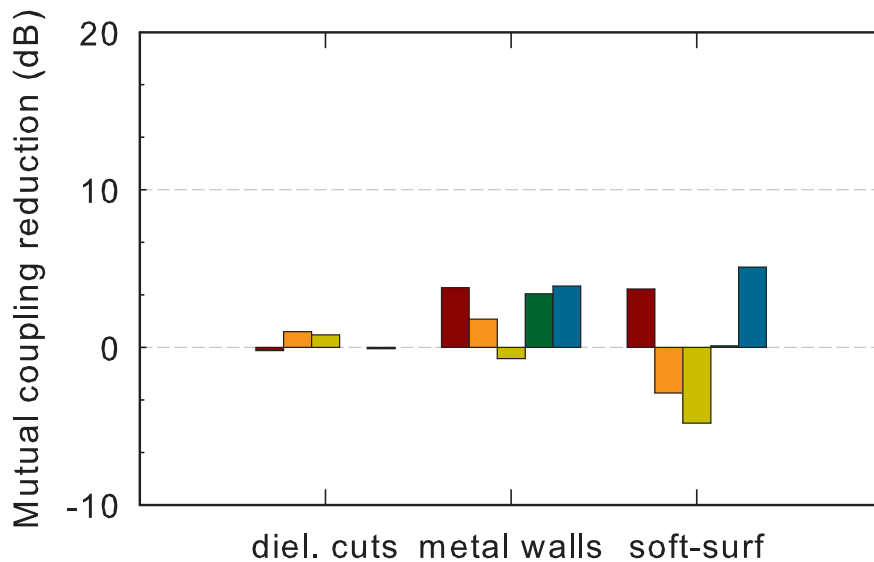


Figure 5.7 Simulated responses of RS patch antennas on different geometrical variations of the array panel substrate: basic substrate panel (case A), metal walls (case B), trenches on substrate (case C), and soft-surface substrate (case D). (a) reflection coefficients ( $S_{11}$ ) (b)-(d) mutual coupling ( $S_{21}$ ) between pairs of (b) horizontally adjacent, (c) diagonally adjacent (d) vertically adjacent. The left and right sub-plots show the 1st and 2nd frequency bands, respectively.



(a)



(b)

Figure 5.8 Change in mutual coupling for pairs of adjacent antennas in the metal walls (case B), trenches on substrate (case C), and soft-surface substrate (case D) geometrical variations on the panel substrate relative the basic substrate panel (case A) (shown in Figure 5.7). Change in mutual coupling ( $S_{21}$ ) between pairs of antennas adjacent to the center element of the panel are shown. The results are shown for the resonant frequency of (a)  $TM_{100}$  and (b)  $TM_{300}$  of the RS patch antenna.

soft-surface structures is very similar when compared at the respective operation frequencies of the antennas in the two cases. Figure 5.8 presents the change in mutual coupling for the metal walls (case B), trenches on substrate (case C), and soft-surface substrate (case D) geometrical variations on the panel substrate relative the basic substrate panel (case A). The change in mutual coupling between pairs of antennas adjacent to the center element of the panel shown. The results show that the soft-surfaces provide more mutual coupling reduction overall.

Finally, we compared coupling between pairs of antennas of a 3 by 3 arrangement and the staggered-element arrangement. We first obtain the coupling for antennas patterned on a basic substrate panel. We compare these results with antennas patterned on a substrate using soft-surface structures. Figure 5.9 reveals that when using a combination of the staggered-element arrangement on a substrate panel using soft-surface structures, the mutual coupling for vertically and diagonally adjacent pairs is significantly reduced. A slight increase in the coupling level of horizontally adjacent pairs of around 3 dB at  $f_{300}$  is observed when soft-surface structures are used. However, if we compare the vertically adjacent antenna pairs of the 3 by 3 arrangement without soft-surfaces to the diagonally adjacent pairs of the staggered-arrangement with soft-surfaces, the reduction obtained is of 12 dB at  $f_{100}$  and 6 dB at  $f_{300}$ . This represents the maximum reduction obtained for the arrangements and variations of substrate geometry considered in this study.

We also investigated mutual coupling levels in a array panel composed of an RS+CS+NRS antenna (i.e. dual-band miniaturized patch antenna presented in [85]). The panel arrangement consisted of three rows of three antennas each (3 by 3) (top left of Figure 5.10). The antennas are patterned on a 32-mil-thick RO4003 substrate ( $\epsilon_r = 3.55$ ). Simulations of transmission coefficients between pairs of antennas located in the same panel revealed that vertically adjacent elements (boxed by dashed lines) exhibit a high level of mutual coupling.

We then considered the staggered-element arrangement (top right of Figure 5.10). Figure 5.10 shows the coupling between vertically adjacent antenna elements of the two panel

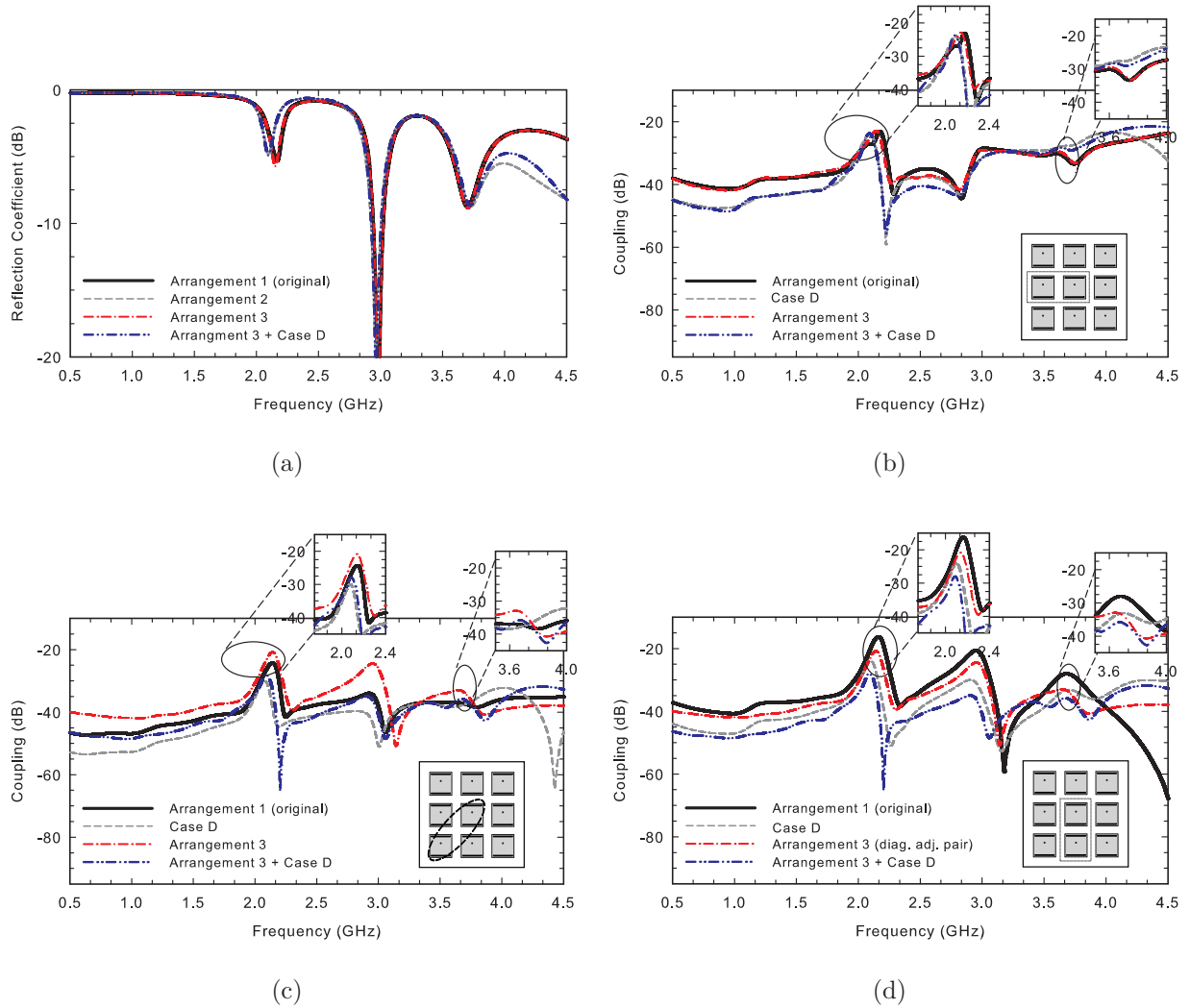


Figure 5.9 Simulated responses of RS patch antennas on different array panel arrangements, 3 by 3 on a basic substrate panel (arrangement 1), staggered-element on a basic panel substrate (arrangement 2), 3 by 3 on a soft-surface structure substrate (arrangement 3), and staggered-element on a soft-surface structure substrate (arrangement 3 + case D). (a) reflection coefficients ( $S_{11}$ ) (b)-(d) mutual coupling ( $S_{21}$ ) between pairs of (b) horizontally adjacent, (c) diagonally adjacent, and (d) vertically adjacent (boxed dashed lines). The left and right sub-plots show the 1st and 2nd frequency bands, respectively.



arrangements. We observed that due to the change in configuration the mutual coupling between vertical antenna element pairs is reduced by around 5.5 dB at both  $f_{100}$  and  $f_{300}$ .

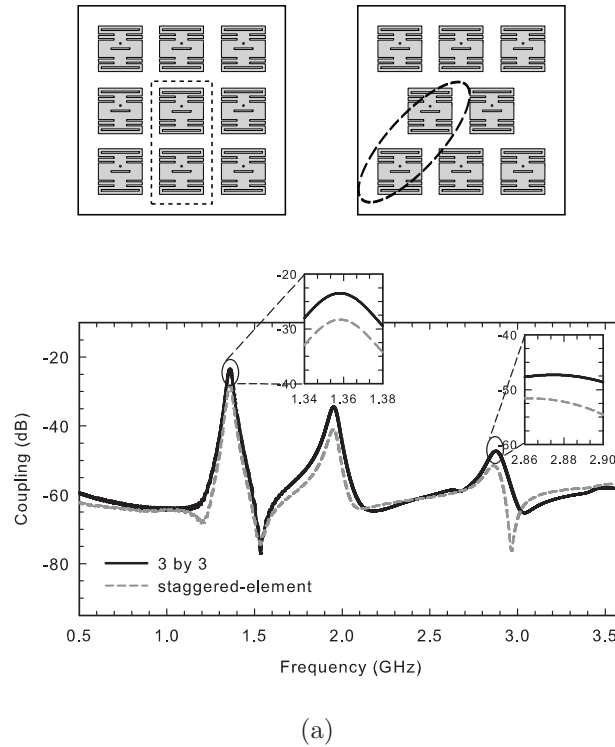


Figure 5.10 Comparison of the simulated mutual coupling  $S_{21}$  between a pair of dual-band miniaturized antennas that are vertically adjacent (3 by 3, top left) and diagonally adjacent (staggered-element, top right) (boxed dashed lines). The antennas are patterned on a 32-mil-thick Rogers RO4003 substrate panel ( $\epsilon_r = 3.55$ ).

## 5.4 Results

### 5.4.1 Antenna element in array panel \*

We investigated the extent to which the measured operating characteristics of the individual antenna elements are altered in the presence of other antenna elements [96]. We

---

\*This section comprises content from the following conference proceeding: S. M. Aguilar, M. A. Al-Joumayly, S. C. Hagness, and N. Behdad, “Design of a Miniaturized Dual-Band Patch Antenna as an Array Element for Microwave Breast Imaging,” presented at the IEEE AP-S International Symposium and USNC/URSI Radio Science Meeting, Toronto, Canada, July 2010.

fabricated prototypes of dual-band miniaturized patch antenna elements (array panels with 9 elements in each panel (Figure 5.11). The antenna elements were patterned on a 32-mil-thick RO4003 substrate ( $\epsilon_r = 3.55$ ). The antenna element of interest is probe-fed using a center conductor of an SMA connector.

We measured the reflection coefficients of both the isolated elements and the central antenna elements contained in the array panel. We immersed the fabricated antenna(s) in a 32 cm  $\times$  15 cm  $\times$  11 cm tank filled with safflower oil. The magnitude of the measured  $S_{11}$  frequency response of the antenna is shown in Figure 5.12. Excellent agreement is observed between the simulated and measured reflection coefficients. Both the fabricated isolated antenna and the central antenna in the array panel show multiple bands at 1.34 GHz, 1.93 GHz, and 2.87 GHz.

Figure 5.13 shows the measured transmission coefficient of a system of two miniaturized patch antennas (either two isolated antennas or the central antennas in two array panels) separated by a distance of 10 cm in the oil. As expected, the system has transmission peaks at  $f_{100}$  and  $f_{300}$ . The transmission peak at  $f_{200}$  is very low ( $-60$  dB), confirming that the radiation pattern has a broadside null at this frequency. This second resonance is not expected to be useful for the intended application where a low-power microwave signal is transmitted. Here we also observe excellent agreement between simulation and experiment. The measured reflection and transmission data of the antenna in the array reveal that there is no frequency shift of the desired dual-band operation of the antenna when used as part of an array.

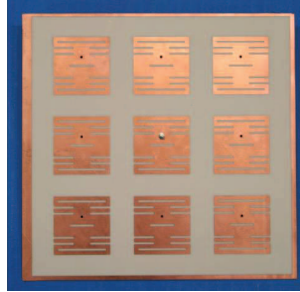


Figure 5.11 Photograph of the fabricated dual-band miniaturized patch antenna in an array.

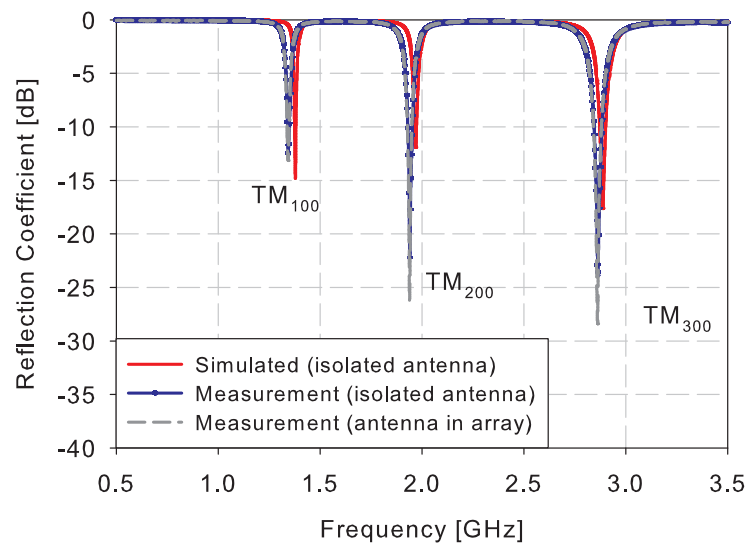


Figure 5.12 Simulated and measured reflection coefficients of an isolated dual-band miniaturized patch antenna immersed in safflower oil. Measured data for an antenna in an array is also shown.

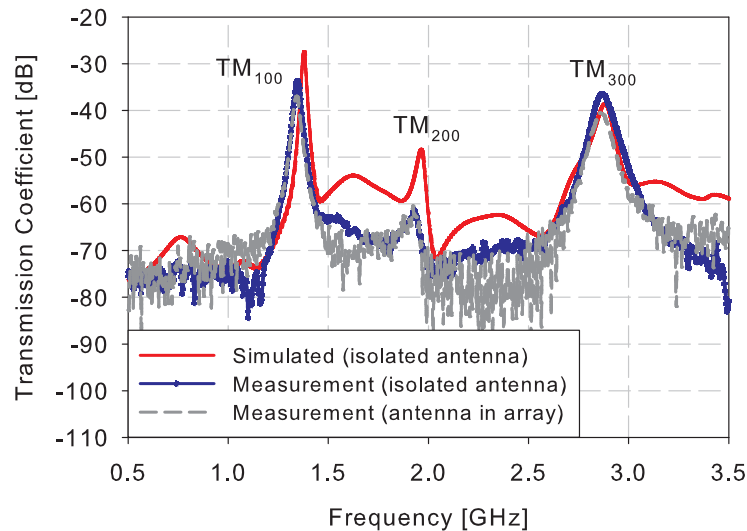


Figure 5.13 Simulated and measured transmission coefficients of an antenna system composed of two dual-band miniaturized antennas. The two patch antennas are immersed in safflower oil and separated by 10 cm. Measured data for antenna array elements is also shown.

## 5.4.2 Antenna elements in 3D sensor array

### 5.4.2.1 Array composed of dual-band miniaturized patch antennas\*

For this study, we populate the four side panels of the array with 32 dual-band miniaturized patch antennas described in [85]. One of the goals of this investigation is to assess the extent to which the operating characteristics of the individual antenna elements are altered in the presence of the breast.

We observed in Section 5.3 that in a 3 by 3 substrate panel, pairs of dual-band miniaturized antennas located in the same panel exhibit a high level of mutual coupling, particularly

---

\*This section comprises content from the following conference proceeding: S. M. Aguilar, M. J. Burfeindt, M. A. Al-Joumayly, J. D. Shea, N. Behdad, and S. C. Hagness, "Design of a Microwave Breast Imaging Array Comprised of Dual-Band Miniaturized Antennas," presented at the URSI General Assembly and Scientific Symposium of International Union of Radio Science, Istanbul, Turkey, August 2011.

the vertically adjacent antenna pairs (see Figure 5.10). Consequently, for this study we used the staggered-element arrangement. Figure 5.14 illustrates the proposed arrangement of eight elements on each panel forming a 32-element array. The antenna array panels are patterned on 32-mil-thick RO4003 substrates ( $\epsilon_r = 3.55$ ). The patch antennas are probe-fed using the center conductor of an SMA connector.

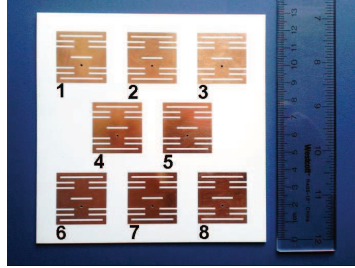


Figure 5.14 Photograph of a prototype of one 13 cm  $\times$  13 cm panel of the proposed array showing eight dual-band miniaturized (28 mm  $\times$  29 mm) antennas.

An ellipsoidal breast phantom is introduced to the simulation domain as shown in Figure 5.15[(b)-(d)]. The pendant breast phantom is an 11.4 cm long ellipsoid with a 10 cm diameter circular base. The interior of the phantom is composed of (b) fatty tissue (c) glandular tissue, and (d) fatty tissue with a 5 cm diameter sphere of glandular tissue; the surface of the phantom includes a 2-mm-thick skin layer. For model completeness, the base of the breast also includes a 1.5-cm-thick subcutaneous fat layer and a 0.5-cm-thick muscle chest wall. The dispersive dielectric properties of breast fat, glandular tissue, skin, and muscle are based on properties described in [36] and [97]. In the numerical simulations, the superposition of two first order dispersion models based on general polynomial formulations [86] were employed to curve-fit to the data reported in [36] and [97]. The superposition of these two first order models can be expressed as:

$$\epsilon_r(\omega) = \epsilon_\infty + \frac{\beta_{0,0}}{\alpha_{0,0} + j\omega} + \frac{\beta_{0,1}}{\alpha_{0,1} + j\omega}. \quad (5.1)$$

The fit was performed to data over the frequency range of 0.5-5 GHz. The resulting first order dispersion model parameters are as follows:

- for fatty tissue,  $\epsilon_\infty = 1$ ,  $\alpha_{0,0} = 154.19 \times 10^9 \text{ s}^{-1}$ ,  $\beta_{0,0} = 0.58 \times 10^{12} \text{ s}^{-1}$ ,  $\alpha_{0,1} = 0.36 \times 10^9 \text{ s}^{-1}$ ,  $\beta_{0,1} = 4.19 \times 10^9 \text{ s}^{-1}$ ;
- for muscle tissue,  $\epsilon_\infty = 1$ ,  $\alpha_{0,0} = 117.49 \times 10^9 \text{ s}^{-1}$ ,  $\beta_{0,0} = 6.17 \times 10^{12} \text{ s}^{-1}$ ,  $\alpha_{0,1} = 0.44 \times 10^9 \text{ s}^{-1}$ ,  $\beta_{0,1} = 92.14 \times 10^9 \text{ s}^{-1}$ ;
- for glandular tissue,  $\epsilon_\infty = 1$ ,  $\alpha_{0,0} = 103.76 \times 10^9 \text{ s}^{-1}$ ,  $\beta_{0,0} = 4.93 \times 10^{12} \text{ s}^{-1}$ ,  $\alpha_{0,1} = 0.13 \times 10^9 \text{ s}^{-1}$ ,  $\beta_{0,1} = 81.67 \times 10^9 \text{ s}^{-1}$  and;
- for skin,  $\epsilon_\infty = 1$ ,  $\alpha_{0,0} = 113.05 \times 10^9 \text{ s}^{-1}$ ,  $\beta_{0,0} = 4.23 \times 10^{12} \text{ s}^{-1}$ ,  $\alpha_{0,1} = 0.98 \times 10^9 \text{ s}^{-1}$ ,  $\beta_{0,1} = 89.03 \times 10^9 \text{ s}^{-1}$ .

We investigated the theoretical performance of the array using numerical simulations conducted with CST Microwave Studio. Here, we highlight the reflection coefficients of individual antenna elements. The magnitude of the simulated reflection coefficient of several miniaturized patch antennas are shown in Figure 5.16. We first obtained the simulated reflection coefficient for an isolated antenna, which is shown as the black solid line in Figure 5.16. The performance of each antenna element operating in the array environment was also simulated and the reflection coefficients for several antennas in a panel are shown in Figure 5.16. We compare these results with and without the ellipsoidal breast phantom composed entirely of fatty tissue shown in Figure 5.15(b).

In the case of a sensor array with no phantom present, the antenna elements still exhibit dual-band operation with operating frequencies that deviate slightly from the isolated-antenna operating frequencies of 1.38 GHz (TM<sub>100</sub>) and 2.88 GHz (TM<sub>300</sub>). In the presence of the phantom, the center frequencies of operation are not affected, suggesting that the antenna will perform well in the vicinity of the breast. Figure 5.17 illustrates that the operating frequencies of the antenna are not significantly affected by the type of breast phantom present in the imaging environment.

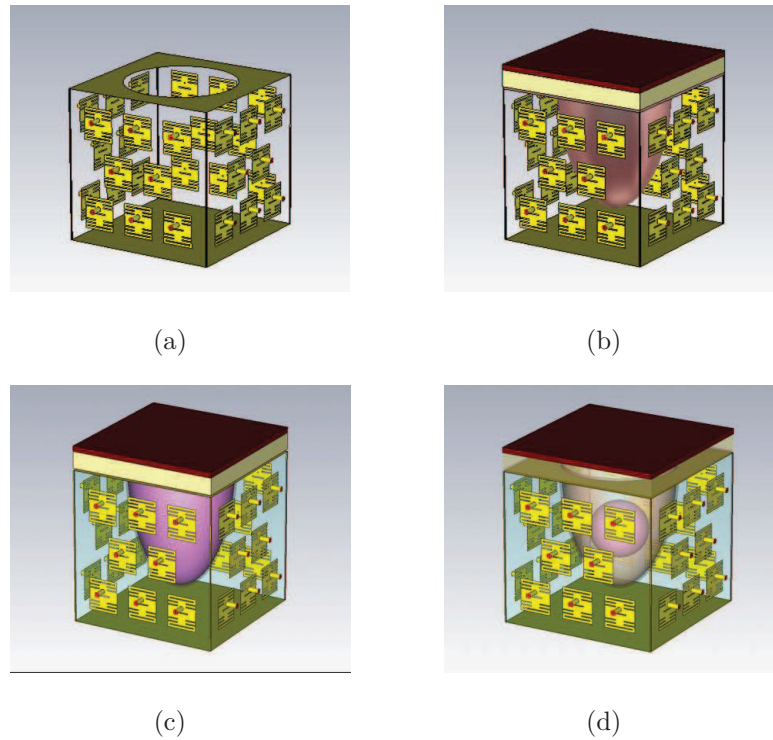
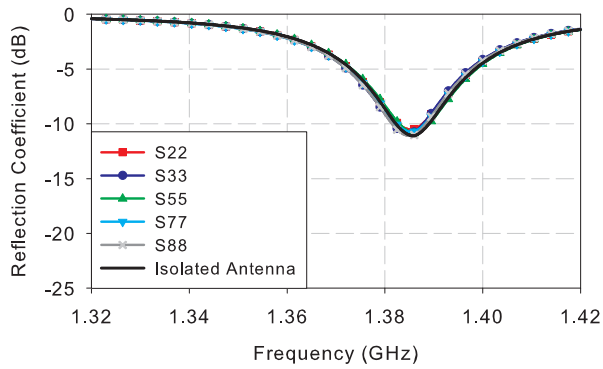


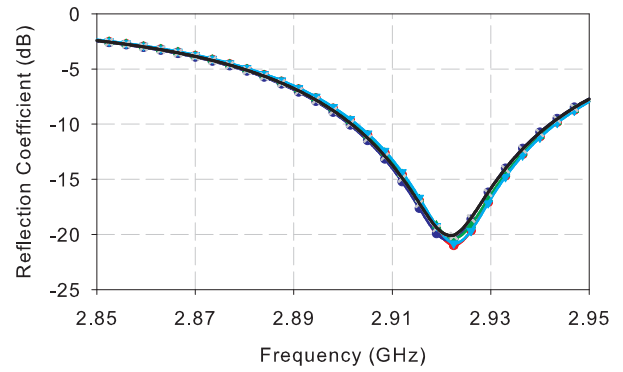
Figure 5.15 Illustration of the 3D sensor array comprised of dual-band miniaturized antennas with (a) no phantom present, (b) simple fatty phantom, (c) simple glandular tissue phantom, and (d) simple fatty and glandular inclusion phantom present.

#### 5.4.2.2 Array composed of RS patch antennas on substrates using a soft-surface structure

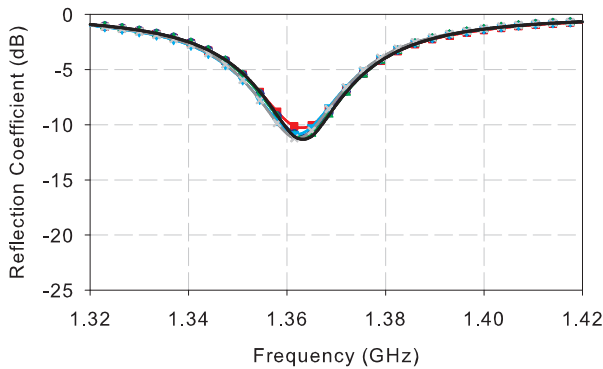
Finally, we investigated the performance of a 3D sensor array composed of array panels that produced a maximum reduction of mutual coupling between pairs of adjacent antennas (see Section 5.3). Each array panel was populated by 32-element RS patch antennas in a staggered-element arrangement and on a substrate using soft-surface structures (Figure 5.18). The theoretical performance was analyzed using numerical simulations conducted with CST Microwave Studio for a 3D sensor array with and without the ellipsoidal breast phantom composed entirely of fatty tissue shown in Figure 5.15(b). The simulated reflection coefficient of a central antenna in the middle row of one of the panels is shown in Figure 5.19. The mutual coupling ( $S_{21}$ ) between such an antenna element and its horizontally and diagonally



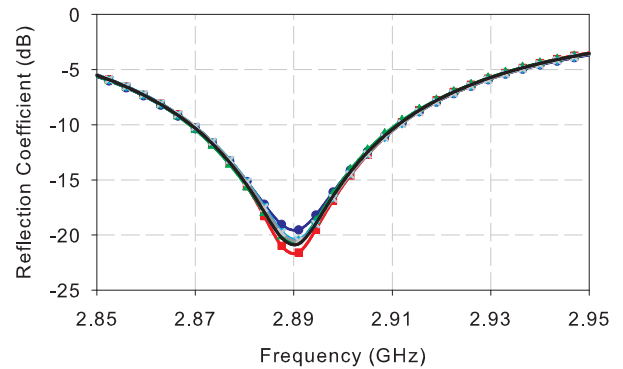
(a)



(b)



(c)



(d)

Figure 5.16 Simulated reflection coefficients ( $S_{ii}$ ) for dual-band miniaturized patch antennas in an oil-filled 3D sensor array. The left and right sub-plots show the 1st and 2nd frequency bands, respectively. [(a)-(b)]  $S_{ii}$  of antennas in sensor array with no phantom present and [(c)-(d)]  $S_{ii}$  of antennas in sensor array with the simple fatty phantom of Figure 5.15(b) present. The bold black line corresponds to a single isolated antenna  $S_{ii}$ .



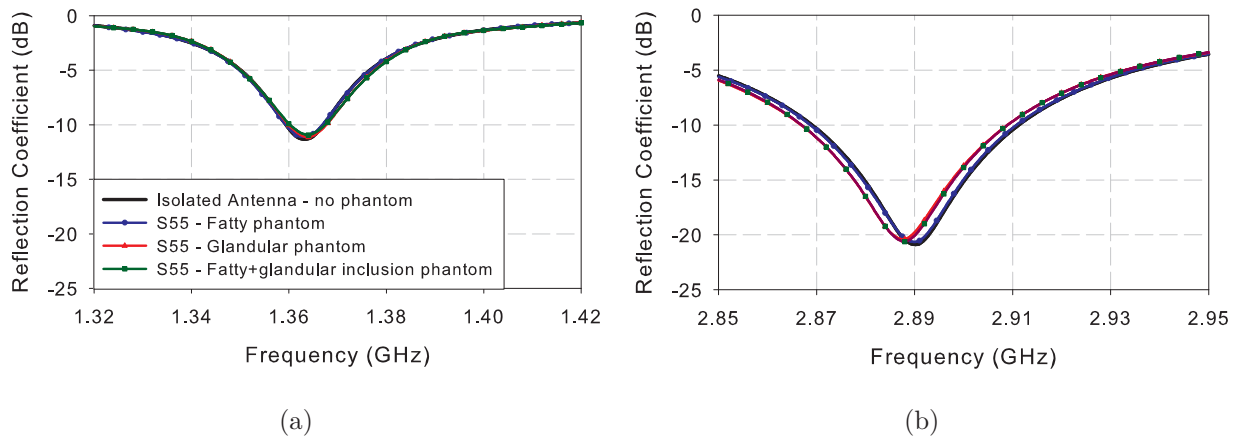
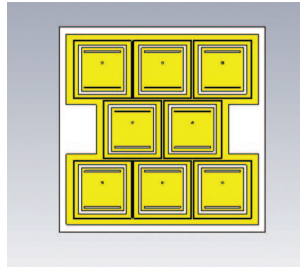


Figure 5.17 Simulated reflection coefficients ( $S_{ii}$ ) for dual-band miniaturized patch antennas in an oil-filled 3D sensor array with and without the phantoms of Figures 5.15 (b)-(c) present. The left and right sub-plots show the 1st and 2nd frequency bands, respectively. The bold black line corresponds to a single isolated antenna  $S_{ii}$  with no phantom present.

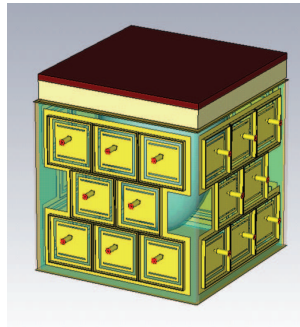
adjacent elements are shown in Figures 5.19 (b) and (c), respectively. The results of the 3D sensor array are also compared to those of an individual panel which are shown as the black solid line in Figure 5.19.

In the case of a sensor array with no phantom present, as can be seen in Figure 5.19(a), the antenna elements still exhibit dual-band operation with operating frequencies of 2.10 GHz ( $TM_{100}$ ) and 3.72 GHz ( $TM_{300}$ ) that do not deviate from the antenna in an individual panel. Furthermore, the mutual coupling between adjacent elements on the same panel does not increase significantly at the operating frequencies of the two bands.

In the presence of the phantom, there is a slight change in the magnitude of the reflection coefficient. However, the center frequencies of operation are not affected, suggesting that this antenna will perform well in the vicinity of the breast. Some changes in the coupling between adjacent antenna elements on the same panel are observed in the presence of the phantom. Those changes are mostly due to scattering from the fatty breast tissue and therefore carry useful information for the purpose of reconstructing the image of the breast tissue.



(a)



(b)

Figure 5.18 Illustration of the 3D sensor array comprised of RS patch antennas on substrates using soft-surface structures. (a) single array panel and (b) 3D sensor array with simple phantom present.

The effect of introducing the breast phantom on the transmission coefficient between central antennas directly facing each other on opposite panels within the 3D sensor array is also examined. The results are shown in Figure 5.20. Changes in the transmission coefficient when the phantom is present demonstrate the ability of the 3D sensor to detect scattering from the phantom and the possible reconstruction of an image.

## 5.5 Summary

The design of a compact 3D sensor array composed of dual-band, miniaturized patch antennas for microwave breast imaging was presented. The array satisfies the space constraints of an existing clinical MRI setup to be used for co-registration of imaging results. Numerical simulations of the operating characteristics of the antenna elements contained in

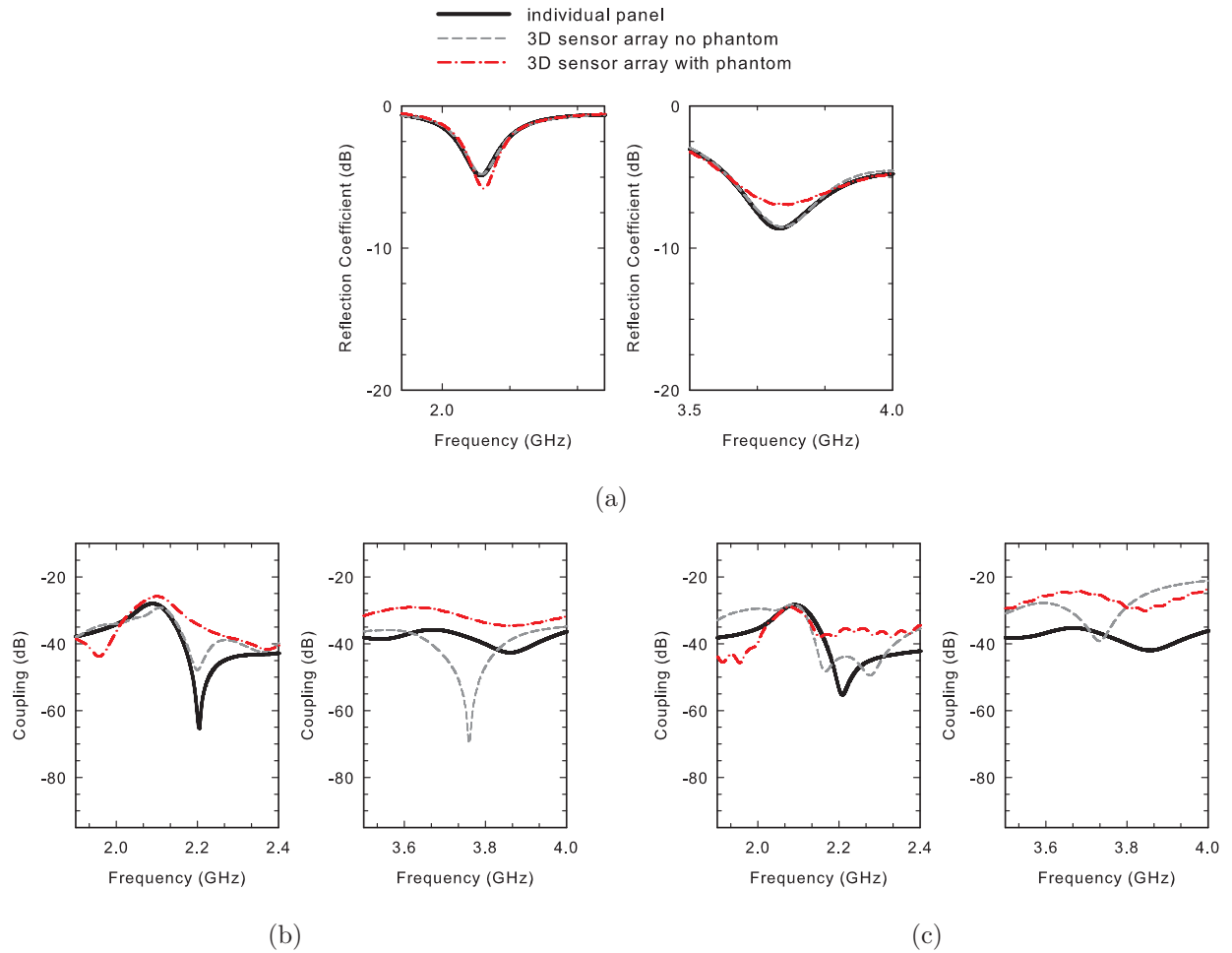


Figure 5.19 Comparison of the responses of antenna elements in an individual array panel and a 3D sensor array with and without the simple phantom of Figure 5.18 (b), immersed in oil. (a) reflection coefficients ( $S_{11}$ ) of a central antenna element. (b)-(c) Mutual coupling ( $S_{21}$ ) between (b) diagonally and (c) horizontally adjacent antennas. The left and right sub-plots show the 1st and 2nd frequency bands, respectively.

the array were performed. The radiating elements of the sensor array exhibit dual-band operation with no significant frequency deviation. The dual-band operation is maintained in the presence of an ellipsoidal breast phantom comprised of different breast tissues. The results of this study suggest antenna arrays comprised of multi-frequency patch antennas are promising candidates for use in microwave breast imaging.

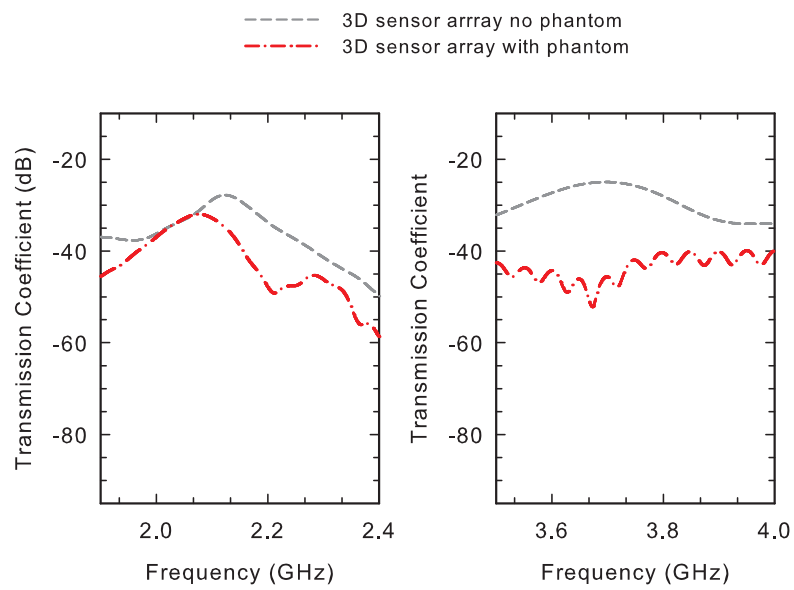


Figure 5.20 Comparison of the transmission coefficients between two central antennas directly facing each other on opposite panels within an oil-filled 3D sensor array with and without the simple phantom of Figure 5.18(b) present. The left and right sub-plots show the 1st and 2nd frequency bands, respectively.

## APPENDIX

### Bandwidth-enhanced miniaturized patch antenna

We have modified the loading technique of the dual-band miniaturized antenna described in [85] such that it provides a greater flexibility in determining the separation between the operating frequencies of  $TM_{100}$  and  $TM_{300}$ . Modifying the length of the center slot (shown in Figure A.1) allows the  $TM_{300}$  frequency to bypass the  $TM_{200}$  frequency and merge with the  $TM_{100}$  frequency. The operational bandwidth of the patch antenna is increased by merging the operating frequency of  $TM_{300}$  with that of  $TM_{100}$ . The proposed patch antenna is designed to operate at 1.76 GHz with a fractional bandwidth of 4.52%.

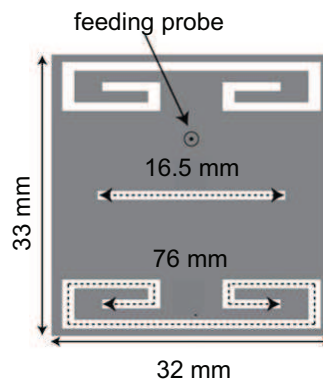


Figure A.1 Top view of proposed bandwidth-enhanced patch antenna.

#### A.0.1 Measurement and experimental verification results

The proposed design technique is validated by fabricating a prototype of the bandwidth-enhanced patch antenna and characterizing its performance. Bandwidth-enhanced antenna elements (Figure A.1) were patterned on a 32-mil-thick RO4003 substrate (Rogers Corp.).

This antenna is probe fed using a center conductor of an SMA connector. We measured the reflection coefficients for fabricated antenna prototypes immersed in a  $32\text{ cm} \times 15\text{ cm} \times 11\text{ cm}$  tank filled with safflower oil. Figure A.2 shows excellent agreement between the simulated and measured  $S_{11}$ . We observe that the operating frequency of the bandwidth-enhanced antenna is reduced by approximately 15% when compared to a previous design [58]. We note that the fractional bandwidth of this design is 4.52% and that this represents an operational bandwidth increase of  $4.7\times$  when compared to a slot-loaded patch (0.97%) [58].

We also characterized the radiation patterns of the bandwidth-enhanced patch antenna immersed in oil. The measurements were taken at a distance of 15 cm from the patch. Figure A.3 shows the co-polarized and cross-polarized radiation patterns in the E- and H-planes at 1.73, 1.76, and 1.80 GHz. The bandwidth-enhanced antenna exhibits measured cross-pol levels of at least 15 dB lower than co-pol at broadside for all frequencies of interest. We observe good agreement between measurement and simulation in the co-pol radiation patterns. Greater cross-pol discrepancy is attributed to the fact that the very low cross-pol levels are more susceptible to measurement imperfections. Figure A.3 shows that the multi-band miniaturized antennas exhibit symmetric and similar radiation patterns for frequencies in its operational bandwidth.

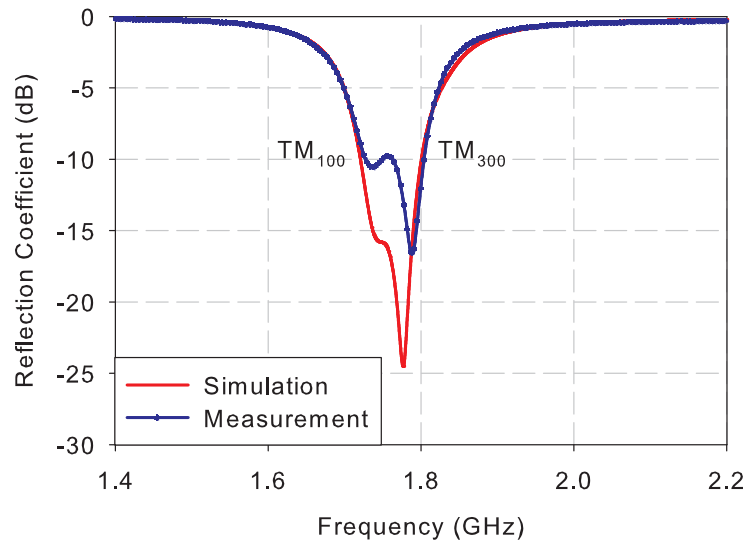


Figure A.2 Simulated and measured reflection coefficients of the bandwidth-enhanced patch antenna of Figure A.1 immersed in safflower oil.

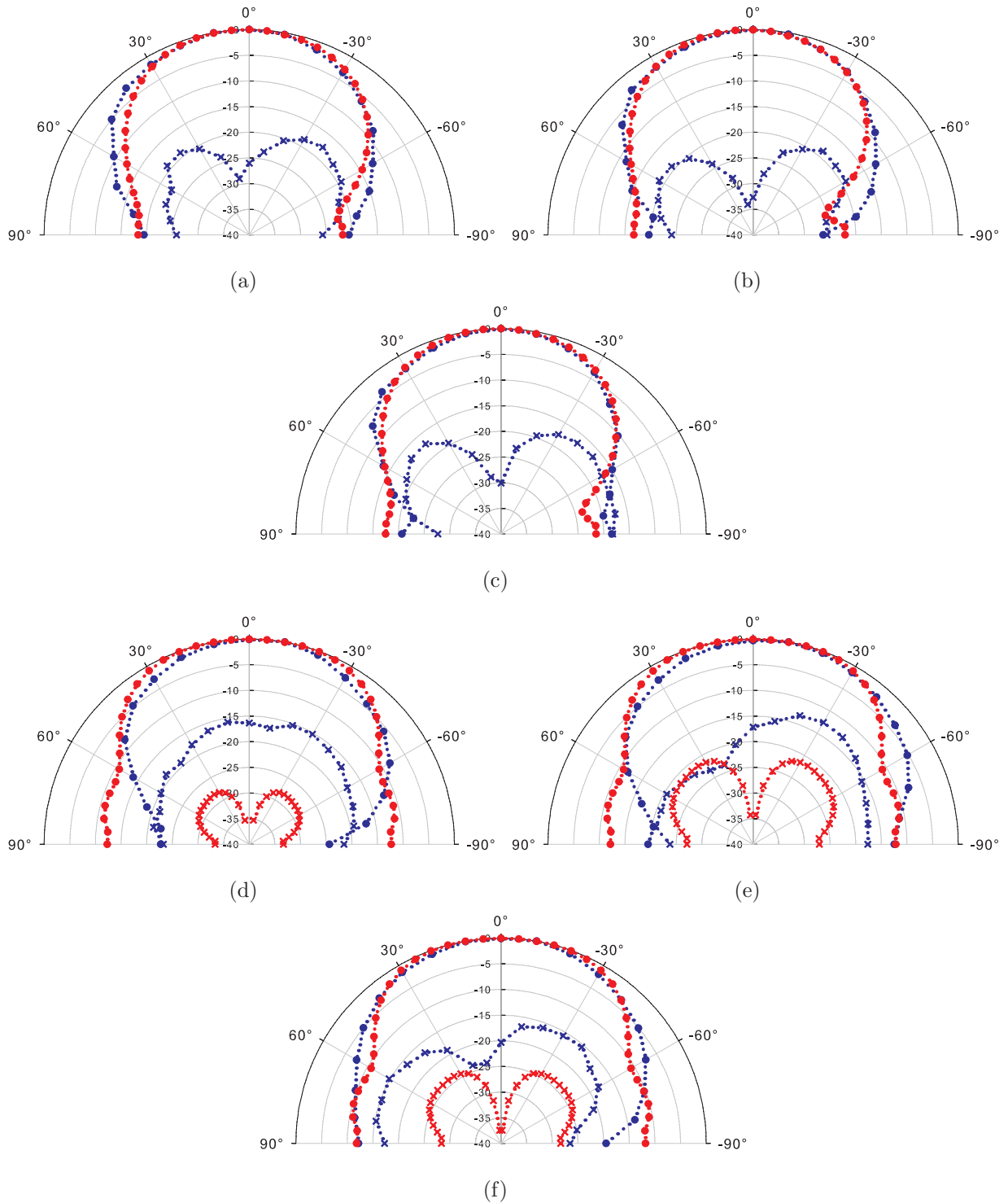


Figure A.3 Measured and simulated radiation patterns of the bandwidth-enhanced patch antenna in oil. The patterns are obtained at a distance of 15 cm from the patch. (a) E-plane at 1.73 GHz (b) 1.76 GHz and (c) 1.80 GHz. (d) H-plane at 1.73 GHz (e) 1.76 GHz and (f) 1.80 GHz. Red: simulated data. Blue: measured data. Circle: co-pol. x: cross-pol.



## LIST OF REFERENCES

- [1] P. Meaney, M. Fanning, T. Raynolds, C. Fox, Q. Fang, C. Kogel, S. Poplack, and K. Paulsen, "Initial clinical experience with microwave breast imaging in women with normal mammography," *Academic Radiology*, vol. 14, pp. 207–218, Feb. 2007.
- [2] T. Rubaek, O. Kim, and P. Meincke, "Computational validation of a 3-D microwave imaging system for breast-cancer screening," *IEEE Transactions on Antennas and Propagation*, vol. 57, pp. 2105–2115, July 2009.
- [3] C. Yu, M. Yuan, J. Stang, E. Bresslour, R. George, G. Ybarra, W. Joines, and Q. Liu, "Active microwave imaging II: 3-D system prototype and image reconstruction from experimental data," *IEEE Transactions on Microwave Theory and Techniques*, vol. 56, pp. 991–1000, Apr. 2008.
- [4] A. C. Society, "Breast cancer facts and figures 2009-2010," Atlanta, GA, 2009.
- [5] P. Vacek and B. Geller, "A prospective study of breast cancer risk using routine mammographic breast density measurements," *Cancer Epidemiol Biomarkers Prev.*, vol. 13, pp. 715–722, May 2004.
- [6] W. Barlow, E. White, R. Ballard-Barbash, P. Vacek, L. Titus-Ernstoff, P. Carney, J. Tice, D. S. M. Buist, B. Geller, R. Rosenberg, B. Yankaskas, and K. Kerlikowske, "Prospective breast cancer risk prediction model for women undergoing screening mammography," *Journal of the National Cancer Institute*, vol. 98, no. 7, pp. 1204–1214, 2006.
- [7] N. Boyd, H. Guo, L. Martin, L. Sun, J. Stone, E. Fishell, R. Jong, G. Hislop, A. Chiarelli, S. Minkin, and M. Yaffe, "Mammographic density and the risk and detection of breast cancer," *The New England Journal of Medicine*, vol. 356, pp. 227–236, Jan. 2007.
- [8] K. Kerlikowske, L. Ichikawa, D. Miglioretti, D. Buist, P. Vacek, R. Smith-Bindman, B. Yankaskas, P. Carney, and R. Ballard-Barbash, "Longitudinal measurement of clinical mammographic breast density to improve estimation of breast cancer risk," *Journal of the National Cancer Institute*, vol. 99, no. 5, pp. 386–395, 2007.

- [9] I. of Medicine and N. R. Council, “Mammography and beyond: developing technologies for the early detection of breast cancer.” National Academy Press, Washington, DC, 2001.
- [10] J. Joy, E. Penhoet, and D. Petitt, eds., *Saving Womens Lives: Strategies for Improving Breast Cancer Detection and Diagnosis*. Washington, DC: National Academies Press, Institute of Medicine, 2005.
- [11] P. Carney, D. Miglioretti, B. Yankaskas, K. Kerlikowske, R. Rosenberg, C. Rutter, B. Geller, L. Abraham, S. Taplin, M. Dignan, G. Cutter, and R. Ballard-Barbash, “Individual and combined effects of age, breast density, and hormone replacement therapy use on the accuracy of screening mammography,” *Annals of Internal Medicine*, vol. 138, no. 3, pp. 168–175, 2003.
- [12] D. Saslow, C. Boetes, W. Burke, S. Harms, M. Leach, C. Lehman, E. Morris, E. Pisano, M. Schnall, S. Sener, R. Smith, E. Warner, M. Yaffe, K. Andrews, and C. Russell, “American Cancer Society guidelines for breast screening with MRI as an adjunct to mammography,” *CA: A Cancer Journal for Clinicians*, vol. 57, pp. 75–89, Apr. 2007.
- [13] J. Elmore, K. Armstrong, C. Lehman, and S. Fletcher, “Screening for breast cancer,” *Journal of American Medical Association*, vol. 293, pp. 1245–1256, 2005.
- [14] A. Bulyshev, S. Semenov, A. Souvorov, R. Svenson, A. Nazarov, Y. Sizov, and G. Tattis, “Computational modeling of three-dimensional microwave tomography of breast cancer,” *IEEE Transactions on Biomedical Engineering*, vol. 48, pp. 1053–1056, Sept. 2001.
- [15] J. De Zaeytijd, A. Franchois, C. Eyraud, and J.-M. Geffrin, “Full-wave three-dimensional microwave imaging with a regularized Gauss-Newton method: Theory and experiment,” *IEEE Transactions on Antennas and Propagation*, vol. 55, pp. 3279–3292, Nov. 2007.
- [16] C. Gilmore, A. Abubakar, W. Hu, T. Habashy, and P. van den Berg, “Microwave biomedical data inversion using the finite-difference contrast source inversion method,” *IEEE Transactions on Antennas and Propagation*, vol. 57, pp. 1528–1538, May 2009.
- [17] D. Winters, J. Shea, P. Kosmas, B. Van Veen, and S. Hagness, “Three-dimensional microwave breast imaging: Dispersive dielectric properties estimation using patient-specific basis functions,” *IEEE Transactions on Medical Imaging*, vol. 28, pp. 969–981, July 2009.
- [18] J. Shea, P. Kosmas, B. V. Veen, and S. Hagness, “Contrast-enhanced microwave imaging of breast tumors: A computational study using 3D realistic numerical phantoms,” *Inverse Problems*, vol. 26, Apr. 2010.

- [19] P. Kosmas and C. Rappaport, “A matched filter FDTD-based time reversal algorithm for microwave breast cancer detection,” *IEEE Transactions on Antennas and Propagation*, vol. 54, pp. 1257–1264, Apr. 2006.
- [20] E. Bond, X. Li, S. Hagness, and B. V. Veen, “Microwave imaging via space-time beamforming for early detection of breast cancer,” *IEEE Transactions on Antennas and Propagation*, vol. 51, pp. 1690–1705, Aug. 2003.
- [21] J. Johnson, T. Takenaka, and T. Tanaka, “Two-dimensional time-domain inverse scattering for quantitative analysis of breast composition,” *IEEE Transactions on Biomedical Engineering*, vol. 55, pp. 1941–1945, Aug. 2008.
- [22] E. Zastrow, S. Davis, M. Lazebnik, F. Kelcz, B. Van Veen, and S. Hagness, “Development of anatomically realistic numerical breast phantoms with accurate dielectric properties for modeling microwave interactions with the human breast,” *IEEE Transactions on Biomedical Engineering*, vol. 55, pp. 2792–2800, Dec. 2008.
- [23] M. Lazebnik, E. Madsen, G. Frank, and S. Hagness, “Tissue-mimicking phantom materials for narrowband and ultrawideband microwave applications,” *Physics in Medicine and Biology*, vol. 50, pp. 4245–4258, 2005.
- [24] S. Poplack, T. Tosteson, W. Wells, B. Pogue, P. Meaney, A. Hartov, C. Kogel, S. Soho, J. Gibson, and K. Paulsen, “Electromagnetic breast imaging: Results of a pilot study in women with abnormal mammograms,” *Radiology*, pp. 350–359, May 2007.
- [25] M. Klemm, I. Craddock, J. Leendertz, A. Preece, and R. Benjamin, “Experimental and clinical results of breast cancer detection using UWB microwave radar,” in *IEEE Antennas and Propagation Society International Symposium, AP-S 2008*, pp. 1–4, July 2008.
- [26] S. Heywang-Koebrunner, A. Heinig, D. Pickuth, T. Alberich, and R. Spielmann, “Interventional MRI of the breast: Lesion localisation and biopsy,” *Eur Radiol*, vol. 10, pp. 36–45, 2000.
- [27] N. de Souza, D. Kormos, and T. Krausz, “MR-guided biopsy of the breast after lumpectomy and radiation therapy using two methods of immobilization in the lateral decubitus position,” *J. Magnetic Resonance Imaging*, vol. 5, pp. 525–528, Oct. 1995.
- [28] Q. Fang, P. Meaney, and K. Paulsen, “Singular value analysis of the Jacobian matrix in microwave image reconstruction,” *IEEE Transactions on Antennas and Propagation*, vol. 54, pp. 2371–2380, Aug. 2006.
- [29] J. Shea, P. Kosmas, S. Hagness, and B. V. Veen, “Three-dimensional microwave imaging of realistic numerical breast phantoms via a multiple-frequency inverse scattering technique,” *Medical Physics*, vol. 37, pp. 4210–4226, Aug. 2010.

- [30] X. Li, E. Bond, B. Van Veen, and S. Hagness, “An overview of ultra-wideband microwave imaging via space-time beamforming for early-stage breast-cancer detection,” *IEEE Antennas and Propagation Magazine*, vol. 47, pp. 19–34, Feb. 2005.
- [31] R. Kruger, K. Stantz, and J. W. Kiser, “Thermoacoustic CT of the breast,” *Proceedings of the SPIE*, vol. 4682, pp. 521–525, 2002.
- [32] M. Xu, G. Ku, X. Jin, L. Wang, B. Fornage, and K. Hunt, “Breast cancer imaging by microwave-induced thermoacoustic tomography,” *Proceedings of the SPIE*, vol. 5697, pp. 45–48, 2005.
- [33] X. Jin and L. Wang, “Thermoacoustic tomography with correction for acoustic speed variations,” *Physics in Medicine and Biology*, vol. 51, no. 24, pp. 6437–6448, 2006.
- [34] A. Mashal, J. Booske, and S. Hagness, “Toward contrast-enhanced microwave-induced thermoacoustic imaging of breast cancer: An experimental study of the effects of microbubbles on simple thermoacoustic targets,” *Physics in Medicine and Biology*, vol. 54, no. 3, 2009.
- [35] J. Sill and E. Fear, “Tissue sensing adaptive radar for breast cancer detection - Experimental investigation of simple tumor models,” *IEEE Transactions on Microwave Theory and Techniques*, vol. 53, no. 11, pp. 3312–3319, 2005.
- [36] M. Lazebnik, L. McCartney, D. Popovic, C. Watkins, M. Lindstrom, J. Harter, S. Sewall, A. Magliocco, J. Booske, M. Okoniewski, and S. Hagness, “A large-scale study of the ultrawideband microwave dielectric properties of normal breast tissue obtained from reduction surgeries,” *Physics in Medicine and Biology*, vol. 52, pp. 2637–2656, 2007.
- [37] S. Semenov, A. Bulyshev, A. Abubakar, V. Posukh, Y. Sizov, A. Souvorov, P. van den Berg, and T. Williams, “Microwave-tomographic imaging of the high dielectric-contrast objects using different image-reconstruction approaches,” *IEEE Transactions on Microwave Theory and Techniques*, vol. 53, pp. 2284–2294, July 2005.
- [38] C. Gilmore, P. Mojabi, A. Zakaria, M. Ostadrahimi, C. Kaye, S. Noghianian, L. Shafai, S. Pistorius, and J. LoVetri, “A wideband microwave tomography system with a novel frequency selection procedure,” *IEEE Transactions on Biomedical Engineering*, vol. 57, pp. 894–904, Apr. 2010.
- [39] D. Armani and C. Liu, “Microfabrication technology for polycaprolactone, a biodegradable polymer,” *J. Micromechanics Microengineering*, vol. 10, pp. 80–84, Jan. 2000.
- [40] A. Wurm, R. Soliman, and C. Schick, “Early stages of polymer crystallization: a dielectric study,” *Polymer*, vol. 44, pp. 7467–7476, Nov. 2003.

- [41] A. Bello, E. Laredo, and M. Grimau, "Comparison of analysis of dielectric spectra of PCL in the  $\epsilon^*$  and the  $M^*$  formalism," *J. of Non-Crystalline Solids*, vol. 353, pp. 4283–4287, Oct. 2007.
- [42] R. Capps, G. Stack, M. Samuels, and L. Beumel, "Dielectric and viscoelastic properties of some meta-tetramethyl xylene diisocyanate-based polyurethanes as a function of sample composition," *J. of Applied Polymer Science*, vol. 45, pp. 1175–1188, July 1992.
- [43] W. Chew, *Waves and Fields in Inhomogeneous Media*. Piscataway, NJ: IEEE Press, 1995.
- [44] Q. Fang, P. Meaney, and K. Paulsen, "Microwave image reconstruction of tissue property dispersion characteristics utilizing multiple-frequency information," *IEEE Transactions on Microwave Theory and Techniques*, vol. 52, pp. 1866–1875, Aug. 2004.
- [45] B. Brandstatter, K. Hollaus, H. Hutten, M. Mayer, R. Merwa, and H. Scharfetter, "Direct estimation of Cole parameters in multifrequency EIT using a regularized Gauss-Newton method," *Physiological Measurement*, vol. 24, pp. 437–448, May 2003.
- [46] P. Meaney, K. Paulsen, A. Hartov, and R. Crane, "An active microwave imaging system for reconstruction of 2-D electrical property distributions," *IEEE Transactions on Biomedical Engineering*, vol. 42, pp. 1017–1026, Oct. 1995.
- [47] D. Li, P. Meaney, T. Raynolds, S. Pendergrass, M. Fanning, and K. Paulsen, "Parallel-detection microwave spectroscopy system for breast imaging," *Review of Scientific Instruments*, vol. 75, no. 7, pp. 2305–2313, 2004.
- [48] N. Behdad, W. H. D. Shi, K. Sarabandi, and M. Flynn, "A 0.3 mm miniaturized X-band on-chip slot antenna in  $0.13 \mu$  CMOS," in *Proceedings IEEE RFIC Symposium*, vol. 1, pp. 441–444, June 2007.
- [49] J. Stang, W. Joines, Q. Liu, G. Ybarra, R. George, M. Yuan, and I. Leonhardt, "A tapered microstrip patch antenna array for use in breast cancer screening via 3D active microwave imaging," in *IEEE Antennas and Propagation Society International Symposium, 2009. APSURSI '09.*, pp. 1–4, June 2009.
- [50] R. Garg, P. Bhartia, I. Bahl, and A. Ittipiboon, *Microstrip Antenna Design Handbook*. Norwood, MA: Artech House, 1995.
- [51] K. Wong, *Compact and Broadband Microstrip Antennas*. New York: John Wiley & Sons, 2002.
- [52] G. Kumar and K. Ray, *Broadband Microstrip Antennas*. Norwood, MA: Artech House, 2003.

- [53] K. Lau, K. Kong, and K. Luk, "A miniature folded shorted patch antenna for dual-band operation," *IEEE Transactions on Antennas and Propagation*, vol. 55, pp. 2391–2398, Aug. 2007.
- [54] J.-H. Lu and K.-L. Wong, "Slot-loaded, meandered rectangular microstrip antenna with compact dual frequency operation," *Electronics Letters*, vol. 34, pp. 1048 – 1050, May 1998.
- [55] X.-X. Zhang and F. Yang, "Study of a slit cut on a microstrip antenna and its applications," *Microwave and Optical Technology Letters*, vol. 18, pp. 297–300, July 1998.
- [56] J.-H. Lu, "Single-feed dual-frequency rectangular microstrip antenna with pair of step-slots," *Electronics Letters*, vol. 35, pp. 354 –355, Mar. 1999.
- [57] S. Maci and G. Gentili, "Dual-frequency patch antennas," *IEEE Antennas and Propagation Magazine*, vol. 39, pp. 13–20, Dec. 1997.
- [58] S. Maci, G. Biffi Gentili, P. Piazzesi, and C. Salvador, "Dual-band slot-loaded patch antenna," *IEE Proc. Microwaves, Antennas and Propagation*, vol. 142, pp. 225–232, Jun. 1995.
- [59] K. Lee, K. Luk, K. Mak, and S. Yang, "On the use of u-slots in the design of dual- and triple-band patch antennas," *IEEE Antennas and Propagation Magazine*, vol. 53, pp. 60–74, Jun. 2011.
- [60] S. Reed, L. Desclos, C. Terret, and S. Toutain, "Patch antenna size reduction by means of inductive slots," *Microwave and Optical Technology Letters*, vol. 29, pp. 79–81, Apr. 2001.
- [61] C. S. Lee and K.-H. Tseng, "Radiation efficiency of electrically small microstrip antennas with width discontinuities," *IEEE Transactions on Antennas and Propagation*, vol. 53, pp. 871–873, Feb. 2005.
- [62] K.-P. Yang and K.-L. Wong, "Dual-band circularly-polarized square microstrip antenna," *IEEE Transactions on Antennas and Propagation*, vol. 49, pp. 377–382, Mar. 2001.
- [63] M. Abu, M. Rahim, and M. Karim, "A meandered rectangular microstrip antenna for dual-frequency operation," in *Asia-Pacific Microwave Conference, APMC 2008*, pp. 16–20, Dec. 2008.
- [64] B. Wang and Y. Lo, "Microstrip antennas for dual-frequency operation," *IEEE Transactions on Antennas and Propagation*, vol. 32, pp. 938–943, Sep. 1984.
- [65] P. Meaney, K. Paulsen, and J. Chang, "Near-field microwave imaging of biologically-based materials using a monopole transceiver system," *IEEE Transactions on Microwave Theory and Techniques*, vol. 46, pp. 31–45, Jan. 1998.

- [66] D. Thompson, O. Tantot, H. Jallageas, G. Ponchak, M. Tentzeris, and J. Papapolymerou, "Characterization of liquid crystal polymer (LCP) material and transmission lines on LCP substrates from 30 to 110 GHz," *IEEE Transactions on Microwave Theory and Techniques*, vol. 52, pp. 1343–1352, Apr. 2004.
- [67] S. Koulouridis, G. Kiziltas, Y. Zhou, D. Hansford, and J. Volakis, "Polymer-ceramic composites for microwave applications: Fabrication and performance assessment," *IEEE Transactions on Microwave Theory and Techniques*, vol. 54, pp. 4202–4208, Dec. 2006.
- [68] H. Sharifi, R. Lahiji, H.-C. Lin, P. Ye, L. Katehi, and S. Mohammadi, "Characterization of Parylene-N as flexible substrate and passivation layer for microwave and millimeter-wave integrated circuits," *IEEE Transactions on Advanced Packaging*, vol. 32, pp. 84–92, Feb. 2009.
- [69] M.-Q. Lee and S. Nam, "An accurate broadband measurement of substrate dielectric constant," *IEEE Microwave and Guided Wave Letters*, vol. 6, pp. 168–170, Apr. 1996.
- [70] S. Barot and J. Bernhard, "Permittivity measurement of layered media using a microstrip test bed," in *IEEE Antennas and Propagation Society International Symposium*, pp. 1–4, July 2008.
- [71] S.-H. Chang, H. Kuan, H.-W. Wu, R.-Y. Yang, and M.-H. Weng, "Determination of microwave dielectric constant by two microstrip line method combined with EM simulation," *Microwave and Optical Technology Letters*, vol. 48, pp. 2199–2201, Nov. 2006.
- [72] J. Baker-Jarvis, M. Janezic, and D. Degroot, "High-frequency dielectric measurements," *IEEE Instrumentation Measurement Magazine*, vol. 13, pp. 24–31, Apr. 2010.
- [73] A. Djordjevi, R. Biljic, V. Likar-Smiljanic, and T. Sarkar, "Wideband frequency-domain characterization of FR-4 and time-domain causality," *IEEE Transactions on Electromagnetic Compatibility*, vol. 43, pp. 662–667, Nov. 2001.
- [74] M. Cauwe and J. De Baets, "Broadband material parameter characterization for practical high-speed interconnects on printed circuit board," *IEEE Transactions on Advanced Packaging*, vol. 31, pp. 649–656, Aug. 2008.
- [75] P. Queffelec, P. Gelin, J. Gieraltowski, and J. Loaec, "A microstrip device for the broad band simultaneous measurement of complex permeability and permittivity," *IEEE Transactions on Magnetism*, vol. 30, pp. 224–231, Mar. 1994.
- [76] J.-Y. Chung, K. Sertel, and J. Volakis, "Broadband characterization of bulk and thin magnetic composites using stripline structures," *IEEE Transactions on Microwave Theory and Techniques*, vol. 58, pp. 2960–2967, Nov. 2010.

- [77] Agilent Technologies, Santa Clara, CA, *Agilent Advanced Design System 2009 User Manual*. (see, e.g., "Distributed Components - Microstrip Components - Microstrip Line").
- [78] M. Ramazani, H. Miladi, M. Shahabadi, and S. Mohajerzadeh, "Loss measurement of aluminum thin-film coplanar waveguide (CPW) lines at microwave frequencies," *IEEE Transactions on Electron Devices*, vol. 57, pp. 2037–2040, Aug. 2010.
- [79] H.-Y. Lee, "Wideband characterization of a typical bonding wire for microwave and millimeter-wave integrated circuits," *IEEE Transactions on Microwave Theory and Techniques*, vol. 43, pp. 63–68, Jan. 1995.
- [80] S.-K. Yun and H.-Y. Lee, "Parasitic impedance analysis of double bonding wires for high-frequency integrated circuit packaging," *IEEE Microwave and Guided Wave Letters*, vol. 5, pp. 296–298, Sept. 1995.
- [81] E. Yamashita, H. Ohashi, and K. Atsuki, "Characterization of microstrip lines near a substrate edge and design formulas of edge-compensated microstrip lines [MMICs]," *IEEE Transactions on Microwave Theory and Techniques*, vol. 37, pp. 890–896, May 1989.
- [82] J. Muldavin and G. Rebeiz, "Millimeter-wave tapered-slot antennas on synthesized low permittivity substrates," *IEEE Transactions on Antennas and Propagation*, vol. 47, pp. 1276–1280, Aug. 1999.
- [83] Agilent Technologies, Santa Clara, CA, *Agilent 85070D Dielectric Probe Kit Manual*.
- [84] C. A. Balanis, *Advanced Engineering Electromagnetics*. Wiley, 1989.
- [85] M. Al-Joumayly, S. Aguilar, N. Behdad, and S. Hagness, "Dual-band miniaturized patch antennas for microwave breast imaging," *IEEE Antennas and Wireless Propagation Letters*, vol. 9, pp. 268–271, 2010.
- [86] CST Computer Simulation Technology, San Mateo, CA, *CST Microwave Studio*. (see, e.g., "Material Overview (HF)").
- [87] J. Lee and S. Nam, "Effective area of a receiving antenna in a lossy medium," *IEEE Transactions on Antennas and Propagation*, vol. 57, pp. 1843–1845, Jun. 2009.
- [88] R. F. Harrington, *Time-harmonic electromagnetic fields*. McGraw-Hill, 1961.
- [89] D. M. Pozar, *Microwave Engineering*. John Wiley & Sons, 2004.
- [90] CTIA, Washington, D.C., *Test Plan for Mobile Station Over the Air Performance*, revision 3.1 ed., 2011.



- [91] S. Aguilar, S. Hagness, N. Behdad, B. Van Veen, J. Shea, and M. Al-Joumayly, “Dielectric characterization of PCL-based thermoplastic materials for microwave diagnostic and therapeutic applications,” *IEEE Transactions on Biomedical Engineering*, vol. 59, pp. 627–633, Mar. 2012. in press.
- [92] S. M. Aguilar, M. A. Al-Joumayly, M. J. Burfeindt, N. Behdad, and S. C. Hagness, “Multi-band miniaturized patch antennas for microwave breast imaging,” *IEEE Transactions on Antennas and Propagation*. under preparation.
- [93] J.-G. Yook and L. Katehi, “Micromachined microstrip patch antenna with controlled mutual coupling and surface waves,” *IEEE Transactions on Antennas and Propagation*, vol. 49, pp. 1282–1289, Sep 2001.
- [94] G. Ruvio, P.-S. Kildal, and S. Maci, “Modal propagation in ideal soft and hard waveguides,” vol. 4, pp. 438–441, Jun. 2003.
- [95] Y. Zhang, “Enrichment of package antenna approach with dual feeds, guard ring, and fences of vias,” *IEEE Transactions on Advanced Packaging*, vol. 32, pp. 612–618, Aug. 2009.
- [96] S. Aguilar, M. Al-Joumayly, J. Shea, N. Behdad, and S. Hagness, “Design of a microwave breast imaging array composed of dual-band miniaturized antennas,” in *General Assembly and Scientific Symposium, 2011 XXXth URSI*, pp. 1–4, aug. 2011.
- [97] S. Gabriel, R. Lau, and C. Gabriel, “The dielectric properties of biological tissues: III. Parametric models for the dielectric spectrum of tissues,” *Physics in Medicine and Biology*, vol. 41, pp. 2271–2293, 1996.